Follicular fluid, ovarian cortical inclusion cysts, and substrate curvature increase the cancerous progression of fallopian tube epithelial cells

By

Andrew Joseph Fleszar

A dissertation submitted in partial fulfillment of the requirements for the degree of

Doctor of Philosophy

(Biomedical Engineering)

At the

UNIVERSITY OF WISCONSIN-MADISON

2019

Date of final oral examination: 8/8/2019

The dissertation is approved by the following members of the Final Oral Committee:

Pamela Kreeger, Associate Professor, Biomedical Engineering
Kristyn Masters, Professor, Biomedical Engineering
David Beebe, Professor, Biomedical Engineering
Jacob Notbohm, Assistant Professor, Engineering Physics
Joan Jorgensen, Associate Professor, Pharmacology
Krishanu Saha, Assistant Professor, Biomedical Engineering

Abstract

A growing body of research supports the idea that the fallopian tube epithelium (FTE) is the precursor for most high-grade serous ovarian cancers (HGSOCs). Studies indicate that the ovary plays a critical role in tumor metastasis; however, the mechanism or mechanisms underlying the impact of the ovary on disease progression remain poorly understood. The central hypothesis of this thesis was that follicular fluid secreted during ovulation and the microenvironment of the ovary encourage the cancerous progression of FTE cells. To address this hypothesis, we developed *in vitro* models to examine the impact that chemical stimuli and physical interactions within the ovarian microenvironment had on FTE cell behavior. This thesis first demonstrated that chemical stimuli released during ovulation enabled FTE cells to evade anoikis by evaluating the impact of follicular fluid on the anchorage-independent survival of FTE cells. Next, this thesis investigated the role that cortical inclusion cysts (CICs) in the ovarian cortex played in HGSOC as these cysts have been hypothesized to create a niche environment for cancer progression. Through histological analysis of pathology samples from human ovaries, we determined that collagen I and III were elevated near CICs and that the collagen fibers in this dense region were oriented parallel to the cyst boundary. Using this information from human samples as design parameters, we engineered an *in vitro* model that recreated the size, shape, and extracellular matrix properties of CICs. We found that FTE cells within our model underwent robust invasion that was responsive to stimulation with follicular fluid, while ovarian surface epithelial cells, the native cells of the ovary, were non-invasive. We provided experimental evidence to support a role of the extracellular matrix in modulating FTE cell invasion, as a decrease in collagen I concentration or the addition of collagen III to the matrix surrounding the CIC mimic increased FTE cell invasion. During histological analysis of ovarian CICs, we noticed that these structures had a diverse range of curvatures, and we hypothesized that variations in ovarian CIC curvature impact the ability of trapped FTE cells to invade into the surrounding stroma. Using our *in vitro* model of CICs, we determined that increased curvature resulted in more invasion of FTE cells. To isolate curvature as a

system parameter, we developed a novel technique to pattern concave curvatures into collagen gels. When FTE cells were seeded to confluency on curved substrates, increased curvature increased the number of invading FTE cells and the invasion distance. FTE invasion into collagen substrates with higher curvature depended on matrix metalloproteinases (MMPs), but expression of collagen I degrading *Mmps* was not different on curved and flat regions. A finite element (FE) model predicted that contractility and cell-cell connections were essential for increased invasion on substrates with higher curvature, while cell-substrate interactions had minimal effect. Experiments supported these predictions, with invasion decreased by blebbistatin, EGTA, or N-cadherin blocking antibody, but with no effect from a focal adhesion kinase (FAK) inhibitor. Finally, experimental evidence supported that cell invasion on curved substrates occurred in two phases—a cell-cell dependent initiation phase where individual cells broke away from the monolayer and a MMP dependent phase as cells migrated further into the collagen matrix. Taken together, this thesis showed that *in vitro* models of anchorage-independent cell survival, ovarian CICs, and substrate curvature can act as important tools for understanding FTE cell interactions with their environment and the cancerous progression of these cells.

Acknowledgements

The help and support of many people helped make this thesis possible. First and foremost, I would like to thank my Ph.D. advisor, Professor Pamela Kreeger for her guidance and unwavering support. Your ideas, work ethic, motivation, and mentorship have helped facilitate this project's success and inspired me to become a better scientist. I would like to thank the members of my Ph.D. committee, Professors Kristyn Masters, Jacob Notbohm, Joan Jorgensen, David Beebe, and Kris Saha, for the time, guidance, and insight they contributed to the completion of this thesis. Would also like to thank Dr. Jeffery Jones at Generations Fertility Care for the collection of follicular fluid used in this thesis. Furthermore, I would like to thank the University of Wisconsin Translational Research Initiatives in Pathology laboratory, in part supported by the UW Department of Pathology and Laboratory Medicine and UWCCC Grant No. P30 CA014520, for use of its facilities and services and the University of Wisconsin Optical Imaging Core for use of its facilities and services. To all the past and present members of the Kreeger Lab, thank you for your support, ideas, and friendship. I would like to thank my mother, father, and brother for their love, support, understanding, and motivation throughout this journey. My success would not have been possible without you. Lastly, I would like to thank my fiancée Sophie for her unconditional love and support and always being there to pick me up after tough days and celebrate triumphs.

Funding for this research was provided by the American Cancer Society (RSG-13-026-01-CSM and Midwest Division supplement), NIH (1DP2CA195766-01, 1R01CA232517, and 1R21CA227922), Hilldale Research Fellowship, and NSF (CMMI-1660703).

Table of Contents

Table of figures

List of tables

List of abbreviations

HGSOC	high-grade serous ovarian cancer
FTE	fallopian tube epithelial
CICs	cortical inclusion cysts
FE	finite element
ECM	extracellular matrix
STIC	serous tubal intraepithelial carcinoma
MMPs	matrix metalloproteinases
FAK	focal adhesion kinase
SHG	second harmonic generation
OSE	ovarian surface epithelial
EMT	epithelial-mesenchymal transition
SCOUT	secretory cell outgrowth
TACS	tumor associate collagen signatures
IVF	*in vitro* fertilization
PI	propidium iodide
FBS	fetal bovine serum
TBS	tris-buffered saline
PDMS	poly-dimethylsiloxane
SFM	serum free media
H&E	hematoxylin and eosin
IMF	immunofluorescent
SEC	size exclusion chromatography

Chapter 1: Thesis Overview

1.1 Introduction

High-grade serous ovarian cancer (HGSOC) has a 10-year survival rate of less than 30%, a prognosis that has not significantly improved over the past 30 years [1]. A major contributing factor to this dismal and stagnant survival rate is a lack of reliable screening methods for ovarian cancer. The inability to effectively screen for HGSOC prevents diagnosis until the disease has advanced to late stages, with over 70% of patients diagnosed with stage III or IV tumors that have metastasized beyond the pelvis [2]. The late stage at which patients are diagnosed has prompted researchers to investigate the early stage progression of HGSOC from a primary tumor to a metastatic carcinoma. While a growing body of evidence indicates that fallopian tube epithelial (FTE) cells are the cells-of-origin for HGSOC, studies show that the ovary still plays an important role in disease progression [3-5]; however, further studies need to be performed to identify features of the ovary that can promote ovarian cancer progression.

Epidemiological, *in vivo*, and *in vitro* studies have been utilized to investigate the role of the ovary in HGSOC progression [6-8]. Epidemiological studies are useful for identifying risk factors for ovarian cancer, but these studies only show correlation and cannot pinpoint a specific mechanism of disease progression. Mouse models can identify causative factors contributing to HGSOC progression and allow for recapitulation of the tumor microenvironment; however, these models are expensive and do not easily allow perturbation of a single variable within the model system. *In vitro* models allow for precise control over system variables, but these models often utilize cells on tissue culture plastic or flat hydrogels and test individual exogenous factors resulting in an oversimplification of the complex ovary microenvironment.

We aimed to address the shortcomings of existing models of HGSOC progression and gain a better understanding of early stage ovarian cancer, particularly the role that ovulation and the ovary microenvironment play in the cancerous progression of HGSOC. This thesis focuses on how inflammatory factors secreted during ovulation, the extracellular matrix (ECM) composition and structure of ovarian cysts, and the physical topography of ECM substrates can induce metastatic behaviors in FTE cells, such as resistance to apoptosis and invasion. The remainder of this chapter will identify potential roles for the ovary in HGSOC metastasis and areas where we aim to further investigate the impact of the ovary microenvironment on the cancerous progression of FTE cells. A detailed overview of the ovary and the outstanding theories of the formation and metastatic cascade of HGSOC will be provided in Chapter 2, focusing on the chemical and structural microenvironmental changes that occur throughout the ovulation cycle. Chapter 3 will explore the anti-apoptotic effects of ovarian secreted follicular fluid on FTE cells, while in Chapter 4, the extracellular matrix composition and structure of ovarian cortical inclusion cysts (CICs) will be quantified, a novel model of these CICs will be developed, and the impact of the CIC microenvironment on FTE cell invasion will be investigated. Lastly, Chapter 5 will focus on the biophysical mechanism via which substrate topography of CICs facilitates curvature-induced FTE cell invasion.

1.2 Prior studies of ovarian cancer progression and topography induced cell behavior

Prior studies implicating the ovary in HGSOC [3-5] have not been able to identify the mechanisms underlying how the ovary impacts the cancerous progression of FTE cells. The ovary is a unique organ that undergoes many cycles of ovarian follicle formation, ovulation (egg release), and ovulation wound repair throughout its lifetime. These cycles are accompanied by the release of follicular fluid, a concentrated solution containing many cytokines and growth factors [9]. While the number of ovulations a woman has throughout her lifetime is correlated with increased risk of HGSOC [4], the impact of follicular fluid on the cancerous progression of FTE cells has not been characterized. This thesis utilized follicular fluid from

patients undergoing *in vitro* fertilization to study the impact of this potent solution on FTE cell anoikis resistance and invasion.

In addition to follicular fluid release, the ovulation cycle involves extensive ECM remodeling and turnover in the ovary [10]. The ECM of developing ovarian follicles has been studied from a reproductive point of view, but the ECM changes that occur during ovulation wound repair have not been characterized. Furthermore, the ECM composition and structure surrounding ovarian cortical inclusion cysts (CICs), which form from ovulation wounds and invaginations of the ovarian surface, remains unknown [8,11,12]. The exposed ECM of ovulation wounds has been shown to increase the attachment of FTE cells [5,13] and histology has revealed FTE cells trapped within ovarian CICs [14], yet the impact of this entrapment on the cancerous progression of FTE cells has not been investigated. This thesis quantified ovarian ECM composition and levels and used second harmonic generation (SHG) to examine collagen structures near CICs. Furthermore, to recapitulate both the structure and ECM composition of ovarian CICs, a microfluidic lumen platform where both the size of the lumen and the ECM composition surrounding the lumen can be precisely controlled was utilized.

Curved substrates are found throughout the body, from intestinal villi to mammary ducts to ovarian cysts, and can impact cellular behavior; however, most of the work in this area has been performed with single cells or on PDMS substrates, which do not allow cells to invade and have lower ECM density than an ECM hydrogel [15,16]. This thesis investigated the role that curvature plays on cell invasion into the ECM by developing a novel way to pattern collagen I substrates with various curvatures while allowing cells to be seeded on these substrates in confluent monolayers. Furthermore, a finite element (FE) model was used to help identify aspects of a cell monolayer that are important for curvature-based invasion and drug inhibition studies were performed to test the FE model predictions.

1.3 Key results of studies

1.3.1 Follicular fluid increases the ability of FTE cells to survive while not attached to a substrate via increased cell clustering. The purpose of this study was to determine if follicular fluid, which is released from the ovary each month during ovulation, altered the metastatic potential of FTE cells. An important step in the metastatic cascade of HGSOC is the ability of FTE cells to detach from the fallopian tube and survive in solution before attaching to secondary organs, most notably the ovary. This ability to survive while not attached to a substrate is termed anoikis resistance. In an assay designed to test the anoikis resistance of FTE cells, follicular fluid collected from patients during *in vitro* fertilization significantly decreased apoptosis of FTE cells. Furthermore, this mechanism of anoikis resistance involved clustering of FTE cells. Follicular fluid was filtered into fractions based on particle size in an attempt to isolate the component responsible for anoikis resistance, and some of the most abundant follicular fluid components known to play role in cell clustering were tested in an anoikis assay, but the exact mechanism of follicular fluid based anoikis was not determined.

1.3.2 Ovarian CICs contain a dense, aligned band of collagen I and III at their boundary and these ECM characteristics can be recapitulated in an *in vitro* lumen model. The goal of this study was to characterize the ECM surrounding CICs and develop a microfluidic device that incorporates the ECM properties of ovarian CICs. The composition of collagen I and collagen III within the ovaries of patients with HGSOC and benign conditions were measured using immunofluorescence staining. This staining revealed a dense band of collagen I and collagen III at the boundary of CICs in both patient populations. Furthermore, SHG imaging showed that the fibers in these dense bands were aligned parallel to the CIC boundary. A modified version of the LumeNEXT platform was designed to replicate the CIC environment as closely as possible – the diameter of microfluidic lumens was set near the average diameter of CICs found in human ovaries,

the dense band of collagen observed surrounding CICs was observed surrounding lumens, and the concentrations and compositions of collagen I and collagen III were set to physiologically relevant ranges.

1.3.3 The physical and chemical environment of CICs affects FTE cell invasion. In this study, FTE cells were found to undergo spontaneous and robust invasion in microfluidic lumens, but not on flat collagen gels. Adding follicular fluid, which has been hypothesized to have pro-carcinogenic effects, to the lumens increased the number of invading cells and average distance of invasion. In addition to this chemical stimulus increasing FTE cell invasion, changes to the ECM surrounding the lumens affected cell invasion. Lowering the concentration of collagen I in microfluidic devices from 7.7 mg/mL to 2.5 mg/mL (a physiologically-relevant range) significantly increased FTE cell invasiveness. Additionally, substituting collagen III into the microfluidic devices for collagen I increased FTE cell invasion. Taking together, these results show that the physical and chemical environment surrounding CICs can have a significant influence on FTE cell invasiveness.

1.3.4 Substrate curvature impacts FTE cell invasion via a cell-cell tension-based mechanism. Building off the observation that FTE cells invaded into lumens but not into flat collagen gels, a novel device was developed to pattern collagen gels with various curvatures and directly study the impact of substrate curvature on FTE cell invasion. When FTE cells were seeded to confluency on substrates with a range of curvatures, decreasing radius of curvature increased the number of FTE cells that invaded into the collagen matrix. This invasion was determined to be MMP dependent, but *Mmp* expression was unchanged between FTE cells in curved and flat regions of a collagen gel. A FE model of cells connected to each other and their substrate via springs showed that substrate curvature impacted the normal stress that cells applied to the substrate, with decreased radius of curvature increasing normal stress. Furthermore, this model predicted that cell contractility and cell-cell tension were the most important

model components for cells to generate stress on a curved substrate. These predictions were tested by using blebbistatin, EGTA, and N-cadherin blocking antibody to inhibit contractility and cell-cell contacts in *in vitro* experiments. These treatments eliminated FTE cell invasion on curved substrates, confirming that cell-cell tension is necessary for curvature-based cell invasion. Lastly, we provide evidence indicating that FTE cell invasion from curved substrates occurred in two distinct phases – a cell-cell dependent initiation step where individual cells break away from the epithelial monolayer and a MMP dependent extension of FTE cells further into the collagen gel.

1.4 Conclusions

Overall, this thesis aimed to understand the role that the ovary microenvironment has in the cancerous progression of FTE cells, including anoikis resistance and invasion, in HGSOC. To achieve this, experiments were designed to study the survival of FTE cells after they have been exfoliated from the fallopian tube and before they attach to secondary metastatic sites, the role that ovarian CICs have in supporting invasive behavior of FTE cells, and the impact that substrate curvature has on FTE cell invasion. Follicular fluid from human ovaries collected during *in vitro* fertilization, tissue sections of human ovaries, and a cell-based FE model were incorporated into these studies to improve upon the *in vitro* systems. Collectively, these models showed the potential role of follicular fluid, ovarian CICs, and substrate curvature in HGSOC progression and deepened our understanding the early stages of HGSOC.

Chapter 2: The ovary, the fallopian tube, ovulation, and HGSOC

2.1 Introduction

The human ovaries are small, intra-abdominal organs, whose primary roles are to support the development of the unfertilized egg within a follicle, release the mature egg into the female reproductive tract, and secrete hormones to prepare the accessory reproductive organs for pregnancy [17]. Ovaries consist of two zones, an inner zone called the medulla, which contains blood vessels, stromal cells, and a dense connective tissue, and an outer zone called the cortex, which comprises the follicles and a thin layer of connective tissue [17]. The outside of the ovary is covered with a layer of epithelial cells called ovarian surface epithelial (OSE) cells. The processes of folliculogenesis and ovulation occur in follicles within the ovary cortex and ultimately result in follicle rupture and the release of a fertile egg (**Fig. 2.1**) [17]. This event creates a wound in the OSE cells covering the ovary and the tissue beneath these cells. When an egg is released from the ovary, the fallopian tube, which is located adjacent to the ovary, aids in the passage of this egg to the uterus. The outside of the fallopian tube is coated with epithelial cells named fallopian tube epithelial (FTE) cells and is comprised of both ciliated and non-ciliated cells. Ciliated FTE

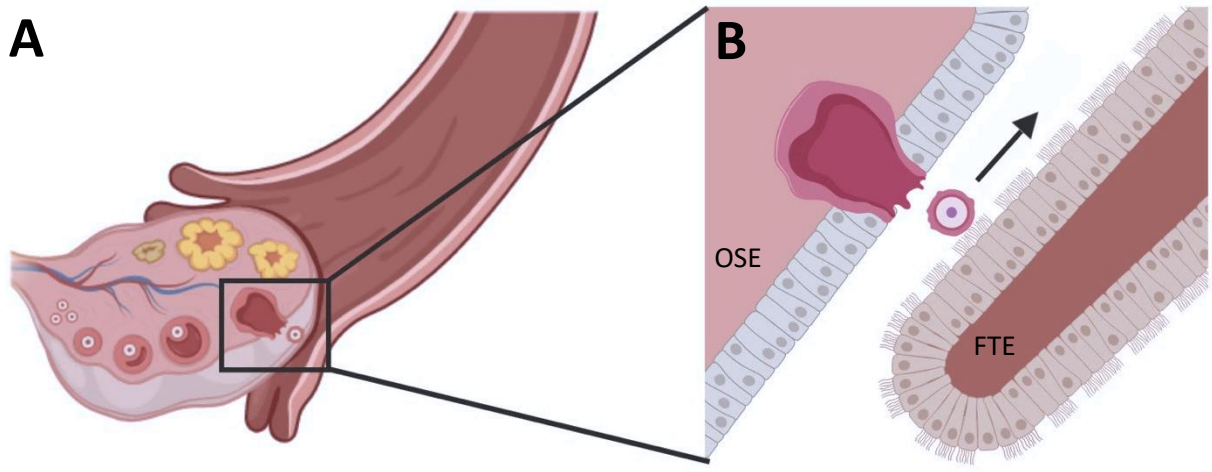

Figure 2.1: Anatomy of the ovary. A) Schematic showing the anatomical relationship between the ovary and the fallopian tube and the process of folliculogenesis within the ovary. B) Zoomed in schematic showing follicle rupture and ovulation with the released egg being swept into the fallopian tube by ciliated FTE cells. Created with BioRender.com.

cells on the distal end of the fallopian tube, termed the fimbria, are closest in proximity to the ovary and are specifically designed to sweep the egg into the fallopian tube (**Fig. 2.1**)[18].

2.2 HGSOC and the incessant ovulation hypothesis

The first theory surrounding high-grade serous ovarian cancer (HGSOC) carcinogenesis, termed the incessant ovulation hypothesis, was developed in the 1970s after it was discovered that hens that produced eggs without any breaks in ovulation developed ovarian carcinomas at a high rate [7]. The incessant ovulation hypothesis was based on the idea that the repetitive minor trauma to OSE cells, exposure of these cells to follicular fluid, and subsequent repair of the ovulation wound make ovulation a major risk factor for ovarian cancer [7]. Epidemiological data in humans supported the incessant ovulation hypothesis as a study that investigated the impact of a woman's number of lifetime ovulations – adjusted for age at menopause, age at menarche, total duration of pregnancies, duration of oral contraceptive use, and menstrual cycle length – on ovarian cancer found that each full ovulation year a woman experienced was associated with a 6% increase in ovarian cancer incidence [4]. Based on these data connecting ovulation and HGSOC, oophorectomy, or removal of the ovaries, became a common potential preventative treatment for ovarian cancer [19]. While oophorectomy did not completely abrogate the risk of ovarian cancer, it was shown to significantly reduce the risk of carcinoma development in patients with an increased hereditary risk for ovarian cancer [20]. When the link between ovulation and ovarian cancer development was tested in a mouse model of HGSOC, it was found that removal of the ovaries significantly reduced peritoneal metastasis of HGSOC tumors, while superovulation promoted ovarian tumor formation, supporting a link between the ovulation and ovarian cancer [3,5].

2.3 Ovarian surface epithelium hypothesis

In addition to the correlation between ovulation and HGSOC incidence, ovarian cancer tumors are most notably found on the ovary in patients diagnosed at earlier stages, leading to the hypothesis that the ovary was the site of origin for HGSOC [21,22]. HGSOC tumors are epithelial in origin - implicating OSE cells, the only epithelial cells in the ovary, as the potential precursor cell for ovarian cancer [23]. OSE cells are found on both the surface of the ovary and lining cortical inclusion cysts (CICs) - spherical, epithelial-lined cysts (<1 cm) found within the cortex of the ovary [11]. While OSE cells are typically quiescent, it has been hypothesized that these cells undergo epithelial-mesenchymal transition (EMT) during HGSOC initiation. This hypothesis has been supported by animal models and *in vitro* experiments demonstrating that OSE cells are capable of transforming into malignant tumors [24-28].

The first potential cause of EMT in OSE cells occurs when these cells are required to proliferate, migrate, and upregulate ECM synthesis to repair ovulation wounds following rupture of the ovarian surface [8,29,30]. Furthermore, there is evidence that inflammatory cytokines and other factors released at the ovulatory site, including EGF, TGF-β, and reactive oxygen species, could increase EMT and cause DNA damage in OSE cells [8,31,32]. The second potential source of EMT for OSE cells on the ovary is the entrapment of these cells in CICs [22]. These cysts are thought to result from either improper healing of ovulation wounds or invaginations of the ovarian surface [33], and an increase in CICs in patients with ovarian tumors has been observed [34]. It was historically hypothesized that OSE cells migrate into and become trapped in CICs as they form, and the unique microenvironment of these cysts induced the transformation of OSE cells to an invasive carcinoma [8,35]. Histological examination of ovaries surgically removed supports a role of CICs in HGSOC initiation as abnormal cell shape and cell dysplasia have been commonly observed in CICs [22,36].

Although numerous studies have shown a link between ovulation and HGSOC and abnormal cells have been observed within CICs, precursor lesions for HGSOC tumors have not been found within the ovary. The lack of precursor lesions has given many researchers pause in concluding that OSE cells are able to transition into HGSOC tumors, as small lesions on the ovary should be abundant if the ovarian surface epithelium hypothesis is correct. Furthermore, tumors formed from OSE cells in mouse models of HGOSC have displayed weak metastatic potential compared to extremely aggressive human HGSOC tumors [25,37]. Taken together, these shortcomings indicate that OSE cells may not be the cells of origin for HGSOC.

2.4 Tubal hypothesis

With the inability of to find tumor precursors on the ovary, the search for early-stage HGSOC lesions extended beyond this organ. The earliest indication that the fallopian tube was a site of origin for HGSOC came in 2001, when dysplastic lesions that histologically resembled HGSOC were found during the examination of fallopian tubes that were removed from women undergoing risk-reducing surgery [38]. In this new paradigm, called the 'tubal hypothesis', the fallopian tube epithelium undergoes malignant transformation to form precursor lesions on the distal end of the fallopian tube. Cells from these lesions are then exfoliated form the fallopian tube to the ovary where they develop into an invasive carcinoma and therefore, create the appearance of ovarian origin [39].

Since the formation of the tubal hypothesis, multiple mouse models have been developed that support FTE cells as the origin of HGSOC. The injection of human FTE cells into the peritoneum of mice induced tumors that histologically, immunophenotypically, and genetically resemble HGOSC [40]. Additionally, a model that mutated *Brca1, Tp53, and Pten* in the fallopian tubes of mice observed proliferation, loss of polarity, and cellular atypia, all phenotypes seen in HGSOC, in FTE cells on the fallopian tube. Furthermore,

these genetically modified mice formed invasive carcinomas on the ovary and throughout the peritoneal cavity that were histologically characteristic of HGSOC [3].

2.4.1 Serous tubal intraepithelial carcinoma (STIC) formation

The discovery of lesions resembling HGSOC on the fallopian tube fimbria in the early 2000s prompted additional studies examining the fallopian tubes of women at a high-risk for HGSOC [41,42]. The fallopian tube fimbria's epithelial layer is comprised of two cell types, ciliated and secretory, and there is a cyclic increase in cell ciliation at ovulation to aid in the passage of an egg into the fallopian tube [43]. In the current carcinogenic model, there is an initial loss of ciliated cells and expansion of secretory cells, which develops into a secretory cell outgrowth (SCOUT - a linear stretch of 30 or more secretory FTE cells) (**Fig. 2.2**) [44]. SCOUTs are considered benign in nature, but are more prevalent in the fimbria than the rest of the fallopian tube [44].

Figure 2.2: Schematic of FTE progression into HGSOC precursors on the fallopian tube fimbria. First a SCOUT containing at least 30 secretory cells forms, followed by the acquisition of mutated TP53 forming a p53 signature. Lastly, the FTE cells form a STIC with increased proliferation and multilayered epithelium. Created with BioRender.com.

While some SCOUTs are composed of normally functioning cells, others harbor abnormalities in gene expression. These genetic mutations in SCOUTs are believed to be the earliest indications of ovarian cancer as the progression from benign precursor lesions to HGSOC involves multiple genetic hits [45]. The mutation event most associated with HGSOC is a genetic mutation in *TP53* [46]. *TP53* encodes the tumor protein p53, which is a transcription factor and acts as a tumor suppressor by preventing cells with damaged or mutated DNA from dividing [47]. Cells with mutated *TP53* can circumvent apoptosis and

continue to divide even if the cells' DNA becomes damaged beyond repair. This genetic mutation is extremely ubiquitous in ovarian cancer as a study that sequenced tumor DNA from 145 HGSOC patients found that 97% of patients harbored a mutation in *TP53* [48]. The majority of *TP53* mutations are frameshift or nonsense mutations that cause the production of a nonfunctional p53 protein that accumulates in the cytoplasm [42]. Due to this accumulation, *TP53* mutations can be visualized as patches of secretory cells on the fallopian tube that exhibit strong immunostaining for p53 and are referred to as a p53 signature [42] (**Fig. 2.2**). These p53 signatures have been found to display positive γ-H2AX staining, but no Ki-67 staining indicating that cells have DNA damage but minimal cell proliferation [41].

The loss of *TP53* can allow SCOUTs to circumvent apoptosis, but subsequent genetic alterations are necessary for the transformation of FTE cells into a malignant lesion. The most commonly molecular events are inactivation of *BRCA1/BRCA2*, meaning women with germline mutations in either gene are at high risk for ovarian cancer [49] (**Appendix A**). Malignant lesions that form from FTE cells on the fallopian tube are called serous tubal intraepithelial carcinomas (STICs) [50,51]. STICs have been seen in continuity with p53 signatures on the fallopian tube fimbria indicating that there is a direct evolution from p53 signatures to STICs [42]. While the distinction between a p53 signature and a STIC remains somewhat arbitrary, STICs are more histologically conspicuous, extensive, and involve atypical proliferation, often resulting in multilayered epithelium (**Fig. 2.2**) [51].

2.4.2 Metastatic progression of HGSOC

While STICs are now considered the precursor lesions for HGSOC, these lesions do not develop into invasive tumors on the fallopian tube. Instead, cells from STICs are believed to undergo precursor escape, where they are exfoliated from the surface of the fallopian tube fimbria and float through the peritoneal cavity before attaching to a secondary organ (**Fig. 2.3**) [52]. The ability of cells to survive when they are

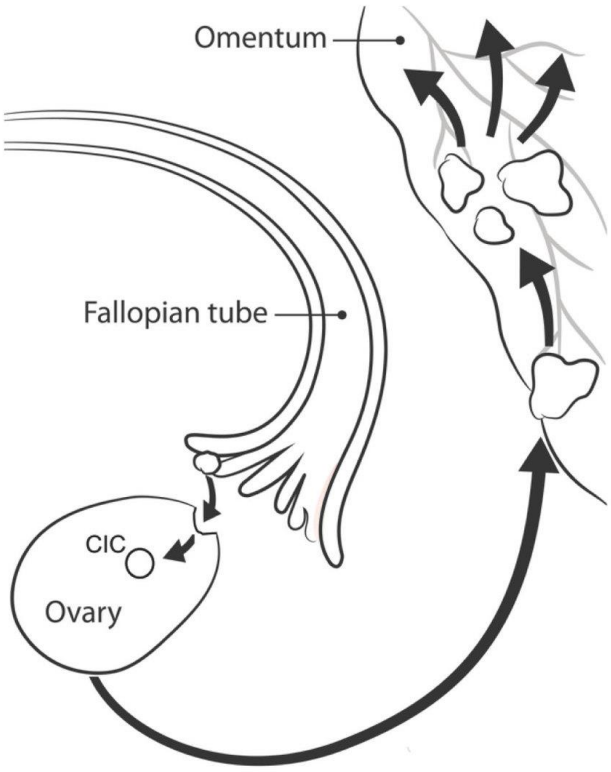

Figure 2.3: The hypothesized progression of HGSOC. FTE cells on the fallopian tube fimbria are exfoliated and embed in CICs within the ovary. The niche environment of these cysts causes the cancerous progression of FTE cells to HGSOC tumors that spread throughout the peritoneal cavity. Modified from original artwork by Jennifer Zernick.

not attached to a substrate is termed anoikis resistance and is an important step for HGSOC metastasis. In HGSOC progression, it has been found that mutant p53 increases the anchorage independent survival of FTE cells by inducing fibronectin production and fibronectin receptor signaling [53]. This thesis further investigates aspects of the microenvironment surrounding FTE cells that may increase their anoikis resistance, particularly the impact that follicular fluid has on anchorage independent survival.

The proximity of the ovary to the fallopian tube and consistent presence of HGSOC tumors on the ovary indicate that the ovary is the most likely secondary metastatic site for cells from STICs [41]. A mouse model of the tubal hypothesis supports the idea that the ovary plays an important role in metastatic spread of HGSOC. In this model, oophorectomy resulted in STIC formation on the fallopian tubes of all mice, but significantly reduced metastasis to secondary organs [3]. Furthermore, *ex vivo* experiments where ovaries were removed from mice and seeded with FTE cells showed that physical disruption of the ovarian surface with a scalpel increased attachment of FTE cells to the ovary. The exposure of the underlying ECM of the ovary was believed the be the reason for this increased attachment as FTE cells preferentially attached to collagen gels over OSE cells *in vitro* [13].

Historically, the microenvironment of CICs in the ovary was thought to contribute to the metastatic progression of cells trapped within these cysts [8,35]. With the development of the tubal hypothesis, the ability for FTE cells to become trapped within CICs became a viable question. Analysis of pathological sections revealed that both FTE cells and epithelial tumor precursors can be present in ovarian CICs [11,14]. Since CICs can only be accessed through histology, it is not known if or how the CIC microenvironment alters FTE cell behavior. This thesis investigates the physical and chemical properties of the CIC and uses a microfluidic system to recreate many elements of CICs in order to address the hypothesis that the CIC microenvironment enhances cancerous progression of FTE cells.

2.5 Extracellular matrix

A key element of the microenvironment that may impact HGSOC progression is the extracellular matrix (ECM), a three-dimensional network of macromolecules that provides structural and biochemical support to surrounding cells. There is a dynamic balance between cells and their surrounding ECM as the composition, concentration, and structure of ECM molecules can dictate cellular phenotypes including adhesion, proliferation, and invasion. In return, cells are able to remodel their surrounding ECM by secreting new ECM proteins or degrading the ECM via matrix metalloproteinases (MMPs) – a family of ECM degrading proteases [54]. In cancer, the ECM is an integral part of the tumor microenvironment, and dysregulation has been implicated in tumor progression [55]. Excess deposition, degradation, or reorganization of ECM components can disrupt the normal function of a tissue and lead to increased cell migration, invasion, or survival [56,57]. Furthermore, cancerous cells often acquire an increased ability to remodel their surroundings via increased ECM and MMP production [54]. In the ovary, the formation, development, rupture, and repair of ovarian follicles requires considerable tissue remodeling, and the ECM of the ovary is in constant turnover as it supports the many stages of folliculogenesis and ovulation

[55]. An imbalance in ECM production or degradation during ovulation wound repair or CIC formation may lead to an ECM environment that increases the cancerous progression of FTE cells.

One of the most important and widely studied ECM molecules in cancer progression is collagen. Fibrillar collagens, including collagen I and III, are the most abundant ECM proteins in many tissues, including the ovary. A single collagen molecule, termed tropocollagen, is composed of a tightly wound triple helix of amino acid chains. Tropocollagen subunits spontaneously self-assemble into a highly organized array called a fibril, which can bundle with other fibrils to form fibers [58]. The precise packing structure of collagen causes crimping of fibrils and gives collagen a wavy architecture and appearance [59]. Using second harmonic generation, a microscopy technique that allows for visualization of fibrillar collagen in tissues, researchers have investigated the organization of collagen near tumors [60]. In breast cancer, three-dimensional information about collagen fibers at the tumor-stromal interface was captured and all tumors were grouped into three tumor-associated collagen signatures (TACS) based on the density, straightness, and orientation of collagen fibers [61]. It was found that TACS could be used as a predictive biomarker for patient outcome as TACS-3 tumors, which are characterized by straight collagen fibers oriented radially from the tumor, corresponded with the worst patient prognosis [62].

In the ovary, collagen I and III are organized into concentric layers of wavy fibrils within the stroma that are aligned parallel to the epithelial boundary [63,64]. These fibrillar collagens have been found to be most abundant before ovulation, but the exact levels of these ECM proteins within the ovary cortex have not been quantified [63]. Furthermore, the structure, composition, and concentration of collagens surrounding CICs has never been investigated. In order to better understand the role that CICs play in the cancerous progression of FTE cells, this thesis attempts to build a physiologically relevant *in vitro* model of ovarian CICs. In order to accomplish this, second harmonic generation was used to gather information

about the structure of collagen surrounding CICs, and the concentration of collagens from histological samples was measured using a combination of quantitative measurements and imaging.

2.6 Follicular fluid

For ovulation to occur, follicles need to move through the stroma to the ovarian surface. This movement is generated by an osmotic pressure gradient created by the secretion of hyaluronan and chondroitin sulfate proteoglycans within follicles [65]. This process ultimately results in follicles pushing though the layer of connective tissue in the cortex, rupturing through the surface of the ovary, and releasing the contents of the follicle. In addition to a fertile egg being released, ovulation releases follicular fluid, a concentrated mixture of cytokines, growth factors, and steroid hormones, into the surrounding area. A total of 305 unique proteins were identified in human follicular fluid in a study that used high performance liquid chromatography followed by mass spectrometry to separate and identify proteins [66]. For this study and other experiments that have utilized human follicular fluid, specimens were collected from patients undergoing *in vitro* fertilization (IVF). During these procedures, women were treated with fertility drugs to increase follicle recruitment and growth, and follicles were surgically ruptured to collect eggs. During this process, the follicular fluid is collected, and is separated prior to fertilization. There is some debate in the field to the physiological-relevance of follicular fluid collected during IVF, since it is collected from patients that may have altered follicle development and is subject to the effects of the fertility medications used; however, IVF is currently the only medical procedure where human follicular fluid can be collected. Therefore, this source provides the closest approximation to follicular fluid from untreated patients that can be obtained.

During ovulation, the ovarian surface and the fallopian tube fimbria, which is adjacent to the ovary, are bathed in follicular fluid. Multiple factors in follicular fluid, including EGF, TGF-β, and reactive oxygen

species, have been shown to increase proliferation, invasion, and double-stranded DNA breaks in ovarian cancer cells, suggesting that follicular fluid stimulation may be responsible for the early cancerous progression of HGSOC [67-69]. Furthermore, primary FTE cells cultured on collagen-coated transwells and treated with human follicular fluid had increased cell proliferation and double-stranded DNA breaks as well as p53 accumulation – all hallmarks of HGSOC precursor lesions on the fallopian tube [70]. This thesis attempts to build off these findings by performing *in vitro* experiments to better understand the impact of human follicular on FTE cell anoikis survival and invasion. Anoikis survival is necessary for FTE cells to undergo precursor escape from lesions on the fallopian tube to secondary metastatic sites and invasion aids later stage metastasis of tumors; however, the impact of follicular fluid on these behaviors remains largely unexplored.

2.7 Conclusions

For many years, it was thought that HGSOC originated from ovarian surface epithelial cells; however, recent evidence suggests that HGSOC begins on the distal end of the fallopian tube. In this new paradigm, there is an initial loss of ciliated cells, expansion of secretory cells forming a SCOUT on the fimbria, acquisition of a *TP53* mutation, and malignant transformation to a STIC. Cells from these lesions then undergo precursor escape as they are exfoliated from the surface of the fallopian tube and display anchorage independent survival before attaching and forming metastatic tumors on the ovary and throughout the peritoneal cavity. Evidence supports that even for the tubal hypothesis, the ovary has a definitive role in disease progression. Ovulation appears to be linked to HGSOC advancement based on epidemiological data and the elements of the ovulatory microenvironment that have the potential to impact tumor development: extensive ECM turnover, the contents of follicular fluid, and the unique structure of the CIC. This thesis uses pathological analysis and *in vitro* models to identify and replicate the microenvironment of CICs and investigate steps in the metastatic cascade of HGSOC including the impact

of follicular fluid on the anoikis survival of FTE cells and the influence of the CIC microenvironment on FTE cell invasion.

Chapter 3: Human follicular fluid enables human FTE cells to evade anoikis

3.1 Introduction

Cells within a tissue must collectively balance growth, expansion, migration, and apoptosis in order to maintain homeostasis and proper tissue function [71,72]. To maintain this equilibrium, cells receive and integrate information from cell-matrix, cell-cell, and soluble factor signaling to ultimately determine cellular behavior [73]. Integrin receptors act as mediators of cell-ECM interactions by providing a physical connection between the ECM and the cellular cytoskeleton, transducing signals from the matrix [74]. Similarly, cadherins – calcium-dependent cell-cell adhesion receptors – help transfer information between cells, while soluble factors modulate cell phenotype by activating signaling cascades [75,76]. As these biochemical and biophysical signals direct cellular phenotype, drastic changes in these inputs will commonly trigger cell apoptosis [73]. One example of how microenvironmental changes can lead to cell death is anoikis – a form of programmed cell death induced when a cell detaches from the ECM [77]. A hallmark of cancer is the ability of cells to circumvent the traditional mechanisms of cell death including anoikis. Anchorage-independent survival of cancer cells enables metastasis by allowing cells to travel to and colonize distant organs and grow in tissues with unfamiliar ECM compositions [78]. Tumor cells have developed a variety of strategies to evade anoikis including the production of ECM, modification of their integrin repertoire, upregulation of N-cadherin, and activation of pro-survival signaling pathways [79-81].

The hypothesized metastatic progression of HGSOC involves FTE cells escaping precursor lesions on the fallopian tube and populating the ovary and other organs throughout the peritoneal cavity [39]. A woman's number of lifetime ovulations has been shown to be correlated with her risk of ovarian cancer, and ovulation has therefore been a major focus for HGSOC research [4,20]. The repetitive release of follicular fluid is thought to contribute to the transformation of FTE cells into malignant lesions on the fallopian tube fimbria, as studies have shown that proteins in follicular fluid can lead to the increased

proliferation and migration of FTE cells [67-69]; however, the impact of follicular fluid on the metastasis of these cells beyond the fallopian tube has not been investigated. We hypothesized that follicular fluid will activate anti-apoptotic signaling pathways within FTE cells that allow these cells to evade anoikis and survive while not attached to an ECM substrate. The acquisition of anchorage-independent survival is critical for FTE cells to metastasize to the ovary and other organs within the peritoneal cavity.

3.2 Materials and methods

3.2.1 Cell lines and reagents

Unless otherwise stated, all reagents were purchased from ThermoFisher (Waltham, MA). Human FTE cells that have been immortalized with TERT and overexpress a loss of function, dominant negative $p53^{R175H}$ protein were obtained from Dr. Ronny Drapkin at the University of Pennsylvania [82]. Cells were maintained at 37°C in 5% CO_2 in DMEM/F-12 with L-Glutamine, 2% Ultroser (Pall; New York, NY), and 1% Pen Strep.

3.2.2 Collection and processing of follicular fluid

Through a protocol approved by the Institutional Review Board at the University of Wisconsin-Madison (IRB No. 2016-1082, deemed not human subjects material), human follicular fluid was collected at Generations Fertility Clinic (Middleton, WI) during *in vitro* fertilization procedures and frozen at −80 °C. Follicular fluid was collected from patients undergoing *in vitro* fertilization, which is currently the only procedure where this fluid can be obtained. It is unknown if the use of hormonal stimulation alters the composition of follicular fluid; however, follicular fluid is not retrieved for any other purpose besides egg collection for *in vitro* fertilization. Follicular fluid was thawed on ice and centrifuged at 1200*g* for 10 minutes to remove cell debris. Follicular fluid was then diluted to a final concentration of 6% in SFM based on previous studies [69], and SFM containing 6% PBS served as a vehicle control.

3.2.3 Anoikis assay

Six-well tissue culture plates (Corning) were coated with 950 µL of sterile filtered polyHEMA (Sigma) and allowed to dry with the lid off in a laminar flow hood overnight. The following day, FTE cells expressing a $p53^{R273H}$ protein were trypsinized, quenched with media, spun down at 1000 rpm for five minutes, and resuspended to 100,000 cells/mL in serum free media (SFM) containing any experimental factors. Two mL of cell solution was then added to each polyHEMA coated well and placed in an incubator for 24 hours.

3.2.4 Interventions in anoikis assay

To determine if exogenous factors played a role in anoikis survival of FTE cells, specific interventions were diluted in SFM, and FTE cells were resuspended in these solutions before plating the cells on polyHEMA coated plates. Human fibronectin (Corning; Corning, NY) was added to SFM at a final concentration of 100 µg/mL while EGTA was added at a final concentration of 5 mM and H_2O_2 was added at a final concentration of 10 µM. In a similar fashion, RGD peptide (Sigma), chondroitinase (Sigma), hyaluronidase (Sigma), N-acetyl-L-cysteine, and TGFβR1 blocking peptide (Tocris) were added to cells in SFM containing 6% follicular fluid at a final concentrations of 1 mM, 1 Unit/mL, 5 Units/mL, 30 µM, and 5 µM respectively, and the cell solution was incubated on a rotator at three rpm for one hour at 37°C before seeding on polyHEMA coated plates. For β-catenin siRNA, cells were transfected with SMARTpool: ON-TARGETplus *CTNNB1* siRNA (Dharmacon; Lafayette, CO) following the manufacturer's protocol for 48 hours before seeding cells on polyHEMA coated plates. Knockdown of β-catenin between 48 and 96 hours was confirmed by Western blotting analysis. Membranes were blocked with 5% normal goat serum and 1% BSA (Sigma), probed with anti-β-catenin (8814s, Cell Signaling Technology; Danvers, MA) at 1:1000, detected with Goat Anti-Rabbit IgG H&L (HRP) (ab6721, Abcam; Cambridge, UK) at 1:1000 and Clarity Western ECL (Biorad, Hercules, CA),

and imaged on an Odyssey Infrared Imaging System (Li-Cor, Lincoln, NE). All bands were normalized to GAPDH levels.

3.2.5 Flow Cytometry

FTE cells were collected by pipetting the cell solution from the polyHEMA coated wells though a 40 μm filter. Each well was washed twice with PBS to collect any remaining cells and the wash solution was also filtered and added to a conical tube containing the cell solution. As a control, FTE cells seeded on TCP were trypsinized, quenched with media, filtered, and collected in a conical tube. The tubes containing cell solution were spun down at 1000 rpm for five minutes to pellet the cells and the remaining solution was aspirated taking extra caution to not disturb the cell pellet. Cells were then resuspended in 150 μL of flow buffer (10 mM HEPES, 140 nM NaCl (Sigma), 2.5 mM $CaCl_2$, and pH 7.4) containing 0.5% propidium iodide and incubated for ten minutes protected from light before running flow cytometry. Propidium iodide expression was measured on a ThermoFisher Attune flow cytometer and analyzed using FlowJo (FlowJo LLC; Ashland, OR).

3.2.6 Immunofluorescent imaging

For immunofluorescent images, FTE cells were stained with 2 μM CellTracker™ Green following manufacturer's directions prior to seeding cells for the anoikis assay. Images were taken on a Zeiss Axio Observer.Z1 inverted microscope with an AxioCam 506 mono camera, Plan-Apochromat 5x air objective, and Zen2 software (Zeiss; Oberkochen, Germany). Images were stitched together and the average size of cell clusters was measured using FIJI software [83].

3.2.7 Separation of follicular fluid

To separate follicular fluid into fractions based on molecular weight, 4 mL of follicular fluid was added to an Amicon Ultra-4 Centrifugal Filter Unit (Sigma) and centrifuged at 7,500*g* for 15 minutes. Both the flow through and the concentrate were resuspended to 4 mL in PBS before use in anoikis experiments.

3.2.8 PCR

RNA was collected and isolated using the Micro-RNeasy Extraction kit (Qiagen), and cDNA was synthesized using the Qiagen FirstStrand Kit according to manufacturer's instructions. Gene expression of ECM proteins was measured using an Extracellular Matrix and Adhesion Molecules RT^2 Profiler PCR array (Qiagen) following the manufacturer's instructions. qRT-PCR was performed using SsoAdvanced Universal SYBR Green Supermix (Bio-Rad; Hercules, CA). PCR was run on a CFX real time PCR machine (Bio-Rad) for a total of 40 cycles and three samples were run in duplicate for each condition. Data is expressed as fold change.

Which array

What RTPCR

3.2.8 Statistical Analysis

Data are presented as mean ± standard deviation. Statistical calculations (two-sided t-test and paired t-test) were performed using GraphPad Prism software (La Jolla, CA).

3.3 Results and discussion

3.3.1 Follicular fluid decreased anoikis in human FTE cells expressing a mutated $p53^{R175H}$ protein

During ovulation, follicular fluid is released from follicles on the ovary and the surrounding tissue, including the fallopian tube fimbria, is bathed in this solution. Follicular fluid has historically been thought

to play a role the metastatic progression of FTE cells into STIC lesions on the fallopian tube, but the possibility for a role in precursor escape and the survival of FTE cells after exfoliation from the fallopian tube requires further investigation. Since a genetic mutation in *TP53* is known to occur very early in the formation of STIC lesions on the fallopian tube [48], we chose to study anoikis in human FTE cells that have been immortalized with TERT and overexpress a loss of function, dominant negative $p53^{R175H}$ protein, since it is likely that *TP53* mutations occur before cells are exfoliated from the surface of the fallopian tube. Furthermore, it has previously been found that the production of a non-functional p53 protein in FTE cells increased anoikis resistance *in vitro* [53].

While a mutation in *TP53* has been shown to activate the anchorage-independent survival of FTE cells [53], the role that follicular fluid plays in this process remains unknown. Therefore, our lab investigated the impact of follicular fluid on human FTE cell anoikis using an *in vitro* assay designed to prevent the attachment of cells to a substrate for the extent of the experiment. When FTE cells were forced to stay in suspension for 24 hours, approximately half of cells stained positive for propidium iodide (PI), indicating necrosis or late apoptosis (**Fig. 3.1**). When cells were treated with 6% follicular fluid for the duration of the anoikis experiment, the percent of PI positive cells dropped significantly, indicating that follicular fluid decreased anoikis in human FTE cells (**Fig. 3.1**).

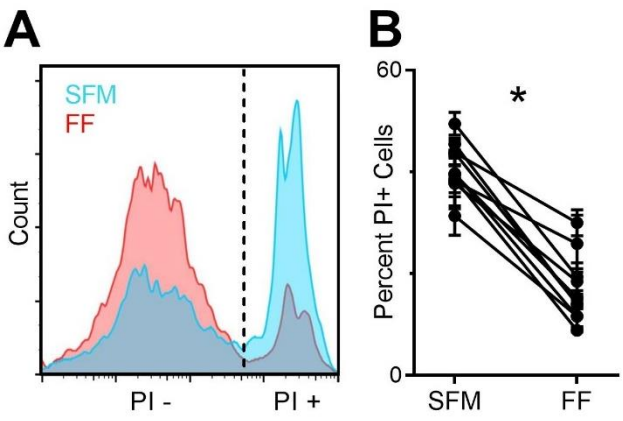

Figure 3.1: Impact of follicular fluid on anoikis. A) A representative example of flow cytometry data captured from *TP53* mutated FTE cells. Dashed line represents the cutoff between PI negative and PI positive cells. B) Follicular fluid decreased the percent of PI positive FTE cells. n = 4 per patient and 10 patients (represented by connected dots), * indicates $p < 0.05$ by paired t-test.

3.3.2 EGTA reversed follicular fluid-based clustering of FTE cells and anoikis resistance

A study that preformed proteomic analysis of human follicular fluid from three separate patients found that follicular fluid contained 305 unique proteins [66]. Many of these proteins activate cellular processes including receptor signaling and adhesion, making the list of proteins that could be involved in anoikis too extensive to test individually. However, many of the pathways modulated by the proteins in follicular fluid converge on cell-ECM and cell-cell adhesion, and modifications to cell adhesion has been shown to be a major tool that cells utilize to actively evade anoikis [77]. In order to determine the impact that follicular fluid had on cell adhesion, FTE cells expressing a mutated p53 were stained with CellTracker™ and seeded in an anoikis assay for 24 hours. Six-well plates containing cells were then imaged using fluorescent microscopy (**Fig. 3.2a**) and the size of clusters were measured using image analysis software. Visually, follicular fluid caused FTE cells to organize into clusters containing approximately 50-100 cells (**Fig. 3.2a**), and measurement of cluster size confirmed that follicular fluid significantly increased the average size of FTE cell clusters (**Fig. 3.2b**) The addition of EGTA – a divalent cation chelator that disrupts both integrin and cadherin function – eliminated clustering of FTE cells, indicating that follicular fluid-based clustering was a result of cell-cell or cell-ECM adhesions (**Fig. 3.2a and 3.2b**). Furthermore, EGTA also abolished the ability of FTE cells to evade anoikis when treated with follicular fluid (**Fig. 3.2c**) indicating that divalent cation-based clustering was necessary for FTE cells to evade anoikis.

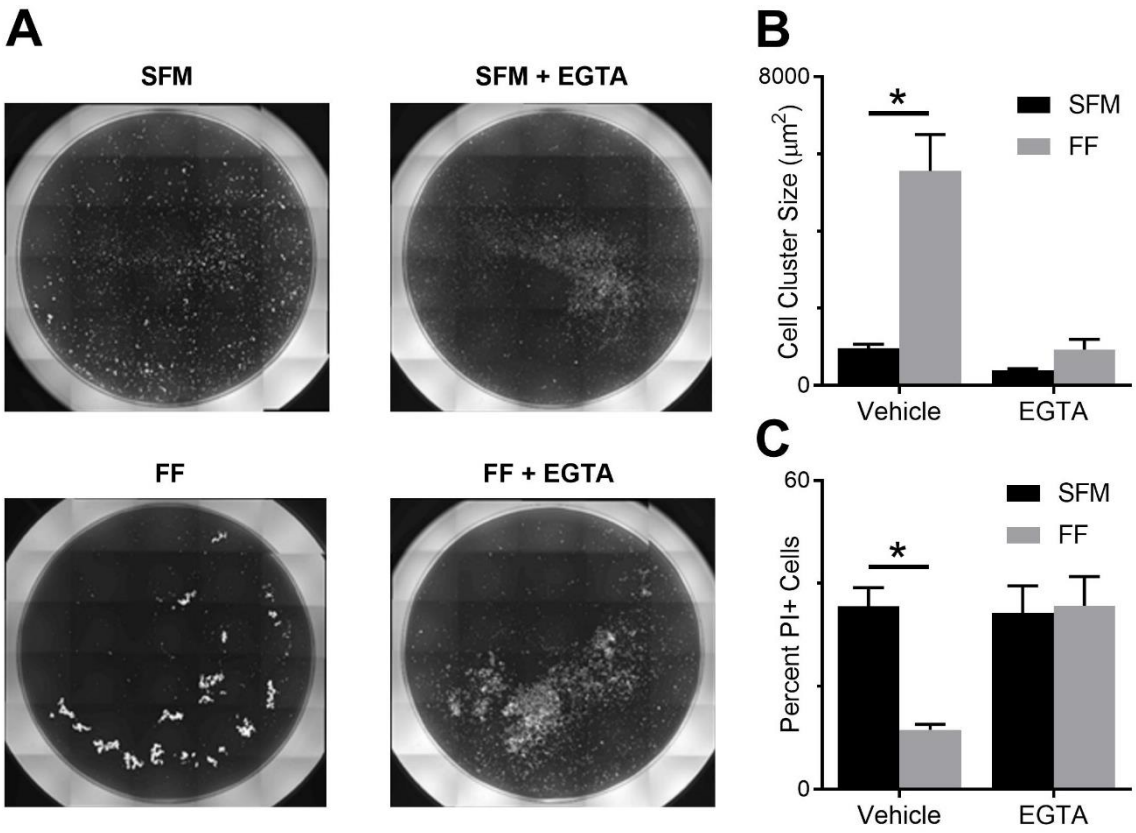

Figure 3.2: Cell clustering and EGTA in anoikis. A) Representative images showing CellTracker™ labelled FTE cells after 24 hours in anoikis assay. Visually, follicular fluid caused clustering of FTE cells and this clustering was eliminated with the addition of 5 mM EGTA. B) Quantification of clustering shows that follicular fluid significantly increased the average cluster size of FTE cells and 5 mM EGTA returned cluster size to baseline levels. n = 4 wells per condition, * indicates $p < 0.05$ using students t-test. C) EGTA eliminated follicular fluid-based anoikis resistance in FTE cells and returned the number of propidium iodide positive cells to baseline levels. n = 8 wells per condition, * indicates $p < 0.05$ using students t-test.

3.3.3 Exogenous fibronectin and RGD peptide did not impact anoikis

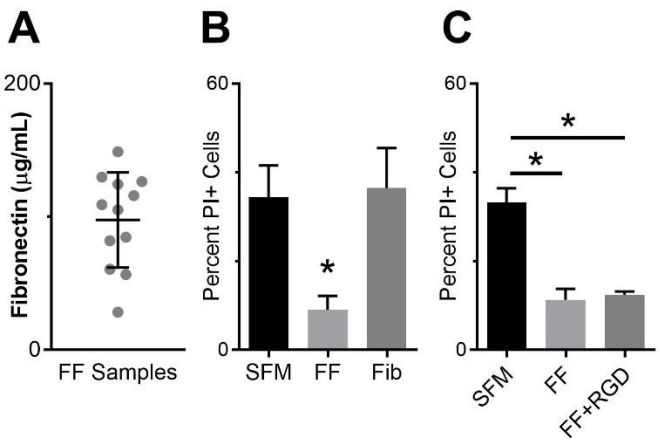

Figure 3.3: Fibronectin and RGD. A) Human follicular fluid samples have an average fibronectin concentration of approximately 100 μg/mL. n = 12 patients. B) Fibronectin did not impact anoikis survival. n = 7-8 wells per condition, * indicates $p < 0.05$ from SFM by students t-test. C) RGD peptide did not impact anoikis survival. n = 3 per condition, * indicates $p < 0.05$ from SFM by students t-test.

Since our data indicated that divalent cation-mediated cell adhesion plays a role in follicular fluid-based anoikis resistance, the impact of integrins on adhesion-independent survival warranted further investigation. It was previously found that a mutation in *TP53* decreased anoikis in FTE cells via upregulation of fibronectin and increased integrin engagement [53]. We hypothesized that follicular fluid was decreasing anoikis in FTE cells though a similar mechanism. The concentration of fibronectin in human follicular fluid samples was measured using an ELISA (**Fig. 3.3a**) and FTE cells were stimulated with exogenous human fibronectin that matched the average concentration found in follicular fluid samples. When exogenous fibronectin was added in the anoikis assay, there was no significant impact on FTE cell survival (**Fig. 3.3a**). Furthermore, the impact of integrin engagement on anoikis was investigated by blocking RGD-binding integrin receptors with soluble RGD peptide. While RGD peptide does not block all integrin receptors, it inhibits ECM binding to the majority of integrin receptors and has been shown to induce anoikis in multiple types of cancer cells [84,85]. Surprisingly, blocking RGD binding sites and preventing cell-ECM interactions did not alter anoikis in FTE cells (**Fig. 3.3b**). Taken together, these data indicate that the mechanism via which follicular fluid enables FTE cells to evade anoikis did not involve fibronectin and was likely not integrin dependent.

3.3.4 β-catenin signaling was not involved in follicular fluid-based anoikis resistance

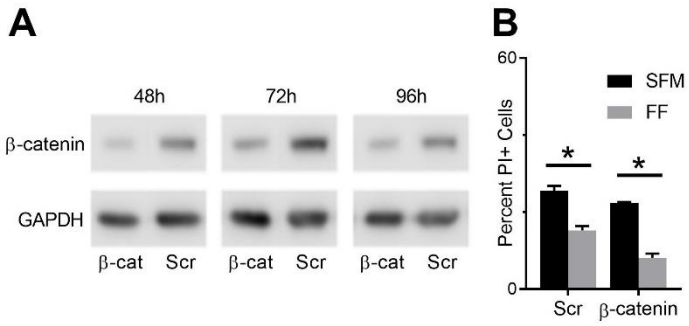

Figure 3.4: β-catenin and anoikis. A) Western blot indicating that active (non-phosphorylated) β-catenin is downregulated at 48, 72, and 96 hours. B) Knockdown of β-catenin did not impact the ability of FTE cells to evade anoikis with follicular fluid stimulation. n = 3 per condition, * indicates $p < 0.05$ by students t-test.

Since our data suggested that follicular fluid-based anoikis resistance of FTE cells was divalent cation-dependent but that integrins were not likely involved, we hypothesized that cadherins – a class of calcium dependent transmembrane proteins that stabilize cell-cell contact formation and transduce signals from other cells to the actomyosin cytoskeleton – were responsible for anoikis resistance in FTE cells [86]. To investigate the impact of cadherins on anoikis, β-catenin was downregulated in FTE cells using siRNA. β-catenin is an adaptor protein located on the cytoplasmic side of both E- and N-cadherins that helps tether these proteins to the cytoskeleton and is a key mediator in cadherin-based cell signaling pathways [87]. Furthermore, β-catenin upregulation has been observed in many types of cancer including HGSOC [88-90], and knockdown via siRNA has been shown to influence proliferation, invasion, and apoptosis of cancer cells [91]. Using siRNA to knock down β-catenin in FTE cells resulted in a reduction in active (non-phosphorylated) protein that was stable between 48 and 96 hours after transfection (**Fig. 3.4a and 3.4b**). When cells were subjected to the anoikis assay 48 hours after siRNA treatment, knockdown of β-catenin did not overturn the ability of follicular fluid to increase survival in FTE cells (**Fig. 3.4c**). Taken together, these data indicate that neither integrins or cadherins were involved in the mechanism by which follicular fluid induced FTE cells to evade anoikis.

3.3.5 ECM PCR array

Since RGD binding integrins and β-catenin were not responsible for follicular fluid-based anoikis resistance, a PCR array for ECM proteins was performed to see if any ECM proteins had altered expression after 24 hours in an anoikis assay with follicular fluid compared to SFM. This PCR array resulted in a number of proteins that were either upregulated or downregulated (**Fig. 3.5a**); however, when the upregulated proteins were tested with RT-PCR, none of these proteins were upregulated (**Fig. 3.5b**) Taken together, these data indicate that the results of our ECM array were not accurate.

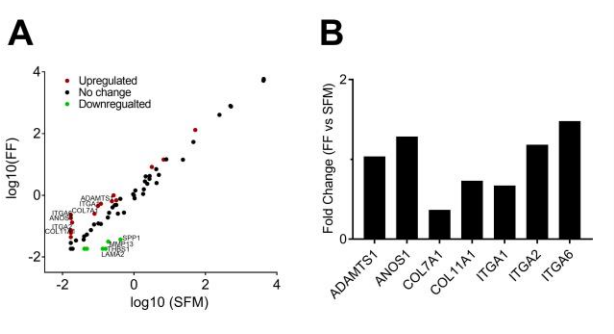

Figure 3.5: PCR array for ECM proteins. A) PCR array for ECM proteins indicated a number of upregulated and downregulated proteins. B) PCR for upregulated proteins did not confirm upregulation.

3.3.6 Fractionation of follicular fluid

Since the mechanism of follicular fluid-based anoikis resistance was unable to be deduced from inhibition of integrins and cadherins, we wanted to determine if a protein or a glycosaminoglycan (GAG) was responsible for anoikis resistance. In order to test if a protein was responsible for follicular fluid-based anoikis resistance, follicular fluid was boiled for 20 minutes at 100°C to denature proteins. Boiled follicular fluid decreased cell death of FTE cells in an anoikis assay, but not to the same extent as untreated follicular fluid (**Fig. 3.6a**). This data indicated that a protein was at least partially responsible for follicular fluid-based anoikis. Follicular fluid was unable to be

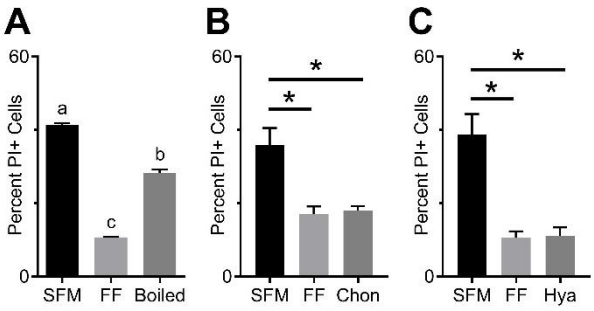

Figure 3.6: Proteins and GAGs. A) Boiled follicular fluid increases FTE cell anoikis resistance but not to the same extent as untreated follicular fluid. n = 3 per condition, different letters indicate significantly different groups by Tukey-HSD, $p < 0.05$. B,C) Neither chondroitinase or hyaluronidase impact follicular fluid-based anoikis resistance. n = 3 per condition for B and n = 8 per condition for C, * indicates $p < 0.05$ from SFM by students t-test

digested with Proteinase K since this enzymatic reaction needed to be stopped with PMSF, which is known to prevent apoptosis. Next, the impact of two GAGs, chondroitin sulfate and hyaluronic acid, which are common in follicular fluid were investigated [66]. Chondroitin sulfate was digested with chondroitinase (**Fig. 3.6b**) and hyaluronic acid was digested with hyaluronidase, but neither of these enzymes had an impact on follicular fluid based anoikis resistance. Since data indicates that a protein is involved in follicular fluid-based anoikis resistance, size filtration was used as an attempt to separate follicular fluid proteins into smaller cohorts that could be tested individually. Using a filter with a 100 kDa molecular weight cutoff, follicular fluid was separate into two factions (**Fig. 3.7a**), which were resuspended in PBS to the original sample volume. Based on previous analysis, follicular fluid contains 57 proteins with a molecular weight larger than 100 kDa and 248 proteins with a molecular weight smaller than 100 kDa [66]. When FTE cells were treated with these follicular fluid fractions in the anoikis assay, the fraction containing proteins larger than 100 kDa caused FTE cells to evade anoikis, while the fraction smaller than 100 kDa had no effect (**Fig. 3.6b**). While these data indicate that a protein in follicular fluid with a molecular weight larger than 100 kDa was allowing FTE cells to evade anoikis, size filtration filters were subject to clogging and lacked precision for separating proteins, as they are designed to concentrate a relatively pure protein solution. Furthermore, no filters with molecular weight cutoffs between 100 and 200 kDa exist, making it difficult to further separate the 47 proteins in the large follicular fluid fraction based on size.

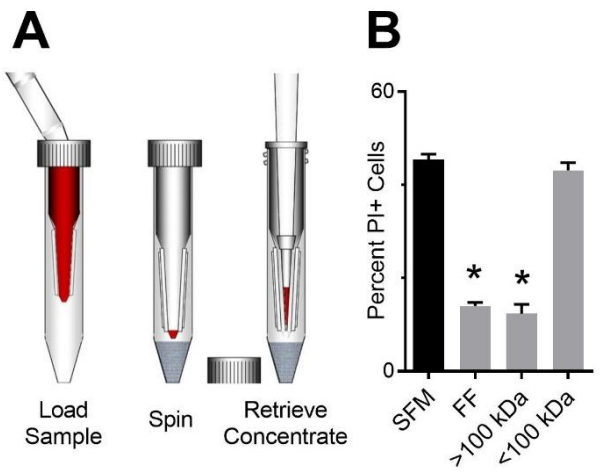

Figure 3.7: Size filtration of follicular fluid. A) Schematic showing process of filtering follicular fluid based on molecular weight (Modified from original artwork by Millipore). B) The fraction of follicular fluid larger than 100 kDa caused FTE cells to evade anoikis while the fraction smaller than 100 kDa did not impact anoikis. n = 4 per condition, * indicates $p < 0.05$ from SFM by students t-test.

3.3.7 Reactive oxygen species and TGF-β

Follicular fluid is known to contain reactive oxygen species [92], and the impact of reactive oxygen species on anoikis was investigated by adding exogenous H_2O_2 and inhibiting reactive oxygen species in follicular fluid with N-acetyl-L-cysteine (NAC). Neither H_2O_2 or NAC had an impact on anokis resistance (**Fig. 3.7a**). Additionally, the impact of transforming growth factor-beta (TGF-β) on anoikis was also evaluated since this protein has been shown to impact anoikis in colorectal cancer cells [93]. When the impact of TGF-β on FTE cell anoikis was investigated by blocking the TGF-β receptor 1 (TGFβR1) with a blocking peptide, this blocking peptide did not impact follicular fluid based anoikis (**Fig. 3.7b**).

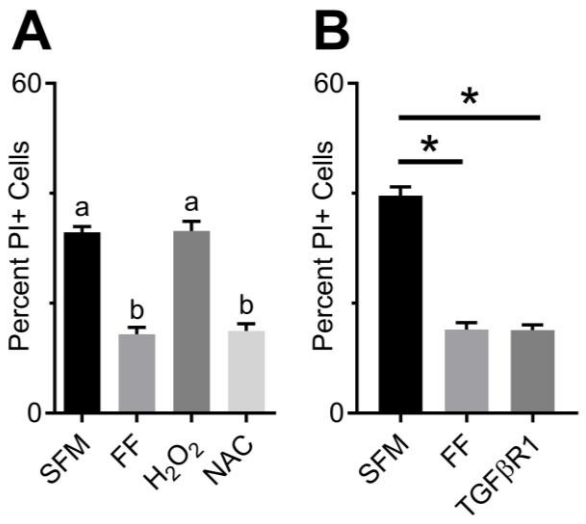

Figure 3.7: Reactive oxygen species and TGF-β receptor 1. A) Neither H_2O_2 or N-acetyl-L-cystine have any impact of follicular fluid based anoikis resistance. n = 4 per condition, different letters indicate significantly different groups by Tukey-HSD, $p < 0.05$. B) Blocking TGF-β receptor 1 with a blocking peptide did not impact follicular fluid based anoikis resistance. n = 4 per condition, * indicate $p < 0.05$ from SFM by students t-test.

3.4 Conclusions

In conclusion, our data indicate follicular fluid caused FTE cells to evade anoikis, an attribute indicative of cancer that may allow these cells to more easily metastasize from the fallopian tube to organs throughout the peritoneal cavity. While experiments indicated that the mechanism of follicular fluid-based anoikis resistance involved divalent cation-based clustering of cells, further investigation into integrins and cadherins did not implicate these adhesion receptors in anoikis resistance. In attempt to narrow down the set of proteins in follicular fluid that could be responsible for anoikis resistance, patient samples were separated with a 100 kDa filter. This experiment revealed that the component in follicular fluid responsible

for allowing FTE cells to evade anoikis was larger than 100 kDa, but further studies still need to be performed to determine the exact mechanism of follicular fluid-based anoikis resistance of FTE cells.

Chapter 4: The Extracellular Matrix of Ovarian Cortical Inclusion Cysts Modulate Invasion of Fallopian Tube Epithelial Cells

4.1 Abstract

A growing body of research supports the idea that the fallopian tube epithelium (FTE) is the precursor for most high-grade serous ovarian carcinomas (HGSOC) but that the ovary plays a critical role in tumor metastasis. Cortical inclusion cysts (CICs) in the ovarian cortex have been hypothesized to create a niche environment that plays a role in HGSOC progression. Through histological analysis of pathology samples from human ovaries, we determined that collagen I and III were elevated near CICs and that the collagen fibers in this dense region were oriented parallel to the cyst boundary. Using this information from human samples as design parameters, we engineered an *in vitro* model that recreates the size, shape, and extracellular matrix (ECM) properties of CICs. We found that FTE cells within our model underwent robust invasion that was responsive to stimulation with follicular fluid, while ovarian surface epithelial (OSE) cells, the native cells of the ovary, were not invasive. We provide experimental evidence to support a role of the extracellular matrix in modulating FTE cell invasion, as decreased collagen I concentration or the addition of collagen III to the matrix surrounding FTE cells increased FTE cell invasion. Taken together, we show that an *in vitro* model of CICs informed by the analysis of human tissue can act as an important tool for understanding FTE cell interactions with their environment.

4.2 Introduction

High-grade serous ovarian cancer (HGSOC) has a 10-year survival rate of less than 30%, a prognosis that has not significantly improved over the past 30 years [1]. As a result of the field's limited understanding of the early stages of disease progression, there are currently no reliable screening methods for HGSOC and over 70% of patients are diagnosed with stage III or IV tumors that have metastasized beyond the pelvis [2]. For many years, it was thought that HGSOC originated from ovarian surface epithelial (OSE)

cells; however, recent evidence suggests that HGSOC begins on the distal end of the fallopian tube [5,94,95]. In this new paradigm, fallopian tube epithelial (FTE) cells acquire *TP53* mutations and undergo malignant transformation to form precursor lesions known as serous tubal intraepithelial carcinomas (STICs) [42].

Although HGSOC likely originates on the fallopian tube, evidence suggests that the ovary still plays an important role. Epidemiologically, a woman's number of lifetime ovulations is correlated with increased risk of ovarian cancer, and birth control and multiple pregnancies are potential preventative measures [4]. A mouse model of HGSOC that originated from the PAX8-positive cells of the fallopian tube showed that, while lesions on the fallopian tube developed following oophorectomy, there was a significant reduction in peritoneal metastasis without the ovary [3]. Furthermore, a mouse model of HGSOC has shown that the ovulatory wound promotes the migration and adhesion of malignant cells to the ovary, potentially initiating the metastatic cascade [5].

One distinct feature of the ovary associated with ovulation, long thought to play a role in the progression of ovarian cancers, is cortical inclusion cysts (CICs) [96]. CICs are spherical, epithelial-lined cysts (<1 cm) found within the cortex of the ovary. These cysts are thought to form as a result of ovulation wounds to the ovarian surface as well as age-related surface invaginations [11]. OSE cells migrate into these cysts as they form, and it was hypothesized that the unique microenvironment of these cysts induced the transformation of OSE cells to an invasive carcinoma [8,35]. With recent evidence suggesting that the FTE cells, rather than OSE cells, are the precursors for HGSOC, researchers have begun to revisit the role that CICs play in HGSOC development. Analysis of pathological sections has revealed that both FTE cells and epithelial tumor precursors can be present in ovarian CICs, indicating there is still a potential link between these cysts and HGSOC development [14].

Therefore, we sought to investigate the physical and chemical elements of the CIC in order to address the hypothesis that the CIC microenvironment enhances metastasis of FTE cells. The tumor microenvironment is known to influence metastasis in breast cancer, as differences in composition and physical organization of extracellular matrix (ECM) proteins near tumors can initiate and direct cell invasion [97-99]. In the ovary, collagen I and collagen III are the main structural elements of the ECM, but these proteins are in flux due to the extensive ECM remodeling associated with follicle maturation and ovulation [63,100]. This turnover can shift the balance of ECM production and degradation and may give CICs a unique ECM composition and structure compared to other parts of the ovary. However, the levels of collagen I and collagen III in the ovarian cortex and CICs have not been reported. Therefore, we first characterized the levels of these proteins and then utilized this information to inform the design of a novel *in vitro* model of the CIC where perturbations to the CIC microenvironment could be examined.

4.3 Materials and Methods

4.3.1 Cell lines and reagents

Unless otherwise stated, all reagents were purchased from ThermoFisher (Waltham, MA). Mouse fallopian tube epithelial (FTE) cells that have been immortalized with TERT and overexpress a loss of function, dominant negative $p53^{R273H}$ protein were obtained from Dr. Joanna Burdette at the University of Illinois at Chicago [101]. Mouse ovarian surface epithelial (OSE) cells were isolated from FVB mice under a protocol approved by the University of Wisconsin School of Medicine and Public Health Animal Use and Care Committee (Animal Committee Number: M005940), following a previously established method [102]. Cells were maintained at 37°C in 5% CO_2 in MEM Alpha Modification supplemented with 10% heat-inactivated fetal bovine serum (FBS), 2 mM L-glutamine (Sigma-Aldrich; St. Louis, MO), 2 ng/mL epidermal

growth factor, 5 μg/mL insulin (Roche; Basel, Switzerland), 5 μg/mL transferrin (Roche), 5 ng/mL sodium selenite (Roche), 1.1 μg/mL gentamicin (Corning; Corning, NY), and 0.055% penicillin/streptomycin.

4.3.2 Collagen Dot Blot

Paraffin embedded samples of ovaries from women who underwent oopherectomy due to HGSOC or non-cancerous conditions were obtained from archived pathology samples through a protocol approved by the Institutional Review Board at the University of Wisconsin-Madison (IRB Number: 2016-1152). Collagen hydrogels created from collagen I (Advanced Biomatrix; San Diego, CA) or collagen III (Advanced Biomatrix) were used as controls. From each sample, a 20 μm section was cut and placed in a 1.5 mL tube and deparaffinization was performed by incubating with 1 mL of Safeclear II Xylene Substitute for 10 minutes at room temperature. The tissue and any undissolved paraffin were pelleted by centrifuging for 3 minutes at 16,000g. Safeclear washing and centrifuging was repeated two additional times until all of the paraffin was dissolved and only tissue remained. The tissue pellet was rehydrated using serial dilutions of ethanol (100%, 70% and 50%). The pellet was resuspended in 200 μL of protein extraction buffer containing 20 mM Tris-hydrochloride (Promega; Madison, WI), 2% sodium dodecyl sulphate (SDS, Boston Bioproducts; Ashland, MA), pH 8.0. Non-protein material was removed from the solution by centrifuging at 16,000g for 20 minutes at 4°C. Collagen I and III levels were quantified by dot blot [103]. Briefly, a polyvinylidene fluoride membrane (BioRad; Hercules, CA) was soaked in methanol for 1 minute and then rinsed in water for 2 minutes. The membrane was then allowed to dry and 1 μL of standard and samples were pipetted onto the membrane. The membrane was incubated at 37°C for 5 minutes to set the protein into the membrane, rinsed 3 times with tris-buffered saline (TBS, Boston Bioproducts), and blocked in TBS with 0.1% Tween-20 (TBST, Dot Scientific; Burton, MI) and 1% normal goat serum for 1 hour at room temperature. Antibodies (anti-collagen I (ab34710, Abcam; Cambridge, United Kingdom) at 1:2000 and anti-collagen III (ab7778, Abcam) at 1:5000) were diluted in blocking solution and incubated with the blots

overnight at 4°C with agitation. The membrane was rinsed three times in TBST and incubated in goat anti-rabbit IgG H&L (HRP) secondary antibody (ab6721, Abcam) at 1:2000 in blocking buffer for 1 hour. The membrane was then washed three times with TBST and three times with TBS. The blot was imaged using Clarity Western ECL Substrate (BioRad) and an Odyssey Fc Imaging System (Licor; Lincoln, NE), and analyzed using FIJI software [83].

4.3.3 Immunofluorescent staining of ovary sections

From each paraffin-embedded ovary used for collagen dot blots, 10 µm sections were cut and mounted on glass sides. The slides were deparaffinized with SafeClear II Xylene Substitute and rehydrated using serial dilutions of ethanol (100%, 95%, 70%) followed by two washes with TBST. Heat antigen retrieval was performed at 95˚C using Universal Antigen Retrieval Solution (R&D Systems; Minneapolis, MN) for 10 minutes, followed by a 10 minute incubation at room temperature. Slides were washed twice for 5 minutes each in TBS supplemented with 1% bovine serum albumin (TBSB), and the tissue sections were encircled with a PAP pen. The slides were then blocked in TBSB supplemented with 1% normal goat serum for 1 hour at room temperature. Antibodies (anti-collagen I (ab34710, Abcam) at 1:100 and anti-collagen III (ab7778, Abcam) at 1:500) were diluted in the blocking solution and incubated on the sections at 4˚C overnight. Slides were washed four times in TBSB and a goat anti-rabbit IgG H&L Alexa Fluor® 488 secondary antibody (ab150077, Abcam, 1:300) was added for 1 hour. Slides were rinsed 3 times in TBSB and sealed with ProLong® Diamond Antifade Mountant with DAPI. Imaging was performed on a Zeiss Axio Observer.Z1 inverted microscope with an AxioCam 506 mono camera, a Plan-Neofluar 10x 0.4-NA air objective, a Plan-Apochromat 20x 0.8-NA air objective, and Zen2 software (Zeiss; Oberkochen, Germany).

4.3.4 Quantification of collagen concentration

FIJI was used to measure the total area of each ovary section and this area was multiplied by the thickness of each section to obtain the tissue volume. The collagen I and collagen III concentrations from the dot blot assays were multiplied by the tissue resuspension volume (200 µL) and divided by the tissue volume to obtain total collagen concentrations. To obtain the level of collagen in the cortex, the total collagen concentration was multiplied by the average fluorescence intensity of the cortex divided by the average fluorescence intensity of the whole ovary.

4.3.5 Second Harmonic Generation Imaging

The SHG imaging system consisted of a laser scanning head (Olympus FluoView 300, Olympus, Tokyo, Japan) mounted on upright microscope (Olympus BX61), coupled to a mode-locked Titanium Sapphire laser. All measurements were carried out with a laser fundamental wavelength of 890 nm with average power of ∼20 mW at the specimen. The microscope simultaneously collected both the forward and backward components of the SHG intensity. In the former, a long working distance 40× 0.8 N.A. water-immersion objective and a 0.9 N.A. condenser provided excitation and signal collection, respectively. The backward component was collected through the excitation objective in a non-descanned configuration. In each channel, the SHG signal was isolated with a dichroic mirror and 10 nm bandpass filter (445 nm). The signals were detected by two identical photon-counting photomultiplier modules (Hamamatsu 7421, Hamamatsu, Japan).

4.3.6 Analysis of collagen alignment

CT-FIRE [104] was run on the z-stacks generated from second harmonic generation imaging to identify collagen fibers. CurveAlign [105] was then used to identify each fiber's distance from and angle relative to a manually-drawn CIC boundary. Fiber angle was binned into three groups with fibers with an angle

between 0-30° classified as parallel, 30-60° as random, and 60-90° as perpendicular. Analysis was conducted in two unique spots on each of 29 CICs from patients with benign conditions.

4.3.7 Microfluidic devices

Microfluidic lumens were made using the LumeNEXT platform [106]. Briefly, soft lithography was used to generate negative molds of the multilayer lumen device and poly-dimethylsiloxane (PDMS, Dow Corning, Salzburg, MI) prepared at a 1 to 10 curing agent to elastomer base ratio was used to fabricate the top and bottom layers of the chamber. Linear PDMS rods with a 410 µm diameter circular cross-section were created by filling 22G hypodermic needles with PDMS and removing the PDMS from the needles after curing. These circular lumen rods were inserted into the chamber and the devices were bonded to a glass surface using oxygen-plasma treatment (Thierry Corp., Royal Oak, MI). The devices were sterilized by exposure to UV light for 20 minutes, pretreated with 2% poly(ethyleneimine) (Sigma) diluted in sterile deionized water for 10 minutes at room temperature followed by 0.1% glutaraldehyde (Sigma) diluted in sterile deionized water for 30 minutes at room temperature, and washed three times with sterile deionized water.

Collagen gel preparation was carried out on ice to halt polymerization of collagen. Bovine collagen type I (Advanced Biomatrix) was mixed with 1 part 10x serum free MEM Alpha Modification media, neutralized to a pH of 7.4 with 0.2 N sodium hydroxide (Sigma), and diluted to 10 parts with sterile deionized water. The mixture was incubated on ice for 20 minutes before use. By varying the initial concentrations, gels of 2.5, 4.8, and 7.7 mg/mL were formulated. The collagen gel mixture was loaded into each device and a ring containing 200 µL of phosphate buffered saline (PBS) was added around each device to prevent evaporation. The devices were incubated at room temperature for 10 minutes followed by overnight incubation at 37°C. The following day, 5 µL of PBS was added to the small port of the lumen and the PDMS

rod was pulled out of the polymerized collagen from the larger port, resulting in a lumen structure filled with PBS inside the collagen gel. The PBS was aspirated from each lumen, and 5 µL of 1:10 Matrigel (Corning) diluted in serum-free media (SFM) was added to each lumen and incubated for 20 minutes at 37°C. The lumens were washed once with SFM before seeding cells.

4.3.8 Fluorescent labeling of collagen

To visualize collagen organization within microfluidic lumens, 5 µL of collagen-binding adhesion protein 35 (CNA35-EGFP) [107] at a concentration of 25 µM was incubated in each lumen overnight at 37°C. The lumen was then washed 5 times for 2 hours each at 37°C to remove unattached protein. The CNA35-EGFP plasmid was a gift from Maarten Merkx (Addgene plasmid # 61603).

4.3.9 Cell seeding and culture in lumens

FTE and OSE cells were stained with 2 µM CellTracker™ Green following manufacturer's directions, dissociated using trypsin-EDTA, and suspended in SFM at 100,000 cells/µL. 4 µL of cell suspension was added to each lumen through the small port and the PBS ring surrounding the device was replenished. The lumens were rotated at 3 rpm for 2 hours at 37°C, washed once with 5 µL of media to remove unattached cells, and incubated with 5 µL of media per lumen. The devices were rotated at 3 rpm throughout the experiment and the media in the lumens and PBS ring around the device were changed every 12 hours.

4.3.10 Analysis of cell invasion

A Leica TCS SP8 confocal microscope (Leica; Wetzlar, Germany) was used to image cells in the lumens. Confocal slices at the vertical midpoint of the lumen were stitched together to visualize the entire length of the lumen and quantify invasion. The number of cells that invaded the collagen from the lumen and

the distance invaded was measured in FIJI. Z-stacks were taken at a Nyquist sampling interval of 2.41 µm to generate cross-sectional images of lumens**.** Rendering of z-stacks into three dimensional images was performed using Leica LAX software.

4.3.11 Follicular Fluid

Through a protocol approved by the Institutional Review Board at the University of Wisconsin-Madison (IRB Number: 2016-1082, follicular fluid is classified as IRB exempt), human follicular fluid was collected at Generations Fertility Clinic (Middleton, WI) during *in vitro* fertilization procedures and frozen at -80°C. Follicular fluid was thawed on ice and centrifuged at 1,200g for 10 minutes to remove cell debris. Follicular fluid was then diluted to a final concentration of 6% in SFM [69] and 5 µL of this solution was added to each lumen 2 hours after seeding. SFM containing 6% PBS served as a vehicle control. As above, media in the lumens was changed every 12 hours and lumens were rotated at 3 rpm for the duration of the experiment.

4.3.12 Statistical Analysis

Data are presented as mean $\pm$ standard deviation. Statistical calculations (two-sided t-test, paired t-test, one-way ANOVA followed by Tukey-HSD) were performed in GraphPad Prism software (La Jolla, California).

4.4 Results

4.4.1 CIC boundaries contain a dense band of collagen

Paraffin embedded ovary sections from 10 patients with HGSOC and 10 patients that had their ovaries removed for benign conditions (**Table 4.1**) were stained with hematoxylin and eosin (H&E) to identify the cortex, where follicles and CICs reside (**Fig. 4.1a**). Collagen I and collagen III are the main structural components of the ovary [63] and have been known to influence metastasis in other tumor types. The distribution of these ECM proteins in the ovary was visualized by immunofluorescent (IMF) staining (**Fig. 4.1b and 4.1c**). From these images, the average fluorescent signal in the cortex was compared to the signal from the whole ovary to obtain the relative level of collagen in the cortex. These relative levels were combined with the absolute level of collagen I and collagen III measured via dot blot (**Fig. 4.2**) to obtain the average collagen I and collagen III concentrations in the ovarian cortex (**Fig 4.1d**). The concentration of collagen I in the cortex was determined to be approximately 2.9 mg/mL for benign patients and 2.1 mg/mL for HGSOC patients. The concentration of collagen III in the cortex was found to be approximately 1.5 mg/mL for benign patients and 1.7 mg/mL for HGSOC patients. These concentrations are comparable

Table 4.1: Summary of ovarian patient samples used in this study. Ages for benign and HGSOC groups are statistically significant by a two-sided t-test, $p < 0.01$. This is not surprising as the average age for diagnosis for HGSOC is 63, while most indications for removal of benign ovaries occur prior to menopause.

	Age	Race
Benign	53.4 ± 14.1	90% Caucasian, 10% Asian/Pacific Islander
HGSOC	70.9 ± 11.6	100% Caucasian

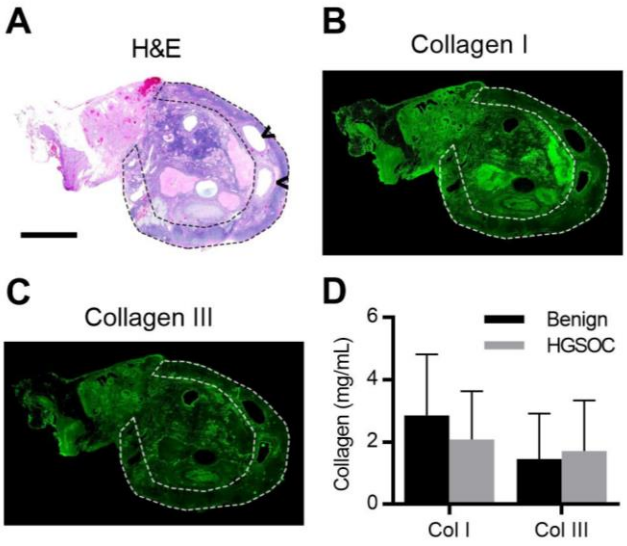

Figure 4.1: Collagen I and III in the ovary. A) H&E stain of human ovary; arrowheads indicate CICs and dotted line highlights cortex (Scale bar = 5 mm). B,C) IMF showing the distribution of collagen I and III in the ovary and cortex for the same ovary as in (A). D) Quantification of collagen I and III in the ovarian cortex, n = 10 per condition, not significantly different by two-sided t-test.

to the levels seen in other non-structural tissues [108]. Neither collagen I or collagen III concentrations were significantly different between patients with HGSOC and patients that had their ovaries removed for benign conditions.

While there were no patient-population based differences in ovarian collagen I or collagen III concentration, IMF demonstrated that there was an uneven distribution of collagens throughout the ovary. In particular, some parts of the ovary, including blood vessels (**Fig. 4.3**) and CICs (**Fig. 4.4a**) had dense patterns of collagen adjacent to their lumens. To examine this quantitatively, 29 small cysts lined with epithelial cells and contained within the ovary cortex were identified in the 10 ovaries from patients with benign conditions (1-7 CICs/ovary). Image analysis showed that CICs were surrounded by a dense collagen band with an average thickness of approximately 4 µm as measured from collagen I images (**Fig. 4.4b**) and a fluorescence intensity approximately twice that of the cortex stroma (**Fig. 4.4c and 4.4d**).

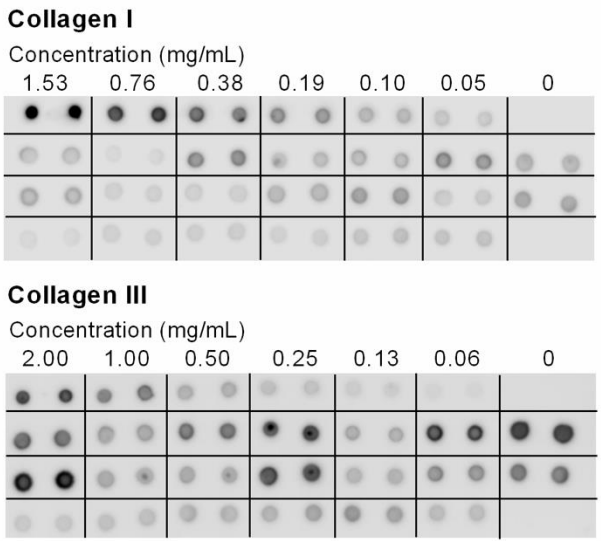

Figure 4.2: Dot blots of collagen I and III. Dot blots show the concentration of collagen I and collagen III in patient samples (bottom three rows) compared to a collagen I or collagen III standard (top row).

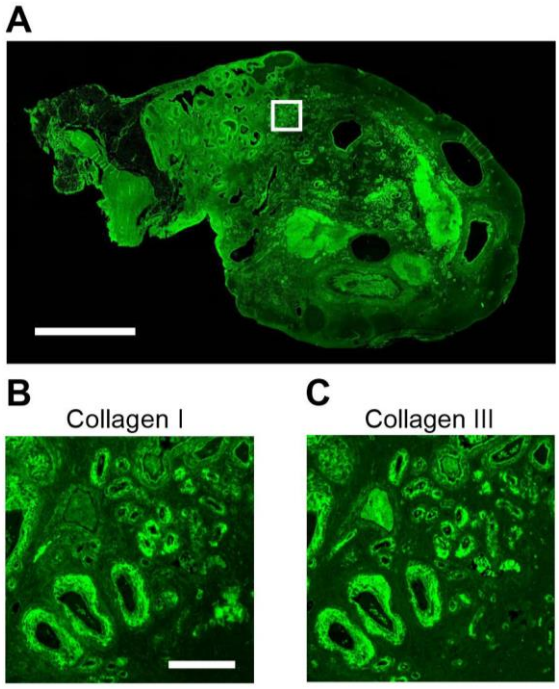

Figure 4.3: Collagen surrounding blood vessels. A) IMF for collagen I with a white box highlighting a vascular region of the ovary (Scale bar = 5 mm). B) Higher magnification image demonstrating the intense level of collagen I encircling blood vessels (Scale bar = 200 µm). C) Higher magnification image demonstrating the intense level of collagen III encircling blood vessels in the same region.

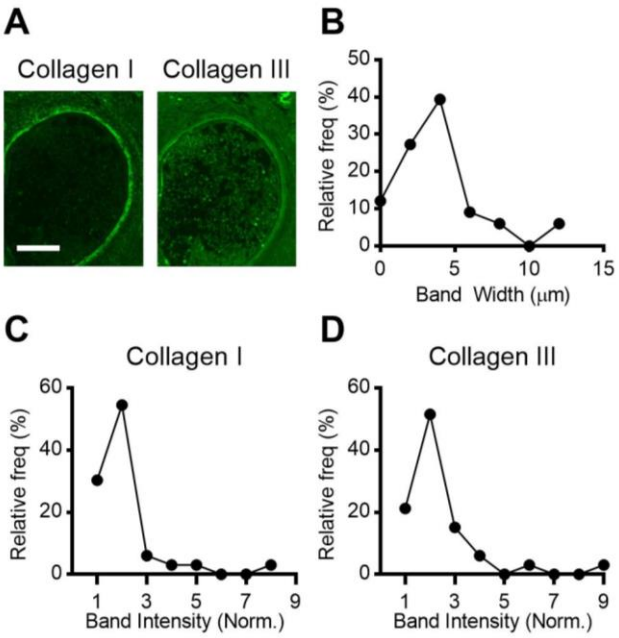

Figure 4.4: Collagen surrounding CICs. A) IMF for collagen I and III near CICs revealed a dense band of collagen surrounding CICs (Scale bar = 50 μm). B) Histogram of the width of the collagen I band. C,D) Histograms showing the relative fluorescent intensity of the collagen I and III bands compared to stroma near the cyst. For (B-D), data presented as frequency distributions from 29 CICs from 10 patients with benign conditions.

4.4.2 The collagen band in CICs is aligned parallel to the CIC boundary

In contrast to ECM composition and concentration, which could potentially inhibit or promote cell invasion, collagen alignment has been shown to increase the persistence of cell invasion in the direction of alignment [99]. To determine if the collagen band surrounding CICs has a unique alignment signature, Collagen Specific Second Harmonic Generation (SHG) Imaging was used to visualize collagen fiber structure at the CIC boundary. This imaging technique takes advantage of the nonlinearity of collagen fibers to visualize their orientation within a matrix [60]. Z-stacks of the collagen band surrounding each CIC were taken (**Fig. 4.5a**), and the images from these z-stacks were run through an algorithm designed to extract individual collagen fibers from images (**Fig. 4.5b**) [105]. Using this algorithm, we quantified fiber location and orientation, and then determined the distance and orientation of each fiber relative to a manually drawn line reflecting the CIC boundary (**Fig. 4.5c**). Collagen fibers within 10 μm of the CIC boundary were considered part of the collagen band surrounding CICs, since this distance captured the entirety of the collagen band in over 90% of CICs (**Fig. 4.5b**). Fibers further than 10 μm from the CIC boundary were considered part of the bulk stroma. Fibers in the boundary region contained a significantly higher percentage of fibers parallel to the boundary than was found in the bulk stroma (**Fig. 4.5d**).

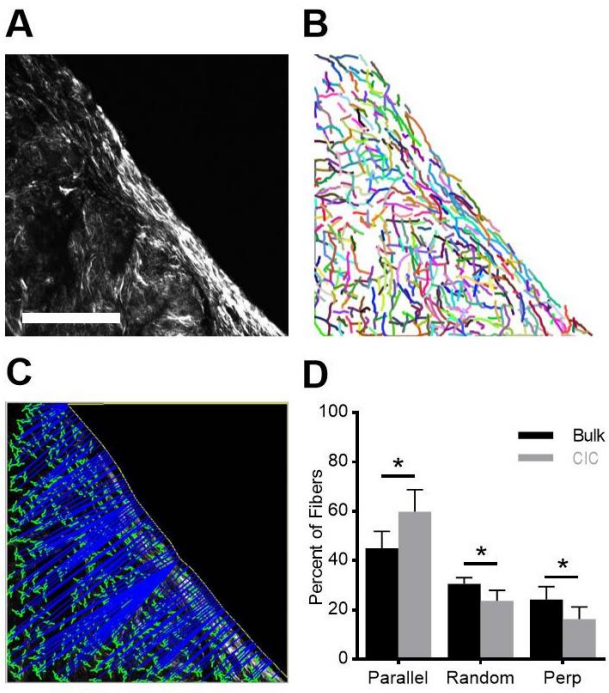

Figure 4.5: Collagen organization around CICs. A) Collagen Specific Second Harmonic Generation image of collagen at CIC boundary (Scale bar = 20 μm). B) CT-FIRE identification of collagen fibers. C) CurveAlign image identifying the angle and distance from the boundary for each fiber. D) Collagen fibers at the CIC boundary were significantly more aligned to the boundary compared to stromal fibers, data is an average of the alignment percentages found in each CIC, n = 904-6544 fibers per CIC, $p < 0.001$ between CIC boundary and bulk using two-sided t-test.

4.4.3 *In vitro* model of CICs

Due to the buried location of CICs in the ovary and randomness of their formation, it is not possible to follow the progression of FTE cells in CICs in *in vivo* models. Additionally, *in vitro* models provide flexibility to examine the impact of many physical and chemical characteristics on cellular behaviors. Therefore, we modified a microfluidic platform [106] to recapitulate the CIC microenvironment. The model consists of a cylindrical lumen embedded within an ECM hydrogel (**Fig. 4.6a**), where the diameter of the lumen and the composition of the ECM hydrogel could be altered to reflect CIC characteristics. To replicate the *in vivo* CIC environment as closely as possible, the lumen diameter was set near the average diameter measured from the 29 CICs found in human ovaries (500 μm, **Fig. 4.7a**). Although CICs are generally spherical, this cylindrical model provided a close approximation of local curvature and surface area-to-volume ratio, while enabling cells and different soluble stimuli to be added to the model. For our initial optimization, we utilized collagen I alone as it is the most prevalent ECM protein based on our measurements from human ovary sections (**Fig. 4.1 and 4.4**). To examine the ECM in the model, lumens were stained with a fluorescent collagen-binding protein, cryosectioned, and visualized. From this analysis, we determined that the lumens retained their size and shape and were surrounded by a dense band of collagen similar to the collagen I signature of human CICs (**Fig. 4.6b**). This dense band was

observed in lumens made from a broad range of collagen concentrations. Upon quantification, the collagen band's width (**Fig. 4.6c**) and normalized fluorescent intensity (**Fig. 4.6d**) were within an order of magnitude of the collagen pattern measured in human CICs.

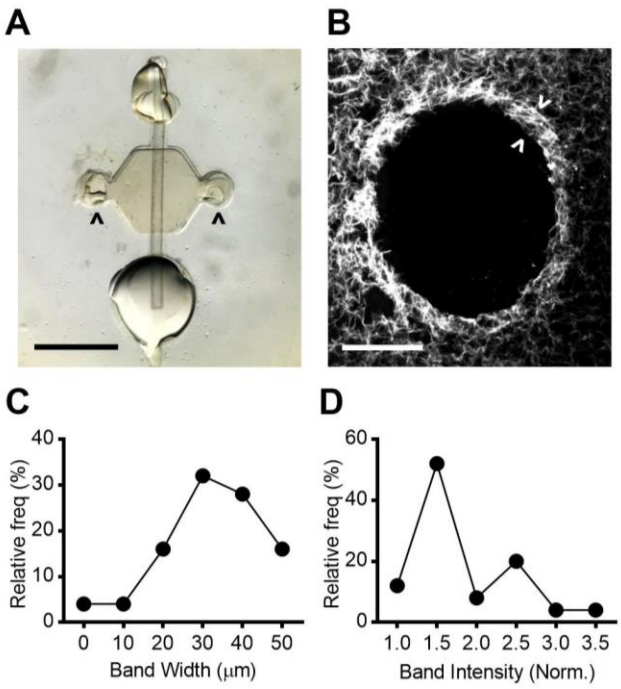

Figure 4.6: Collagen surrounding microfluidic lumens. A) Microfluidic lumen with small port (top), large port (bottom), side ports (arrowheads), and lumen rod (Scale bar = 2 mm). B) Collagen formed a dense band (arrowheads) surrounding lumens in the in vitro model (Scale bar = 200 μm). D) Histogram of the width of the collagen band. D) Histogram of the normalized fluorescent intensity of the collagen band. For (C-D), data presented as frequency distributions, n = 25 lumens.

4.4.4 FTE cells undergo robust invasion in an *in vitro* CIC model and respond to follicular fluid stimulation

The entrapment of FTE cells within CICs [14] was mimicked by seeding mouse FTE cells expressing a mutated p53 protein into our *in vitro* CIC model. Confocal microscopy showed that FTE cells formed a confluent monolayer around the entire lumen after the initial attachment period (**Fig. 4.8a**). Over the next 48 hours, FTE cells underwent robust invasion radially out of the lumen into the surrounding ECM (**Fig. 4.8b**). The pattern of invasion resembled amoeboid migration [109], as single cells broke away from the collective as they invaded out of the lumen. It is possible that secondary cells followed leader cells, as we often observed multiple cells in a line coming from the center lumen. In stark contrast to FTE cells, primary mouse OSE cells seeded in the CIC model did not undergo

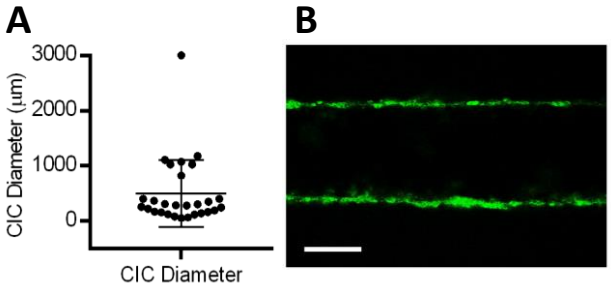

Figure 4.7: CIC diameters and OSE cells in lumens. A) Diameters of the 29 CICs found in patients with benign conditions, average CIC diameter was approximately 500 μm. B) Confocal cross-section of a lumen lined with primary mouse OSE cells showed no invasion after 48 hours (scale bar = 200 μm).

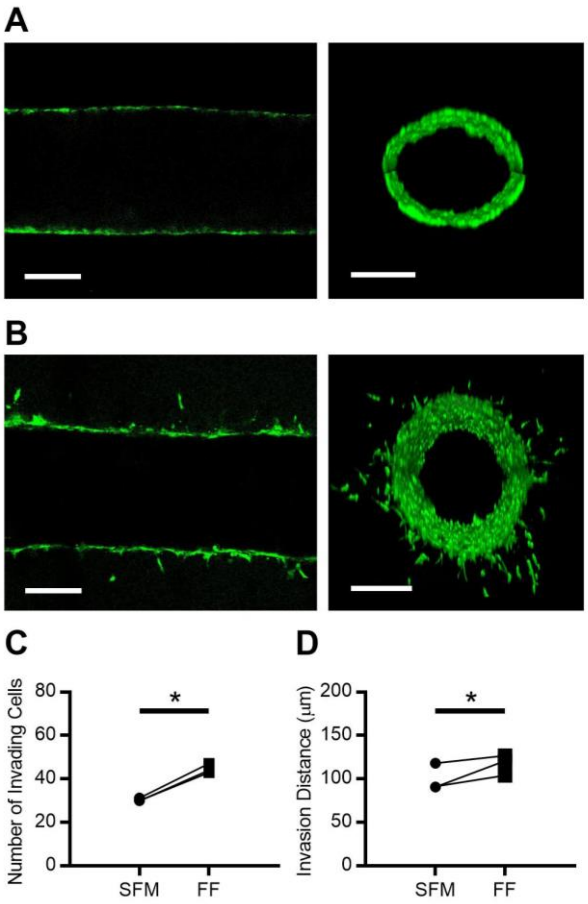

Figure 4.8: FTE cell invasion in lumens. A) Confocal slice and Z-stack cross-section reconstruction of CellTracker™ Green-labeled FTE cells in the in vitro CIC model two hours after seeding. B) Confocal slice and Z-stack cross-section reconstruction of FTE cells after 48 hours in lumen, demonstrating that individual cells migrated into the ECM from the confluent layer (Scale bar = 200 µm). C,D) Stimulating FTE cells with follicular fluid increased the number of cells that invade and invasion distance. Data in (C-D) is shown as the average per patient sample, n = 3 individual patients with 10-13 lumens/patient. * indicates $p < 0.001$ for (C) and $p < 0.01$ for (D) using paired t-test.

any invasion over 48 hours (**Fig. 4.7b**). To validate the efficacy of our model, we wanted to ensure that FTE cells seeded in microfluidic lumens would respond to chemical stimuli. We chose to stimulate cells with follicular fluid since this fluid contains a diverse and highly concentrated collection of pro-inflammatory cytokines and has been hypothesized to play an important role in HGSOC initiation [70,110]. When FTE cells in the *in vitro* CIC model were stimulated with follicular fluid collected from patients undergoing *in vitro* fertilization, there was a significant increase in the number of FTE cells that invaded (**Fig. 4.8c**) and the distance of invasion for all patient samples (**Fig. 4.8d**). While follicular fluid stimulation from different patients consistently increased invasion, both the number of invading cells (1.40-fold to 1.51-fold) and the average invasion distance (1.07-fold to 1.33-fold) varied slightly from patient-to-patient. Since ovarian CICs have been shown to contain both FTE and OSE cells [14], the impact of crosstalk between these two cell types on invasion was measured. FTE cells were seeded with mouse OSE cells at ratios of 5%, 20%, and 50% OSE cells, and the number of invading cells were measured. This experiment showed that OSE cells did not significantly impact the number of invading cells (**Fig. 4.9a**). FTE cells were tracked with CellTracker™ and

OSE cells were tracked with CellTracker™ red to and confocal imaging showed that only FTE cells and not OSE cells invaded out of lumens (**Fig. 4.9c**). To confirm this result, media that was conditioned for 24 hours on OSE cells culture on tissue culture plastic that were 50-70% confluent was added to lumens containing FTE cells and the number of invading cells was measured. Data indicated that media conditioned on OSE cells did not impact FTE cell invasion (**Fig. 4.9b**) indicating that there is not crosstalk between FTE and OSE cells that impacted the invasion of FTE cells.

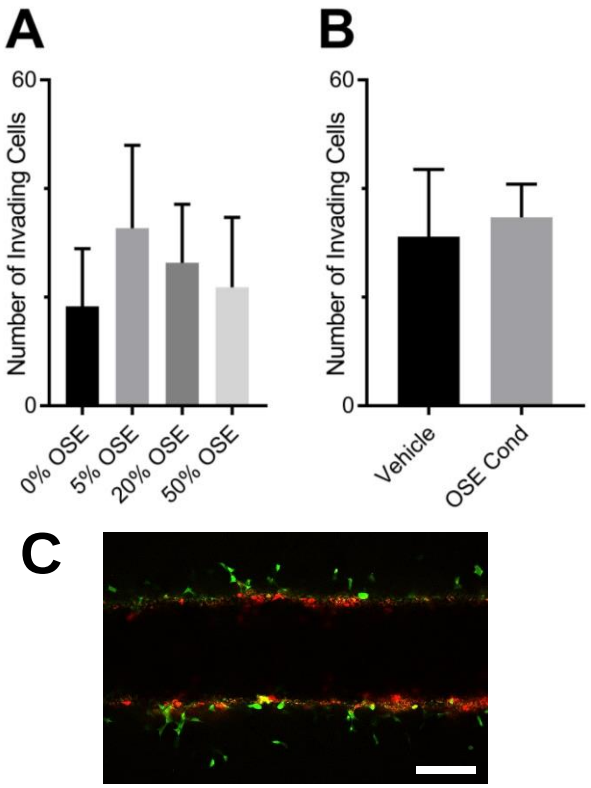

Figure 4.9: FTE and OSE co-culture and conditioned media. A) Adding 5, 20, or 50 percent OSE cells did not impact the number of FTE cells that invaded in lumens. n = 10-12 per condition. B) Media conditioned with OSE cells did not impact FTE cell invasion. n = 14. C) Confocal slice showing only FTE cells (green) and not OSE (red) invading. Scale bar = 200 µm.

4.4.5 The physical and chemical microenvironment of CICs affects FTE cell invasion

A key advantage of *in vitro* biomimetic models is that they allow the impact of microenvironmental parameters (*e.g.,* ECM concentration and composition) on cell behavior to be easily examined and quantified. Based on our observation of relatively high variability of collagen I concentration in the ovarian cortex (CV = 71%), the concentration of collagen I in the hydrogel was adjusted to concentrations between 2.5 mg/mL and 7.7 mg/mL, which is within the physiological range obtained from ovarian samples (**Fig. 4.1d**). Increased collagen I concentration significantly reduced both the number of FTE cells that invaded (**Fig. 4.10a**) and the distance of invasion (**Fig. 4.10b**) in the CIC model. Since we had observed the presence of collagen III in both the ovarian cortex and band surrounding the CIC, we next examined FTE cell invasion

into a matrix containing both collagen I and collagen III, where the total protein content remained constant. Collagen III in the matrix significantly increased the number of cells that invaded (**Fig. 4.10c**), but did not impact the average distance of invasion (**Fig. 4.10d**). Taken together, these data support that the ECM properties surrounding CICs can alter the invasive characteristics of FTE cells.

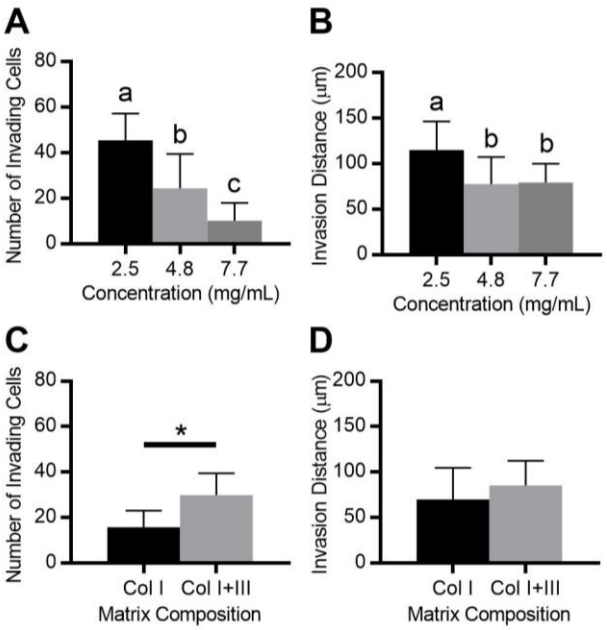

Figure 4.10: EMC properties impact FTE cell invasion. A,B) Increasing collagen density decreased the number of cells that invaded and the distance of invasion. n = 12-43 lumens per condition, different letters indicate significantly different groups by Tukey-HSD, $p < 0.01$. C,D) Incorporating collagen III increased the number of cells that invaded but did not impact invasion distance. n = 17-19 lumens per condition, * indicates $p < 0.001$ by two-sided t-test.

4.5 Discussion

The recent development of the 'tubal hypothesis' for the origin of HGSOC [42,95] has called into question the role of the ovary in this subtype of ovarian cancer. Evidence from animal models continues to support a role for the ovary in progression to advanced HGSOC [3,5] and pathological analysis has demonstrated the presence of cells resembling the putative precursor cell, the FTE, in CICs [14]. However, analyzing progression in the CIC is complicated by the inability to visualize and monitor CICs *in vivo.* The *in vitro* CIC model that we developed offers two significant advantages over animal models: 1) FTE cell behavior within this model can be analyzed in real time and 2) the components that make up this model can be modulated individually or in combination to determine how these variables impact FTE cell behavior.

To ensure our model was based on physiologically-relevant conditions, we first undertook a detailed characterization of the physical and chemical composition of the ECM surrounding CICs in human ovaries.

Using our characterization as design parameters, we developed a CIC model that reflected average CIC size and collagen I concentrations and examined the behavior of the two cell types found within CICs – the OSE and the FTE [14]. While both cell types were able to form a confluent layer covering the lumen wall, drastically different behaviors were observed over the time period examined. FTE cells with a *Tp53* mutation (the hypothesized precursors to HGSOC) underwent spontaneous and robust invasion into the surrounding ECM, while OSE cells (the native cells from the ovary) did not invade from the lumen. To our knowledge, this is the first time a phenotypical difference between FTE and OSE cells has been demonstrated *in vitro*. This contrasting behavior supports the hypothesis that the implantation of FTE in the ovary is an important step to develop advanced HGSOC tumors [111]. The wound remaining after ovulation is a likely site of FTE cell implantation, and studies have demonstrated that FTE cells preferentially adhere to the wounded ovaries compared to intact ovaries [112]. The pro-inflammatory follicular fluid milieu that is released during ovulation has been shown to promote enhanced migration and preferential adhesion of FTE cells to the ovarian stroma [5]. To further investigate the behavior of FTE in our *in vitro* CIC environment, we examined the cells response to the soluble stimuli found in follicular fluid and confirmed that FTE cells seeded within our *in vitro* model were responsive to chemical stimuli that would be present in the CIC *in vivo*.

The ECM plays a prominent role in ovarian structure and function, with collagen I and collagen III comprising the main structural components of the ovary [63]. Prior studies investigating these fibrillar collagens in the developing ovarian follicle found that collagen I and collagen III are organized into concentric layers surrounding follicles and also throughout the ovarian stroma [63,113]. Furthermore, extreme changes in the ECM surrounding follicles have been observed throughout follicle development and extensive ECM degradation and synthesis are necessary for follicle maturation and ovulation [63,65,114]. We examined the local microenvironment of the cortex to determine CIC collagen levels,

information that has not been previously reported. The elevated levels of collagen I and collagen III near CICs are perhaps not surprising since these cysts form in conjunction with the enhanced ECM remodeling that takes place during and after ovulation [115]. The levels of collagen I and III surrounding CICs were not different between normal ovaries and those with tumors, suggesting that ECM changes associated with HGSOC occur following metastasis, rather than predisposing the ovary to colonization.

Our IMF staining and quantitative results were focused on fibrous collagens that support cells and structures such as CICs in the ovary. To further examine the fibrillar structure of CICs, we used Collagen Specific SHG to visualize individual collagen fibers. The pattern of collagen fiber alignment in the stroma changes drastically with the onset of HGSOC and SHG imaging has been identified as a useful tool for differentiating normal ovarian tissue from HGSOC tumors [116]. Our analysis demonstrated that in addition to having an increased density, the fibers in the band of collagen surrounding CICs were aligned parallel to the CIC boundary at significantly higher levels than fibers in the stroma bulk. The presence of fibrous collagen has been found to not only be necessary for the invasion of breast cancer cells, but fibers regulated the extent of the MDA-MB-231 breast cancer cells invasion independent of total ECM concentration [117]. Importantly, fiber alignment has been shown to provide cues that cells respond to. *In vitro* models of aligned fibers have revealed that while fiber alignment does not affect the overall motility of cells, alignment restricts cell motility largely to one dimension [118]. Aligned fibers result in increased directional persistence of cells along the fiber direction and limit cell protrusions perpendicular to this alignment, leading to increased migrational efficiency [99]. Notably, the presence of collagen bundles aligned perpendicular to tumors has been shown to be correlated with poor patient prognosis in breast cancer [62]. Based on these observations, we would expect that collagen fibers aligned parallel to the CIC boundary likely slow invasion into the stroma.

Since FTE cells undergo extensive invasion in our *in vitro* CIC model at collagen concentrations reflective of average levels of collagen I *in vivo*, we sought to examine the impact of changes in ECM concentration. Collagen concentration has been shown to be a key mediator of tumor progression in other tumors. For example, a mouse model with increased stromal collagen in mammary tissue showed that enhanced re-organization in collagen-dense tissues facilitated significantly more invasive breast carcinomas [97]. Importantly, as collagen density increases, the bioavailability of collagen ligands increases, promoting the formation of focal adhesions [119], which allows cells to reorganize the ECM and activate downstream signaling pathways modulating cell behaviors such as invasion [120-122]. However, the impact of collagen density is not straightforward as increased collagen density has also been shown to act as a passive barrier to cell invasion unless degraded by matrix metalloproteinases [123]. In our *in vitro* CIC model, we observed an inverse relationship, with FTE cell invasion increased in lower collagen I concentrations. This behavior may help explain why HGSOC metastasis is usually not seen until post-menopause, when collagen I and collagen III production slows [100].

Our characterization of the ovary also revealed collagen III as a major structural component surrounding the CIC, where it was elevated in a pattern similar to the collagen I band. The incorporation of collagen III into a collagen I matrix has been shown to decrease the organization of collagen across several structural levels [124], which may result in a more permissive matrix for cell invasion. Indeed, when collagen III was added to the ECM in our model, FTE invasion was increased. These data suggest that imbalances in ECM turnover that increase the relative levels of collagen III could promote FTE cell invasion. While this is the first study to investigate cell invasion in collagen I/III gel mixtures *in vitro*, collagen III gels have previously been shown to increase endothelial cell angiogenesis compared to collagen I [125]. Interestingly, decreasing collagen I concentration increased both the number of invading cells and the average distance of invasion, while adding collagen III to the matrix surrounding lumens only increased the number of FTE

cells that invaded. Collagen concentration and composition have varied effects on collagen structure that could explain this observation as a less dense collagen matrix creates larger pores in an organized matrix [126], while adding collagen III to the matrix disrupts collagen fiber organization [124]. The flexibility of this biomimetic CIC model will permit additional perturbations of the ECM and soluble factors to be examined, in order to determine how elements of the CIC physical and chemical microenvironment influence the progression of metastatic FTE-derived cells to advanced HGSOC.

Chapter 5: Substrate curvature induces fallopian tube epithelial cell invasion via cell-cell tension in a model of ovarian cortical inclusion cysts

5.1 Abstract

Throughout the body, epithelial tissues contain curved features (*e.g.,* cysts, ducts, and crypts) that influence cell behaviors. These structures have varied curvature, with flat structures having zero curvature and structures such as crypts having large curvature. In the ovary, cortical inclusion cysts (CICs) of varying curvatures are found, and fallopian tube epithelial (FTE) cells have been found trapped within these cysts. FTE cells are the precursor for ovarian cancer, and the CIC niche has been proposed to play a role in ovarian cancer progression. We hypothesized that variations in ovarian CIC curvature that occur during cyst resolution impact the ability of trapped FTE cells to invade into the surrounding stroma. Using a lumen model in collagen gels, we determined that increased curvature resulted in more invasion of mouse FTE cells. To isolate curvature as a system parameter, we developed a novel technique to pattern concave curvatures into collagen gels. When FTE cells were seeded to confluency on curved substrates, increases in curvature increased the number of invading FTE cells and the invasion distance. FTE invasion into collagen substrates with higher curvature depended on matrix metalloproteinases (MMPs), but expression of collagen I degrading *Mmps* was not different on curved and flat regions. A finite element (FE) model predicted that contractility and cell-cell connections were essential for increased invasion on substrates with higher curvature, while cell-substrate interactions had minimal effect. Experiments supported these predictions, with invasion decreased by blebbistatin, EGTA, or N-cadherin blocking antibody, but with no effect from a focal adhesion kinase (FAK) inhibitor. Finally, experimental evidence supports that cell invasion on curved substrates occurs in two phases—a cell-cell dependent initiation phase where individual cells break away from the monolayer and a MMP dependent phase as cells migrate further into the collagen matrix.

5.2 Insight, innovation, integration

Curved epithelial tissues occur throughout the body, yet the impact of substrate curvature on epithelial cell behavior remains unclear. In this study, we developed 3D printed molds to pattern collagen I hydrogels with a flat surface or concave curves of different curvatures. We found that fallopian tube epithelial (FTE) cells did not invade on flat gels but underwent spontaneous invasion on curved collagen substrates, and invasion increased as curvature increased. By using a finite element (FE) model to inform experimental conditions, we discovered that cell-cell tension transmitted by N-cadherin induced the invasion of FTE cells into collagen I gels within the curve, while MMP activity regulated the distance of invasion into the matrix.

5.3 Introduction

In the human body, cells are organized into structures that give rise to unique tissues. One of the most widespread tissues is the epithelium, which is comprised of epithelial cell monolayers that line the surfaces of organs. These epithelial cell monolayers commonly cover extracellular matrix (ECM) substrates with curved topography, such as ducts in the breast, pancreas, and kidney and crypts in the small intestine [127-130]. Over the past 20 years, the field of mechanotransduction has revealed that the substrate beneath a cell can impact behaviors including proliferation, invasion, migration, and apoptosis; however, most studies have focused on how changes in substrate stiffness and ECM composition impact these behaviors in the context of flat surfaces, which by definition have zero curvature [126,131-134]. Meanwhile, the impact of substrate curvature on epithelial cell behavior has been less rigorously explored.

Initial experiments investigating the impact of substrate curvature on epithelial cell behavior cultured rat liver (IAR-2) and dog kidney (MDCK) epithelial cells as individual cells on cylindrical glass rods [135,136].

While these studies revealed that a curved substrate causes circumferential reorganization of actin stress fibers [135,136], they did not examine how substrate curvature impacts confluent layers of epithelial cells, they did not vary the magnitude of curvature, and they focused only on convex, not concave, curvatures. This information is essential to understand the impact of curvature *in vivo* as the behavior of epithelial tissues is largely controlled by the epithelial-epithelial interactions [137,138] and the structures in the body cover a broad range of curvatures. To better understand how substrate curvature impacts a monolayer of epithelial cells, more recent studies have used novel techniques to pattern concave curvatures into PDMS [139,140]. When MDCK or human colon epithelial (Caco-2) cells were cultured on PDMS substrates with curvature, cells seeded on the curved portions of the substrate detached from the substrate but retained their cell-cell connections, forming a one-cell thick bridge across the depression in the substrate [140]. This phenomenon is not seen in curved regions of epithelial tissues in the body. While this study examined only one curvature [140], evidence suggests that cell morphology is influenced by the magnitude of curvature [139].

Many human ovaries contain cortical inclusion cysts (CICs), which are spherical or oval epithelial-lined cysts found within the cortex of the ovary. CICs are thought to arise from ovulation wounds and age-related invagination of the ovarian surface [8,11,12]. While CICs are most commonly lined with ovarian surface epithelial cells, fallopian tube epithelial (FTE) cells have been found trapped within them [14]. As FTE are believed to be the precursor cell for many high grade serous ovarian cancers [39], the niche environment of these cysts has been hypothesized to aid in the progression of ovarian cancer [14]. Furthermore, CICs are an interesting model system to study the effects of curvature because these cysts shrink as they resolve, and cells in CICs are therefore subjected to increasing curvature over time [141].
We have previously developed a microfluidic lumen model of CICs, and demonstrated that FTE cells invaded into the collagen matrix surrounding the lumen [142]. We hypothesized that the increase in

curvature that occurs during CIC resolution provides a mechanism for FTE cells to transition to an invasive phenotype. To test this hypothesis, we developed a novel system of 3D printed molds to pattern varied curvatures into collagen I substrates and generated a finite element (FE) model to examine how cell-cell and cell-substrate interactions impact the behavior of cells on curved substrates. Lastly, we used a series of drug inhibition studies to test the FE models predictions *in vitro*.

5.4 Methods

5.4.1 Cell lines and reagents

Unless otherwise stated, all reagents were purchased from ThermoFisher (Waltham, MA). Mouse FTE cells that have been immortalized with TERT and overexpress a loss of function, dominant negative $p53^{R273H}$ protein were obtained from Dr. Joanna Burdette at the University of Illinois at Chicago [101]. Cells were maintained at 37°C in 5% CO_2 in MEM (Minimal Essential Medium) Alpha Modification supplemented with 10% heat-inactivated fetal bovine serum (FBS), 2 mM L-glutamine (Sigma-Aldrich; St. Louis, MO), 2 ng/mL epidermal growth factor, 5 μg/mL insulin (Roche; Basel, Switzerland), 5 μg/mL transferrin (Roche), 5 ng/mL sodium selenite (Roche), 1.1 μg/mL gentamicin (Corning; Corning, NY), and 0.055% penicillin/streptomycin.

5.4.2 Microfluidic lumen fabrication

Microfluidic lumens were made using the LumeNEXT platform [142,143]. Briefly, soft lithography was used to generate negative molds of the multilayer lumen device, and poly-dimethylsiloxane (PDMS; Dow Corning; Slazberg, MI) prepared at a 1:10 ratio of curing agent to elastomer base was used to fabricate the top and bottom layers of the chamber. Linear PDMS rods with 400 μm and 205 μm radii were created by filling 22G and 27G hypodermic needles with PDMS and removing the PDMS from the needles after

curing. These circular lumen rods were inserted into the chamber, and the devices were bonded to a glass surface using oxygen-plasma treatment (Thierry Corp.; Royal Oak, MI).

5.4.3 Collagen substrate formation around lumens

Microfluidic lumen devices were sterilized by exposure to UV light for 20 minutes, pretreated with 4% poly(ethyleneimine) (Sigma) diluted in sterile deionized water for 10 minutes at room temperature followed by 0.2% glutaraldehyde (Sigma) diluted in sterile deionized water for 30 minutes at room temperature, and washed three times with sterile deionized water. Collagen gel preparation was carried out on ice to inhibit collagen polymerization. Nine parts rat tail collagen type I was mixed with one part neutralization solution (Advanced Biomatrix; Carlsbad, CA). The mixture was incubated on ice for 20 minutes before use. The collagen gel mixture was loaded into each lumen device and the devices were surrounded by a ring of 200 μL of PBS to provide humidity. The devices were incubated at room temperature for 10 minutes followed by overnight incubation at 37°C. On the following day, 5 μL of PBS was added to the small port of each lumen and the PDMS rod was pulled out of the polymerized collagen from the larger port, resulting in a lumen structure filled with PBS inside a collagen I gel.

5.4.4 Cell seeding and culture in lumens

FTE cells were stained with 2 μM CellTracker™ Green following manufacturer's directions, dissociated using trypsin-EDTA, passed through a 40 μm cell strainer (Corning), and suspended in media at 100,000 cells/μL. The lumens were washed once with PBS, 4 μL of cell suspension was added to each lumen through the small port, and the PBS ring surrounding the device was replenished. The lumens were rotated at 3 rpm for two hours at 37°C, washed once with 5 μL of media to remove unattached cells, and incubated with 5 μL of media per lumen. The devices were rotated at 3 rpm throughout the experiment, and the media in the lumens and the PBS ring around the device were changed every 12 hours.

5.4.5 Curvature negative molds

Negative molds for collagen gels were designed using Solidworks (Dessault Systemes, Velizy-Villacoublay, France) to either have a flat or curved surface. For the curved surface the depth was kept constant at 400 µm and the radius of curvature was either 3200 µm (low curvature) or 400 µm (high curvature, equivalent to a half circle). Molds were 3D printed on a Form 2 printer (Formlabs; Somerville, MA) using Durable Form 2 Print resin (Formlabs). Molds were cleaned with 70% ethanol before each use.

5.4.6 Curved collagen substrate formation

Falcon 8-well culture slides (Corning; Corning, NY) were exposed to an oxygen-plasma treatment to make the surface of the slides hydrophilic. The culture slides were sterilized by exposure to UV light for 20 minutes, pretreated with 4% poly(ethyleneimine) diluted in sterile deionized water for 10 minutes at room temperature followed by 0.2% glutaraldehyde diluted in sterile deionized water for 30 minutes at room temperature, and washed three times with sterile deionized water. After washing, a 3D printed negative mold was placed into each well of the 8-well chamber slide.

Collagen gel solution was prepared as above, and 150 µL was loaded into each well of the 8-well culture slide in the gap between the mold and the bottom of the slide. Culture slides were placed in a 14 cm petri dish and two Kimwipes were soaked in PBS and added into the petri dish to provide humidity. The devices were incubated at room temperature for 10 minutes followed by overnight incubation at 37°C. On the following day, 400 µL of PBS was added to each well of the chamber slides and the molds were removed, resulting in collagen I substrates with either a flat surface or a concave curve (**Fig. 5.1)**.

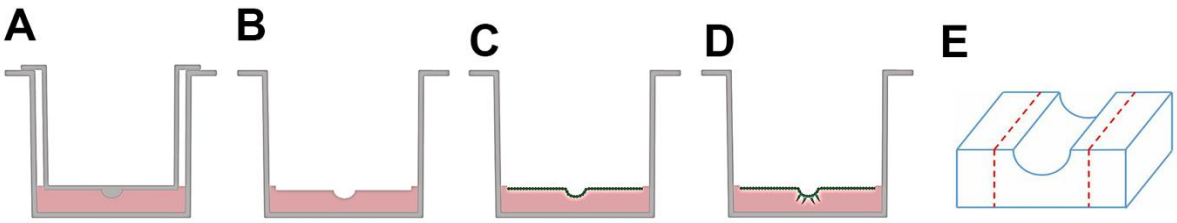

Figure 5.1: Curved collagen substrate formation. A) Schematic of a cell culture well containing a mold and collagen gel (pink) formed between the mold and the bottom of the well. B) Upon removal of the mold, a patterned collagen gel remains. C) FTE cells (green) are seeded to confluency on the collagen gel. D) FTE cells invade at the curved region of the gel. E) Schematic of collagen gel with a curved substrate that was cut into three sections for *MMP* expression quantification. Red dotted lines indicate cuts, the left and right plateau regions were combined.

5.4.7 Cell seeding on curvature devices

FTE cells were dissociated using trypsin-EDTA, passed through a 40 µm cell strainer, and suspended in media at 1.3 million cells/mL. The collagen gels were washed once with PBS, 400 µL of cell suspension was added to each curvature device, and the device was incubated on a flat surface for 10 minutes, followed by 10 minute incubations at a 30 degree angle on each side to better allow cells to attach to the sides of the curve. The flat and angled incubations were repeated one additional time and the devices were then incubated on a flat surface for five hours to allow cell-cell junctions to form. The media was changed six hours after seeding and every 24 hours throughout culture.

5.4.8 Interventions in cell invasion experiments

Specific myosin II inhibitor blebbistatin (20 µM, Sigma), focal adhesion kinase inhibitor FAK Inhibitor 14 (10 µM, Sigma), EGTA (10mM, Sigma), and MMP inhibitors GM6001 (20 µm, EMD Millipore; Burlington, MA) and batimastat (20 µM, Tocris Biosciences; Bristol, United Kingdom) were diluted in media. Unless otherwise specified, drugs were added to cultures during the initial media change (six hours after seeding). To determine the role of N-cadherin in invasion, cells were incubated with 200 µM of anti-N-cadherin blocking antibody (Clone GC-4, Sigma) or monoclonal mouse IgG1 isotype control for one hour at 37°C.

To prevent aggregation, cells were rotated at three rpm throughout the incubation. Cells were then seeded in the devices as described above and antibodies were replaced every 24 hours.

5.4.9 RT-PCR for *Mmps*

Cells were cultured on curved collagen gels for 48 hours; gels were then cut into three sections—one curved region and two plateau regions—using a razor blade (**Fig. 5.1e**). Curved and plateau regions were separated and then pooled across six collagen gels. The resulting curved or plateau samples were placed into 350 µL Buffer RLT (Qiagen; Valencia, CA), passed through a 22G needle five times, and then passed through a 27G needle five times. RNA was collected and isolated using the Micro-RNeasy Extraction kit (Qiagen), and cDNA was synthesized using the Qiagen FirstStrand Kit according to manufacturer's instructions. qRT-PCR was performed using mouse primers for *Mmp-1a, Mmp-2, Mmp-8, Mmp-9, Mmp-13, Mmp-14, and Gapdh* (all Qiagen) with SsoAdvanced Universal SYBR Green Supermix (Bio-Rad; Hercules, CA). PCR was run on a CFX real time PCR machine (Bio-Rad) for a total of 40 cycles and three samples were run in duplicate for each condition. Data is expressed as fold change, with ± 2-fold set as the threshold for significance.

5.4.10 Analysis of cell invasion

A Leica TCS SP8 confocal microscope (Leica; Wetzlar, Germany) was used to image cells in lumens and on curved substrates. For lumens, the number of invading cells were measured from a confocal slice taken at the midpoint of each lumen [142]. For cells on curved substrates, confocal z-stacks capturing the curved region of the gel and invading cells were resliced using FIJI to obtain side view z-stacks of the curved substrate (**Fig. 5.2**). Each z-stack was then projected using average intensity into a single image. From this side view, a region containing cells seeded on top of the substrate was manually outlined and deleted from the side view z-stack. The remaining z-stack contained the side view of cells that invaded into the

substrate in the region below the curve, and the distance of invasion for each cell was measured from this stack. This z-stack was then resliced and projected in FIJI to obtain a single top down image of only the invading cells. This image was thresholded using the default settings in FIJI and the number of invading cells was measured by analyzing particles larger than 40 μm^2.

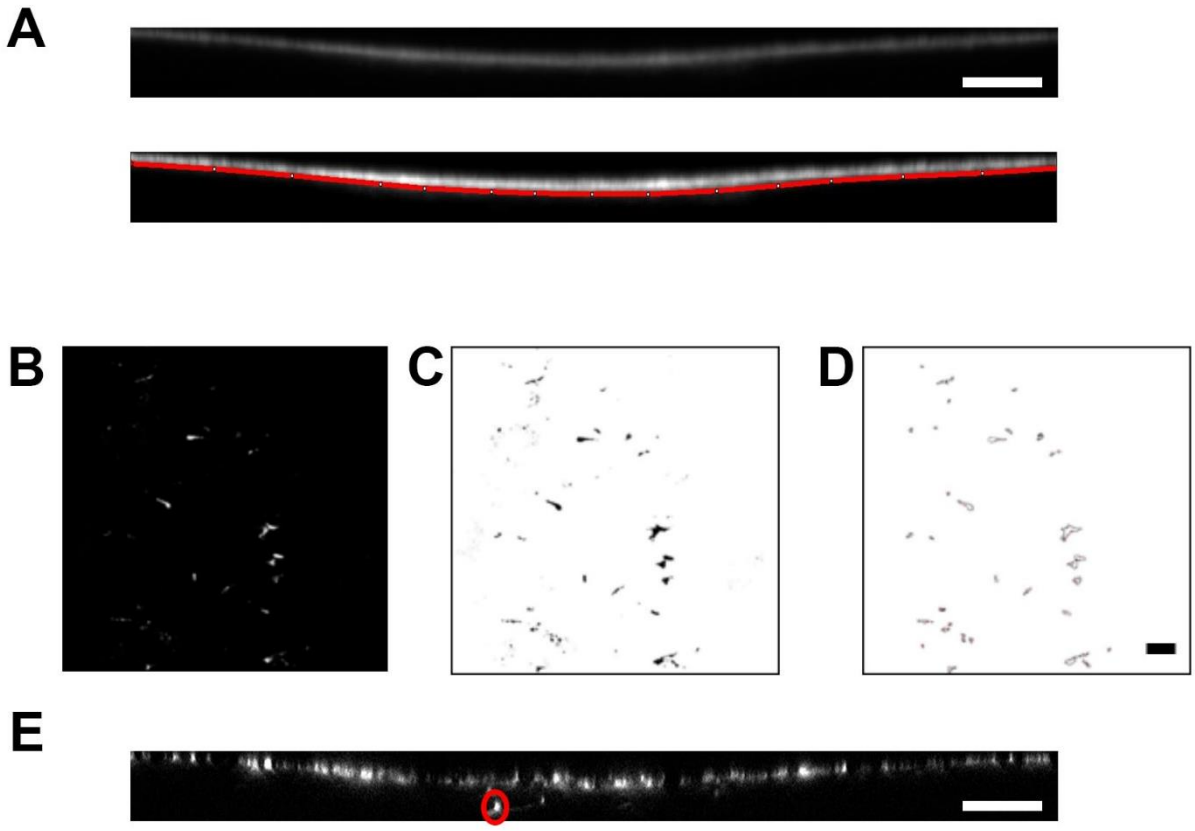

Figure 5.2: Schematic showing the process of analyzing invasion distance and the number of invading cells on curved substrates. A) The average intensity of the z-projection side view is used to manually draw the monolayer boundary (red). The area above the red line is deleted from the z-stack. B) Top down view of the z-stack after deletion of the monolayer, dots seen are individual cells that invaded. C,D) To facilitate automatic counting, cells were thresholded (C) and a cutoff of 40 μm^2 set to identify cell vs. noise (D). E) Side view z-section from original stack with an invading cell highlighted (red circle). The distance from the cell to the boundary was manually drawn and measured for each cell. All scale bars = 100 μm.

5.4.11 Finite element model

An FE model was developed in Abaqus 6.12 (Dassault Systemes, Waltham, MA) to compute the forces of cell contraction on the curved substrates. As the geometry of the experiments does not vary out of the

plane of the curve (**Fig. 5.1e**), a two-dimensional model was used. Linear, 4-node, plane stress elements were used to simulate both the cells and substrate. The substrate geometry matched the experiments with a total height of 1 mm and concave regions having radii of curvature of 3200 μm (low curvature) or 400 μm (high curvature). Each cell consisted of twelve elements and was connected to its neighbors and to the substrate with linear springs at each node [144,145]. Sensitivity studies were performed to quantify the importance of the elastic moduli used for cells and substrate. It was determined that when cells and substrate had elastic moduli of the same order of magnitude, the trends reported in the Results and Discussion section remained unchanged. Therefore, both the cells and substrate were assigned equal Young's moduli of 1 kPa and Poisson's ratio of 0.3, with the understanding that changes in these values would have minimal to no effect on the main conclusions drawn from the model. Cell contraction was simulated by imposing a thermal strain of -1 to the cell elements. Note that the product of Young's modulus and thermal strain sets the magnitude of stress in the results; increasing (decreasing) either modulus or thermal strain causes a proportional increase (decrease) in the computed stress. A symmetric boundary condition was used to simulate half of the geometry; the nodes at the bottom of the substrate were assigned a fixed boundary condition. The normal stress between cells and substrate was computed by outputting the normal force in the springs between cells and substrate and dividing by area over which each spring acted, which was equal to the product of the distance between the springs and the unit thickness. Sensitivity studies were performed to determine the range of spring stiffness that affected the results. It was found that springs with stiffness greater than 100 N/m were essentially rigid, and values of stiffness greater than this had no effect on the results. Similarly, a stiffness of 1 N/m was so compliant that smaller values also had no effect on the results. Values of spring stiffness chosen for cells and the substrate were therefore either 100 N/m (referred to as "rigid") or 1 N/m (referred to as "compliant").

5.4.12 Statistics

All data are presented as mean ± standard deviation. The number of invading cells includes the results of multiple independent experiments, with the total number of lumens/gels per condition noted in each legend. Invasion distances are provided from one representative experiment due to day-to-day variation in baseline invasion, and the number of cells per condition are provided in each legend. All experiments were performed at least twice. Statistical calculations were performed in GraphPad Prism software (La Jolla, CA).

5.5 Results and Discussion

5.5.1 FTE cell invasion increases with increased curvature in lumens

We have previously shown that FTE cells invade into collagen when cultured in a microfluidic lumen model that mimics CICs, but not when cultured on flat collagen substrates [142]. In these prior studies, lumens were made with high curvature (205 μm radius); however, histological measurements of human ovaries demonstrated that CICs encompass a broad range of curvatures. When CICs were approximated as a circle and measured, the 25th percentile radius was 112 μm, the median radius was 254 μm, and the 75th percentile radius was 605 μm [142]. CICs are hypothesized to form from ovulation wounds or invaginations of the ovarian surface, and the randomness of these processes likely result in variation in the initial curvature of CICs across patients, between CICs in the same ovary, and within a single CIC as they are not perfectly circular [146,147]. An additional source of variation in CIC curvature occurs over time, because the CIC shrinks in size as it resolves [141]. Therefore, we investigated the impact of CIC curvature on cell invasion by seeding FTE cells in microfluidic lumens with low (400 μm radius) and high (205 μm radius) curvature (**Fig. 5.3a**), which are representative of smaller ovarian CICs (**Fig. 5.3b**). The number of invading cells was measured from a confocal z-slice taken at the midplane of each lumen (**Fig. 5.3c**), and the results showed that increasing the curvature significantly increased the number of FTE cells

that invaded into the surrounding collagen I matrix (**Fig. 5.3d**). As FTE cells, the precursors for high grade serous ovarian cancer, have been observed within ovarian CICs, this observation suggests that the increase of curvature associated with CIC resolution may allow FTE cells trapped within a CIC an opportunity to escape [141].

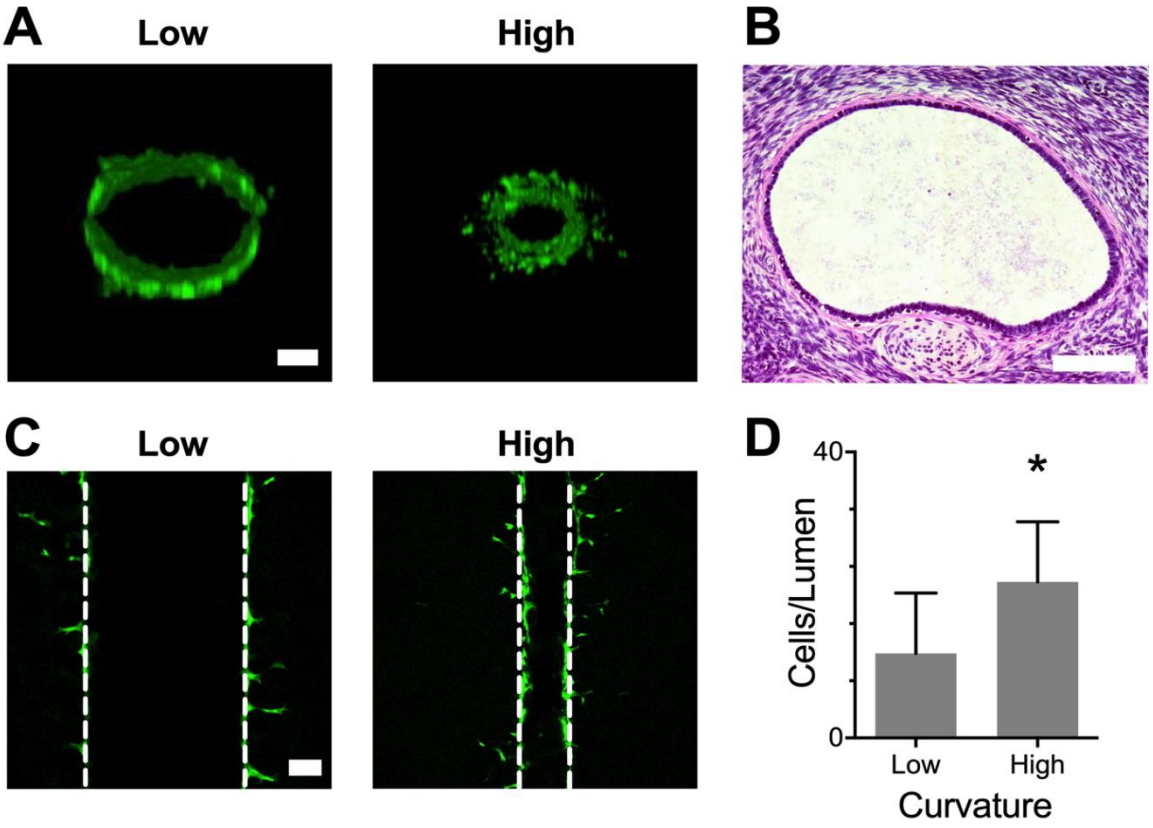

Figure 5.3: Increasing curvature increased FTE cell invasion in a microfluidic lumen model of CICs. A) Z-stack cross-section reconstruction of CellTracker™ Green-labeled FTE cells seeded in lumens with low curvature (400 µm radius) and high curvature (205 µm radius) lumens. Scale bar = 100 µm. B) H&E stain of a representative ovarian CIC. Scale bar = 200 µm. C) Confocal slices taken at the midplane of lumens with low and high curvature from which the number of invading cells were measured. Scale bar = 100 µm. D) Increasing in microfluidic lumens increased the number of invading FTE cells per lumen, n = 25 lumens for low curvature and 26 lumens for high curvature. * indicates $p < 0.0001$ using a two-sided t-test.

5.5.2 FTE cell invasion increases with increasing curvature on engineered substrates

Changing the radius in microfluidic lumens changes both the curvature of the substrate and the surface area to volume ratio within the lumens. It has been hypothesized that the large surface area to volume ratio and enclosure of ovarian CICs leads to the accumulation of cytokines and growth hormones and

initiates cell signaling [8,148]. Increased levels of IL-1 and IL-6, which are secreted by cells on the surface of the ovary [149], enhance the proliferation of ovarian tumors [12], and the accumulation of other cytokines and hormones may lead to dysplasia [150]. In contrast to cell signaling that can be amplified when the ligand is concentrated [148], the impact of variations in curvature on cell behavior has not been explored. In order to isolate curvature as a system variable without impacting concentration of factors in the media, we designed a novel system to pattern curved substrates in collagen gels (**Fig. 5.1**). Using this system, negative molds with either a flat surface, convex low curvature (comparable to the high curvature examined in lumens), or convex high curvature (comparable to larger CICs) were fabricated using a 3D printer. By polymerizing collagen I between the molds and the bottom of an 8-well chamber slide, substrates with concave curves between two flat plateau regions were formed. FTE cells were seeded to confluency on these curved substrates and allowed to form cell-cell interactions. A preliminary study was carried out to investigate the effects of curvature on cell seeding. Substrates with curvatures greater than the ones used in our study were not able to be seeded uniformly due to challenges in seeding cells resulting from not being able to use the rotation method employed with lumens. Fluorescent imaging indicated that the substrates used in our study (flat, low curvature, and high curvature) were seeded uniformly (**Fig. 5.4**), ensuring that changes in cell behavior observed in curved regions were not an artifact of cells settling to the bottom of the curve during seeding.

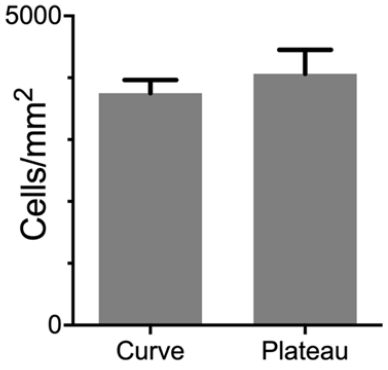

Figure 5.4: Cell density on curved substrates. Quantification of DAPI stain after seeding cells on high curvature substrates determined that there was not a significant difference in initial seeding density between the bottom of the curve and flat plateau regions on the sides of the same culture device. n = 9 devices per condition.

After FTE cells were seeded to confluency on substrates with different curvatures, the cells invaded into the collagen I substrates, similar to the invasion observed in lumens (**Fig. 5.5a**). As shown in the

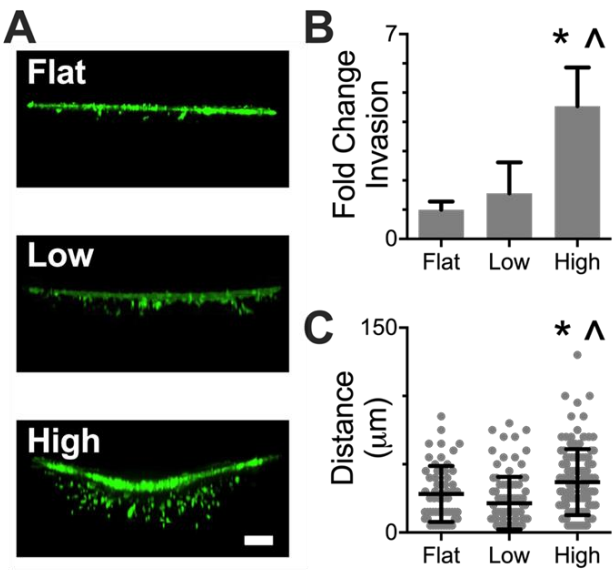

Figure 5.5: Increasing curvature increased the number and distance of FTE cell invasion. A) Z-stack cross-section reconstruction of phalloidin stained FTE cells seeded on collagen I gels with a flat surface, low curvature, or high curvature. Scale bar = 100 μm. B) Increasing curvature increased the number of cells that invade. n = 8 gels for flat and low curvature; 9 gels for high curvature. C) Increased curvature increased invasion distance of FTE cells. n = 56 cells for flat, 94 cells for low curvature, and 127 cells for high curvature. * indicates $p < 0.05$ relative to flat, ^ indicates $p < 0.05$ relative to low curvature by Tukey.

representative cross-sectional images of cells on flat, low curvature, and high curvature substrates, cell invasion did not occur on flat gels or in the plateau regions on each side of the curve. As curvature increased, invasion increased, with significantly more cells invading into high curvature substrates compared to both the flat and low curvature substrates (**Fig. 5.5b**). This finding was consistent with our observations in the lumen model. Thus, the monolayer of cells was able to respond to curvature that is at least an order of magnitude greater than the curvature of a single cell, which highlights the importance of studying the cells as a collective. In addition, the distance that invading cells moved into the collagen was significantly greater from the high curvature compared to the other conditions (**Fig. 5.5c**). We also attempted to visualize actin stress fibers within cells using a phalloidin stain to determine if curvature was causing cells to reorganize their cytoskeleton, but we were not able to clearly image actin fibers in our system. Taken together, these data indicate that smaller curvature, as would be expected in a newly formed, larger CIC would have minimal impact on FTE cell invasion. However, as the CIC resolves, it decreases in size, causing an increase in curvature that may transition FTE cells to an invasive phenotype. Our prior results demonstrated that FTE invasion from the CIC is also impacted by changes in the soluble factors present and the ECM density/composition of the surrounding stroma [142]. Combined, these results help to demonstrate why despite the broad presence of CICs in the ovary, ovarian cancer remains

relatively rare [151] as variations in the microenvironment impact the ability of FTE to progress towards a cancerous phenotype.

5.5.3 Matrix metalloproteinases (MMPs) are necessary for invasion but expression is not altered by curvature

Cell invasion into the extracellular matrix commonly requires matrix remodeling by matrix metalloproteinases (MMPs), a family of proteases that degrade ECM with MMP-ECM specificity [152]. We hypothesized that MMPs were necessary for invasion of FTE cells, and that the changes in invasion associated with substrate curvature may result from curvature-induced changes in expression of collagen I-degrading MMPs. To test this hypothesis, cultures were treated with vehicle or a combination of two broad-spectrum MMP inhibitors (batimastat and GM6001), which inhibit all MMPs that degrade collagen I. We examined the impact of this inhibition in the high curvature condition, as this culture setup contains both the highest invasion (within the curve) and the lowest invasion (from the flat regions surrounding the curve). MMP inhibition significantly reduced the number of invading cells in the curve (**Fig. 5.6a**); as in Fig. 5.5, cells did not invade on the plateau region in either condition. Inhibiting MMPs also significantly decreased the distance that cells invaded (**Fig. 5.6b**). Since MMPs impacted invasion, we next examined if gene expression for *Mmps* was different between curved and flat regions by cutting the culture device into three sections (*i.e.,* the two plateaus on the sides and the curved region in the center,

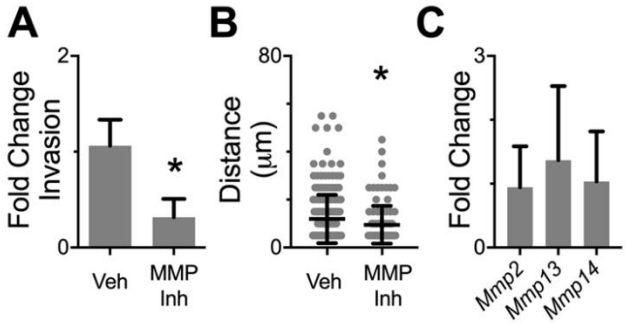

Figure 5.6: MMPs were required for invasion but were not upregulated on curved substrates. A) The number of invading cells on high curvature substrates was reduced with treatment with GM6001 and batimastat (MMP Inh). n = 17 gels for vehicle, 16 gels for MMP inhibition. B) The average invasion distance was decreased with GM6001 and batimastat. n = 222 cells for vehicle; 110 cells for MMP inhibition. C) Fold change in expression for *Mmp-2, Mmp-13,* and *Mmp-14* was less than two between cells on curved regions and plateau regions of collagen I hydrogels. Other *Mmps* that were tested were not detected over 40 PCR cycles. n = 3. * indicates $p < 0.05$ using a two-sided t-test.

Fig. 5.1e). The relative levels of collagen I degrading collagenases (*Mmp-1a*, *Mmp-8*, and *Mmp-13*) and gelatinases (*Mmp-2*, *Mmp-9*, and *Mmp-14*) were then compared between curved and plateau regions by qRT-PCR. *Mmp-1a, Mmp-8,* and *Mmp-13* were not detected after 40 PCR cycles, suggesting they were expressed at very minimal levels by FTE cells on either curved or flat substrates. Additionally, the levels of *Mmp-2, Mmp-13,* and *Mmp-14* did not significantly vary between curved and plateau regions (**Fig. 5.6c**). Taken together, these data indicate that MMPs are necessary for curvature-based invasion, but curvature does not increase invasion into a collagen I substrate through a mechanism involving increased expression of MMPs.

5.5.4 Fibronectin production is increased on plateau regions

Increased fibronectin production has been shown to facilitate the invasion of ovarian cancer cells *in vivo* [153]. We therefore investigated FTE cell fibronectin production on curved substrates to see if curvature was inducing fibronectin production. When curved collagen gels were stained for fibronectin 48 hours after seeding cells, we found that curved regions did not have increased fibronectin production. Instead, FTE cells produced increased fibronectin at plateau regions adjacent to the curve (**Fig. 5.7**).

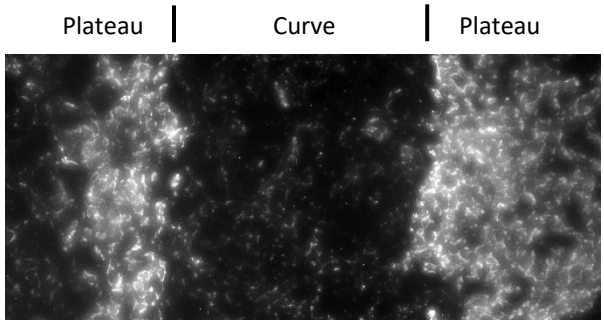

Figure 5.7: Fibronectin on curved substrates. Fibronectin staining shows increased fibronectin production by FTE cells on the plateau regions adjacent to curved regions.

5.5.5 Finite element model of cells on curved substrates

The lack of MMP upregulation on curved collagen I substrates suggested that while MMPs facilitate migration after cells begin to invade, matrix remodeling is not involved in the initiation of invasion. To identify the mechanism responsible for initiation, we began with the observation that the curvatures

affecting invasion would be sensed by a single cell as being essentially flat. Therefore, the curvature is sensed at the scale of the monolayer rather than that of a single cell. By contrast, invasion occurs by individual cells, indicating that some mechanism must transmit a multi-cellular cue, curvature, to the scale of an individual cell. A potential mechanism is mechanical force, which would be altered globally by curvature and sensed locally by a single cell. We therefore hypothesized that curvature altered the normal stress applied by cells to the substrate in the direction of invasion.

To test this hypothesis, we developed an FE model consisting of a layer of cells adhered to a substrate having dimensions matching the collagen substrates used in the experiments (**Fig. 5.8a and 5.8b**). An important component of the model is the forces transmitted between neighboring cells and between cells and the substrate. As in previous studies [144,145], springs were used to make the cell-cell and cell-substrate connections; the stiffness of the springs was modified to control the magnitudes of cell-cell and cell-substrate adhesions by selecting either rigid springs, which transmitted force with minimal deformation, or compliant springs, which deformed significantly, thus transmitting less force.

We used the model to quantify the effect of substrate curvature on the stress at the cell-substrate interface. For this initial analysis, the spring stiffnesses were set to be rigid. Our analysis focused on the center of curved region, defined as within 200 μm of the center of the curve. As in a previous study [144], the normal stress fluctuated from negative (compressive) at the center of each cell to positive (tensile) at the edge of each cell. The average stress was significantly affected by curvature, with increasing curvature increasing the average stress (**Fig. 5.8c**). This is consistent with the experiments that showed greater FTE cell invasion occurring on substrates with greater curvature (**Fig. 5.5b**).

The model was then used to assess the impact of altering different mechanical components within the cell layer. First, contractility was reduced by decreasing the contractile strain by a factor of 10. This

produced a proportional decrease in the stress at the cell-substrate interface (**Fig. 5.8d**). Therefore, if cell-substrate stress is required for cell invasion as hypothesized, the model predicts that reducing cell contractility would reduce invasion. Next, the impact of cell-substrate adhesions was assessed by using compliant springs at the cell-substrate interface. Interestingly, reducing the cell-substrate connections decreased the fluctuations in the stress but had little impact on the average normal stress applied by each cell (**Fig. 5.8e**). According to our hypothesis that cell-substrate stress causes invasion, this finding suggests that changes in cell-substrate adhesion would have no impact on invasion. Lastly, the impact of cell-cell adhesions was quantified by using compliant springs at each cell-cell interface. Reducing the spring stiffness increased the fluctuations in the stress within each cell but reduced the average stress between the cell layer and substrate (**Fig. 5.8f**). In sum, the model findings provide a means to test our hypothesis that cell-substrate stresses cause invasion—reducing cell contractility or cell-cell adhesions would reduce cell-substrate stresses which in turn is hypothesized to reduce cell invasion, while reducing cell-substrate adhesion would have no impact.

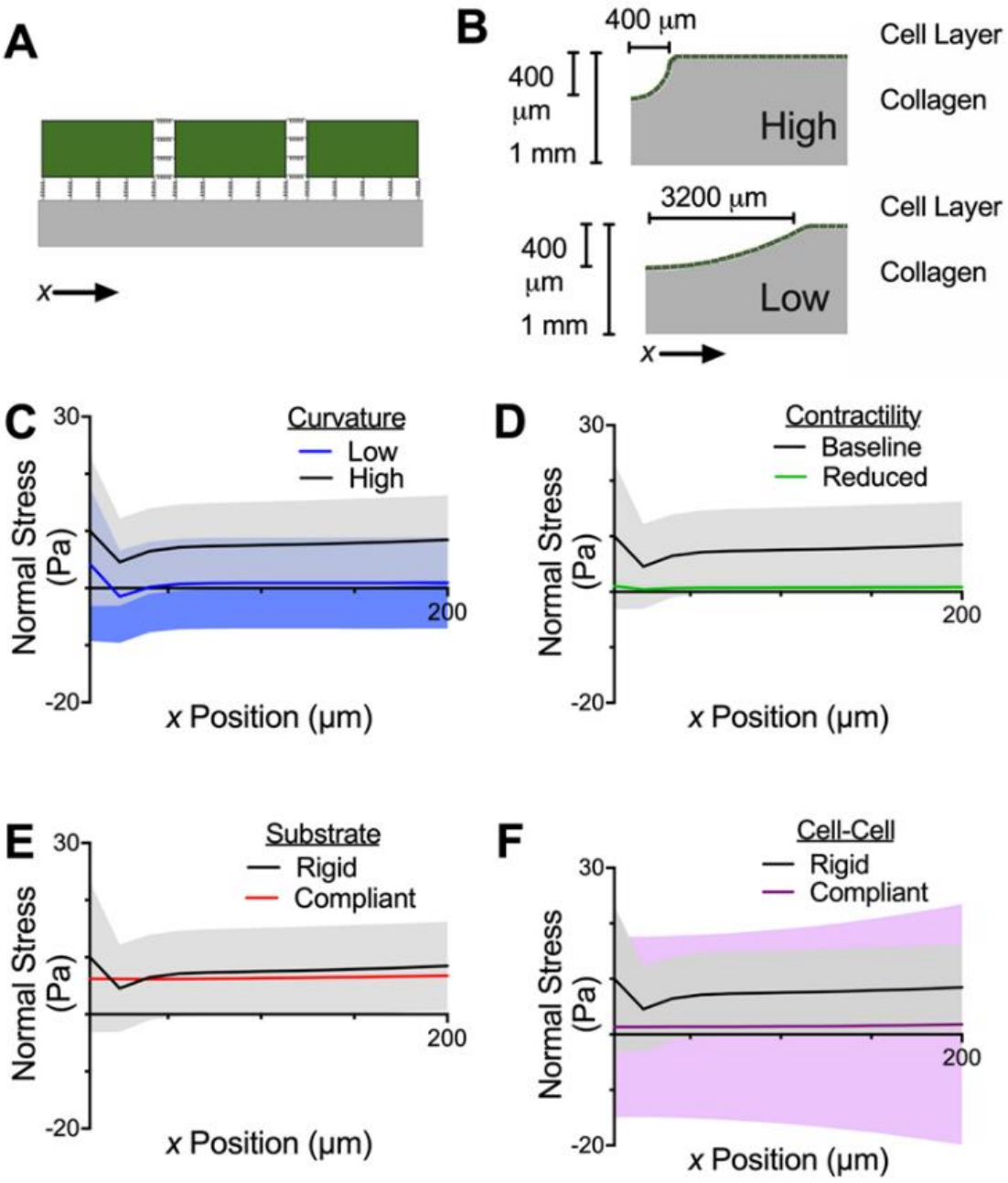

Figure 5.8: FE model of cells on curved substrates. A) Schematic showing the basic structure of the FE model. Cells (green) are connected to each other and the substrate (gray) via springs. B) Schematic showing dimensions of the FE model on substrates with low and high curvature. C) Increasing curvature increases the normal stress between cells and the substrate within 200 μm of the center of the curve. Solid lines show the mean of the normal stress applied by each cell; shaded areas show the standard deviation. D) Reducing contractility within the cell monolayer by a factor of 10 decreases the average normal stress per cell and the variation between springs within each cell. E) Adjusting springs connecting cells to the substrate from rigid to compliant has little effect on the average normal stress applied by each cell. F) Adjusting springs connecting cells to each other from rigid to compliant reduces the average normal stress applied by each cell.

5.5.6 Experiments confirm a role for contractility and cell-cell adhesion in invasion

We attempted to confirm the FE model's prediction that higher curvature lead to increased normal stress using traction force experiments on polyacrylamide gels; however, high curvature caused FTE cells to lift off of the polyacrylamide gels and form a bridge across the curved region. This lifting is likely due to the relative density of integrins on polyacrylamide gels compared to collagen gels and prevented the quantification of traction forces. To test predictions of the FE model that invasion depends on contractility and cell-cell adhesions but not cell-substrate adhesions, cells were seeded on collagen I substrates with high curvature and treated with drugs targeting contractility, cell-substrate adhesion, and cell-cell adhesion. Blebbistatin, a selective inhibitor of myosin II [154], was used to reduce overall cell contractility. When cells on curved collagen I hydrogels were treated with blebbistatin, there was a significant decrease in both the number of invading cells (**Fig. 5.9a**) and the average distance each cell invaded (**Fig. 5.9b**). This is consistent with the predictions of the model showing reduced contractility reduces the stress at the

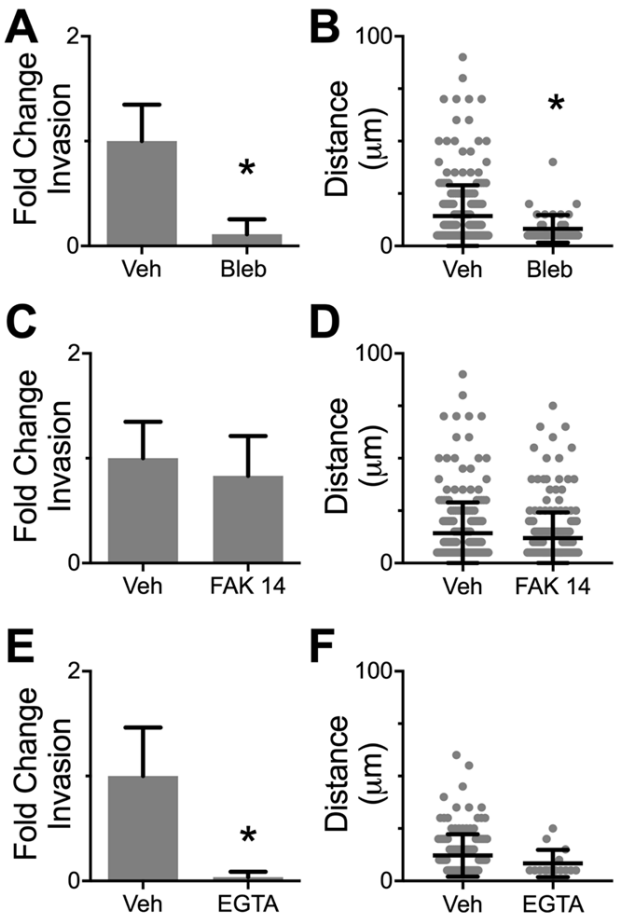

Figure 5.9: The impact of drug inhibitors on FTE cell invasion on substrates with high curvature. A) Blebbistatin decreased the number of invading cells. n = 18 gels for vehicle and 6 gels for blebbistatin. B) Blebbistatin decreased the average distance of invasion. n = 253 cells for vehicle and 44 cells for blebbistatin. C) FAK inhibitor 14 did not impact the number of invading cells. n = 18 gels for vehicle and 8 gels for FAK inhibitor 14. D) FAK inhibitor 14 did not impact invasion distance. n = 253 cells for vehicle and 235 cells for FAK inhibitor 14. E) EGTA decreased the number of invading cells on curved substrates. n = 19 gels for vehicle and 14 gels for EGTA. F) EGTA did not impact invasion distance. n = 149 cells for vehicle and 15 cells for EGTA. * indicates $p < 0.01$ using a two-sided t-test.

cell-substrate interface (**Fig. 5.8d**) and with the fact that myosin II activity is essential for cell migration and invasion [155].

We next assessed the impact of cell-substrate and cell-cell adhesions on invasion. Cell-substrate adhesions were reduced with FAK Inhibitor 14, which blocks focal adhesion kinase phosphorylation [156]. This intervention had no impact on either the number of invading cells (**Fig. 5.9c**) or cell invasion distance (**Fig. 5.9d**). Finally, cell-cell adhesions were inhibited by using EGTA to chelate calcium ions, which are necessary for cadherin function [157]. EGTA significantly reduced the number of cells that invaded on curved substrates (**Fig. 5.9e**). These findings can be explained by our hypothesis that stresses at the cell-substrate interface affect initiation of invasion: the FE model shows that cell-cell adhesion, but not cell-substrate adhesion, affects the normal stress applied by cells to the substrate. Similarly, the experimental data confirms that reducing cell-cell adhesion, but not cell-substrate adhesion, reduces invasion. Interestingly, the average cell invasion distance was unaltered by EGTA (**Fig. 5.9f**), which may suggest that cell-cell forces transmitted through cadherins impact the initiation of invasion but have minimal effect on invasion once a cell has initiated this process.

EGTA chelation of Ca^{2+} ions may have effects outside of cadherins through other calcium-dependent signaling pathways. Therefore, to confirm a role for cell-cell adhesion, we sought to identify the specific cadherin involved through an alternative approach. As N- and E-cadherin are the two main adhesion proteins in adherens junctions, confluent monolayers of FTE cells were immunostained for each protein. Fluorescent imaging demonstrated that confluent FTE cells expressed N-cadherin but not E-cadherin at their cell-cell junctions (**Fig. 5.10a and 5.10b**) indicating that N-cadherin is likely a major cell-cell adhesion protein in FTE monolayers. We therefore specifically blocked N-cadherin using a blocking antibody added to the cells prior to initiation of culture and formation of cell-cell junctions. With this treatment, FTE cells

displayed a significant reduction in the number of invading cells compared to isotype control (**Fig. 5.10c**). In accordance with EGTA data (**Fig. 5.9f**) blocking N-cadherin did not change the distance FTE cells were able to invade (**Fig 5.10d**). It therefore appears that N-cadherin is responsible for the cell-cell adhesion required for invasion. Together with the results of the FE model, these findings demonstrate that initiation of invasion results from a global force balance in the cell layer, which is transmitted through cell-cell adhesions and to the interface between each cell and the substrate. This global force balance can be altered by changing substrate curvature, contractility, or cell-cell adhesions with any of these three preventing initiation of invasion.

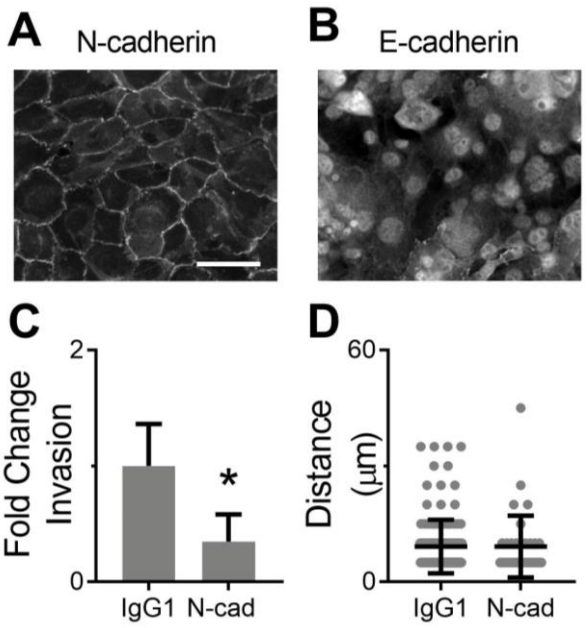

Figure 5.10: Blocking N-cadherin interactions decreased FTE cell invasion from substrates with high curvature. A, B) Immunofluorescent staining for N-cadherin and E-cadherin in FTE cells showed the presence of N-cadherin but not E-cadherin at cell-cell junctions. Scale bar = 25 μm. C) Treatment with an N-cadherin blocking antibody decreased the number of invading cells. n = 8 gels per condition. * indicates $p < 0.001$ by two-sided t-test. D) Treatment with an N-cadherin blocking antibody did not impact invasion distance. n = 135 cells for IgG1 and 35 cells for N-cadherin blocked condition.

5.5.7 Cell-cell adhesion and MMP mechanisms of curvature-based invasion act on different timescales

Given that we observed both MMP-dependent and cell-cell adhesion-dependent impacts on invasion, we hypothesized that these two mechanisms influenced different aspects of FTE cell invasion from curved substrates. Specifically, we hypothesized that cell-cell tension was involved in the initial step of an FTE cell breaking away from the cell monolayer and invading into collagen I, while MMPs allowed those FTE cells that had escaped the monolayer to invade further into the matrix. To test this hypothesis, inhibitors of cell-cell adhesion (EGTA) or MMPs (blebbistatin and GM6001) were added to cells on substrates with high

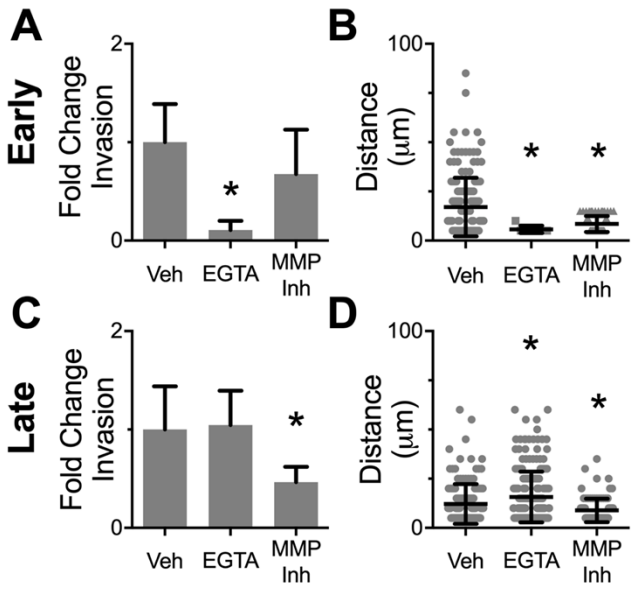

Figure 5.11: EGTA and MMP inhibitors impacted invasion from substrates with high curvature on different timescales. A,B) To examine the impact of early inhibition, cells were treated one hour after seeding and invasion was measured at 24 hours. A) EGTA decreased the number of invading cells, while MMP inhibitors had no significant effect. n = 8 gels per condition. B) Both EGTA and MMP inhibitors decreased the average invasion distance. n = 170 cells for vehicle, 7 cells for EGTA, and 65 cells for MMP inhibitors. C,D) To examine the impact of inhibition once invasion had begun, cells on curved substrates were treated 24 hours after seeding and invasion was measured at 72 hours. C) EGTA had no effect on the number of invading cells, while MMP inhibitors decreased the number of invading cells. n = 17 gels for vehicle, 10 gels for EGTA, and 6 gels for MMP inhibitors. D) EGTA treatment increased average invasion distance, while MMP inhibitors decreased average invasion distance. n = 149 cells for vehicle, 217 cells for EGTA, and 94 cells for MMP inhibitors. * indicates p <0.05 relative to vehicle control using Dunnett's test.

curvature for either early (one hour after seeding, invasion after 24 hours with inhibitors) or later (24 hours after seeding and measuring invasion at 72 hours) stages of invasion. We selected 24 hours as prior observations had suggested that cell invasion was clearly initiated by this time. EGTA was used to inhibit cadherins rather than the N-cadherin blocking antibody as EGTA could be added in the middle of an experiment while blocking antibodies needed to be incubated with FTE cells before seeding to effectively disrupt cell-cell adhesions. EGTA treatment during initial invasion significantly decreased the number of invading cells while MMP inhibitors did not (**Fig. 5.11a**). When the distance of invasion was quantified at 24 hours, both EGTA and MMP inhibitors significantly reduced FTE cell invasion distance (**Fig. 5.11b**). When inhibitors were added to cells on curved substrates after 24 hours, EGTA did not impact the number of invading FTE cells while MMP inhibitors significantly decreased invasion number, suggesting that by 24 hours most cells had already initiated invasion yet still required MMPs to invade into the substrate (**Fig. 5.11c**). Adding EGTA after 24 hours significantly increased invasion distance, while MMP inhibitors significantly decreased FTE cell invasion distance (**Fig. 5.11d**). Taken together, these data indicate that initial invasion (during the first 24 hours)

depended on the global force balance transmitted by the cell-cell junctions, but this mechanism was no longer applicable for cells that already had broken away from the monolayer and begun to invade independently. In contrast, MMPs promoted invasion throughout the duration of the experiments and governed the distance that FTE cells were able to invade into the matrix.

5.6 Conclusion

Curvature is a major component of epithelial tissues throughout the body, yet the impact of substrate curvature on the behavior of confluent monolayers of epithelial cells has not been rigorously investigated. In ovarian cancer, the microenvironmental niche of ovarian CICs has been hypothesized to induce the cancerous progression of cells trapped within these cysts, and our previous work showed that this niche environment can promote FTE cell invasion [142]. Our results demonstrated that cell invasion was influenced by curvature, with more cells invading on substrates with higher curvature and essentially no invasion on flat substrates. Invasion from curved substrates was dependent on MMPs, but did not involve changes in MMP expression. Rather, an FE model predicted that overall cell contractility and cell-cell adhesion were important for curvature-based invasion, while cell-substrate connections did not impact invasion. Our results confirmed this experimentally, identifying N-cadherin as the responsible junctional protein and supporting that cell-cell adhesion was required for contractile forces in the cell layer to be transmitted to the local cell-substrate interface, thus initiating invasion. After cells began to invade, MMPs regulated the distance of invasion. CICs shrink in size during resolution, and this structural change will result in areas with increased curvature within these cysts; our results suggest that cells can sense this change—even though orders of magnitude larger than the cell body—and transition to an invasive phenotype as a result. The work described here provides a foundation for future studies investigating the impact of curvature on epithelial cells and may have implications for metastasis in epithelial tumors that arise in these structures.

Chapter 6: Conclusions and future directions

6.1 Introduction

This thesis illustrated mechanisms of how follicular fluid, the microenvironment of ovarian CICs, and substrate curvature potentially contribute to the progression of normal FTE cells to HGSOC. In Chapter 3, we discovered that follicular fluid caused divalent cation-dependent clustering of FTE cells that enabled these cells to evade anoikis. When we investigated the role of integrins and cadherins on FTE cell anoikis, no significant effects were discovered, and the exact mechanism of follicular fluid-based anoikis resistance remains elusive. In Chapter 4, we quantified the collagen composition, concentration, and organization surrounding ovarian CICs and utilized a microfluidic lumen model to replicate these properties *in vitro*. Using this system, we found that FTE cells underwent spontaneous invasion out of microfluidic lumens into the surrounding collagen. The extent of invasion increased with follicular fluid stimulation, decreased collagen concentration, and substituting collagen III for collagen I. In Chapter 5, investigated the impact of substrate curvature on FTE cell invasion, and found that the number of invading cells increased with decreased radius of curvature. A FE model predicted that cell contractility and cell-cell adhesions induced curvature-based invasion by generating forces normal to the substrate. *In vitro* experiments confirmed the FE model's predictions as contractility and N-cadherin were necessary for the initiation of curvature-based invasion. Furthermore, we show that invasion of FTE cell on collagen substrates is a two-step process with substrate curvature initiating invasion though a cell-cell tension- based mechanism and MMP degradation of collagen facilitating FTE cell extension into the ECM. Collectively, these results demonstrated that follicular fluid and the microenvironment of ovarian CICs could impact anoikis and invasion of FTE cells, and provided further evidence implicating follicular fluid and CICs in the progression of HGSOC. To gain a better understanding of follicular fluid, the CIC microenvironment, and substrate curvature in ovarian cancer progression, I propose that future studies should include separation of

follicular fluid using size exclusion chromatography (SEC), alignment of collagen fibers in our CIC model, and formation of convex curvatures for studying cell extrusion.

6.2 Size exclusion chromatography of follicular fluid

In Chapter 3, we discovered that follicular fluid enabled FTE cells to evade anoikis. Using centrifugal filtration, we determined that the molecule in follicular fluid that allowed cells to evade anoikis was larger than 100 kDa. However, this method did not allow for further separation of follicular fluid, and the exact mechanism of follicular fluid-based anoikis resistance could not be determined. Pinpointing the exact mechanism that allowed FTE cells to evade anoikis would be useful for a number of reasons: 1) Patient ascites fluid, which surrounds the ovary and mixes with follicular fluid after ovulation, could be screened for the factor responsible for anoikis resistance, and the correlation between this molecule and the extent of HGSOC metastasis and patient outcome could be evaluated. 2) If this follicular fluid component is found to correlate with increased HGSOC metastasis or worse patient prognosis, this molecule could potentially be used as a diagnostic marker in HGSOC treatment. 3) It is possible that inhibiting this follicular fluid component would reduce the spread of HGSOC, and the impact of inhibition could be tested in a mouse model of HGSOC [3].

In order to separate follicular fluid into smaller and more precise fractions, we could utilize SEC, a method by which molecules in solution are separated based on size. Using this technique, biomolecules could be separated under non-denaturing conditions, preserving the bioactivity of follicular fluid. Furthermore, PBS, which did not impact FTE cell anoikis in our studies, has previously been used as the solvent in the mobile phase of SEC [158]. After performing SEC, gel electrophoresis should be used to confirm the separation of proteins and obtain the molecular weight range for each fraction. The anoikis assay we developed could then be run with each follicular fluid fraction to narrow the molecule responsible for

follicular fluid-based anoikis down to a testable range. Once a fraction that elicits the same anoikis resistance in FTE cells as follicular fluid has been discovered, the molecular weight range of this fraction will be used to identify follicular fluid components from previous studies [66]. The concentration of each protein potentially responsible for anoikis resistance would be measured in human follicular fluid, and the impact of individual factors on FTE cell anoikis resistance would be tested at concentrations identified in follicular fluid samples. If a single factor is responsible for follicular fluid based anoikis resistance, exogenously adding just this molecule in an anoikis assay should result in a decrease in propidium iodide positive cells comparable to follicular fluid; however, it is possible that multiple factors from follicular fluid contribute to the anoikis resistance. In this case, different follicular fluid fractions should decrease the percent of PI positive cells in an anoikis assay, but the decrease in cell death should be smaller than unfractionated follicular fluid. The proteins in all fractions that impacted anoikis would be identified and tested following the previously described method. Once individual factors that enable FTE cells to evade anoikis have been identified, these molecules would be added together to an anoikis assay to confirm that the combination elicits an anoikis response comparable to unfractionated follicular fluid. If SEC is unable to sufficiently separate follicular fluid, other chromatography techniques such as ion chromatography could be used to further separate samples.

6.3 Collagen alignment, other ECM proteins, and FTE cell invasion

In Chapter 4, IHC and SHG analysis showed that ovarian CICs were surrounded by a dense band of collagen I and III that was aligned parallel to the CIC boundary. While collagen I and III are important structural proteins in the ECM, there are many other ECM proteins that help dictate cell phenotype. One recent study measured ECM gene expression in HGSOC tumors and developed a PLS model to predict patient outcome based on the expression of these genes. This model predicted that increased levels of *COL11A1*, *FN1*, and *VSCN* and decreased levels of *LAMC1*, *HPSG2*, and *TNXB* lead to worse patient prognosis [159].

The ECM proteins that correspond to these genes should be evaluated for their impact on HGSOC progression, since their upregulation or downregulation in HGSOC tumors leads to a more aggressive phenotype. These ECM components could be easily incorporated into the microfluidic lumen platform that we used in this thesis, and their impact on FTE cell invasion could be evaluated. In addition to ECM composition, ECM alignment and organization have been found to play a major role in cancer invasion but were not evaluated in this thesis. In breast cancer, TACS, which characterize the alignment of collagen fibers surrounding tumors, have been found to influence cell invasion and predict patient prognosis, with collagen fibers aligned perpendicular to the tumor boundary facilitating invasion and foreshadowing a worse patient outcome [62]. We hypothesize that these properties translate to the collagen organization surrounding CICs and FTE cell invasiveness. Collagen fibers have previously been aligned by embedding streptavidin coated beads in collagen and applying a magnetic field during gelation [160]. This technique could be applied to our CIC model to align collagen fibers within microfluidic devices. Experiments could then be conducted to quantify the impact of parallel and perpendicular collagen fibers on FTE cell invasion. Furthermore, it has been shown that tumor cells can realign collagen fibers to facilitate invasion [61], and this experimental setup could be used to evaluate the potential of FTE cells to rearrange collagen fibers surrounding CICs. If FTE cells are found to efficiently reorganize collagen fibers to facilitate invasion, drug inhibition studies could be performed to discover the exact mechanism of fiber rearrangement. Any drug that effectively blocks fiber reorganization and FTE cell invasion could be evaluated for its impact on overall disease progression in a mouse model of HGSOC, as therapeutic strategies that target the tumor microenvironment are an emerging area of cancer research [161].

6.4 Factors initiating FTE cell detachment from the fallopian tube

Curved topographies exist in epithelial coated tissues throughout the body, and in this thesis, we identify a N-cadherin based mechanism by which concave substrates increase FTE cell invasion. While our work

indicates that concave curvature is likely important for inducing FTE cell invasion during HGSOC progression, the impact of convex curvature on cell behavior requires further investigation. In the instance of HGSOC, the fallopian tube fimbria contains fingerlike projections with regions of convex curvature (**Fig. 2.1**) and multilayered FTE lesions and cell extrusion are more prevalent in these areas than the rest of the fallopian tube [39,95]. I hypothesize that convex curvature will cause FTE cells to detach and be exfoliated from a confluent monolayer, aiding to their metastasis throughout the peritoneal cavity. Unfortunately, cells seeded on convex curvatures would likely cause the structures to collapse since the compressive modulus of collagen is much weaker than the tensile modulus [162]. However, the technique we developed to pattern collagen gels in this thesis could be used to pattern polyacrylamide gels with convex curvature. These gels could then be coated with collagen to allow FTE cells to be seeded to confluency on substrates of varied curvature. The extent of cell extrusion could be quantified by counting the number of cells floating in media after 24 hours in culture, while cell budding and the formation of multilayered epithelium could be evaluated using confocal microscopy. If convex substrate curvature is found to impact cell detachment, the mechanism underlying this behavior could be investigated using a FE model similar to the one developed in this thesis. Any biophysical stimuli that are predicted to impact cell detachment in a FE model could be confirmed *in vitro*.

In addition to substrate curvature, the ECM composition can have a major impact on cell attachment as different types of cells preferentially adhere to various ECM molecules [57]. As described above, many ECM proteins were found to be either upregulated or downregulated in aggressive HGSOC tumors [159]. By coating polyacrylamide gels with these ECM proteins, the impact of these ECM molecules on FTE cell budding and detachment could be evaluated. In addition to biophysical mechanisms of FTE cell detachment, the impact of follicular fluid on cell detachment should be investigated due to the proximity of the ovary and fallopian tube and the correlation between ovulation and HGOSC risk [4,5,70]. The

potential additive effects of follicular fluid and substrate curvature on FTE cell extrusion could be investigated by adding follicular fluid to FTE cells on varied substrate curvatures. If follicular fluid is found to alter the detachment of FTE cells, it could be separate into testable fractions using SEC as previously described. Since detachment of FTE cells from the fallopian tube is necessary for metastasis in HGSOC, the influence of the cell microenvironment on this behavior is important to evaluate. Further studies investigating the impact of substrate curvature, composition, and chemical stimuli on cell behavior could help discover new biophysical and biochemical mechanisms between cells and their environment.

Appendix

A.1: CRISPR knockout of *Brca1* did not have sufficient efficiency for future studies

One of the most common molecular events in HGOSC is the inactivation of *BRCA1*, a tumor suppressor gene that is responsible for repairing damaged DNA or initiating apoptosis if DNA damage is too extensive to be repaired [49,163]. Furthermore, women that harbor a germline mutation in *BRCA1* are at an increased risk for HGSOC. Based on these factors, we hypothesized that knocking out *Brca1* in mouse FTE cells will increase the cancerous progression of these cells. In order to test this hypothesis, we decided to use cluster regularly interspaced short palindromic repeats (CRISPR) and CRISPR-associated protein 9 (Cas9) to modify the *Brca1* locus in both WT and cells that have been immortalized with TERT and overexpress a loss of function, dominant negative $p53^{R175H}$ protein. The CRISPR-Cas9 system that we used will generate double-strand DNA breaks at specific locations in the *Brca1* gene. Cells will attempt to repair these breaks using non-homologous end joining (NHEJ), a type of DNA repair that does not use a repair template; however, NHEJ is prone to generating indel errors typically consisting of 1-10 base pairs [164]. These indels typically generate a frameshift mutation resulting in a nonfunctional protein.

A.2: Methods

A.2.1: LentiCRISPR V2 Ligation

Individual lentiviral CRISPR plasmids targeting the mouse *Brca1* locus were designed using previously established techniques [165,166]. Briefly, 5 µg of lentiCRISPR V2 plasmid (Addgene; Watertown, MA) was digested with *BsmBI* for 30 minutes at 37°C and gel purified using QIAQuick Gel Extraction Kit (Qiagen; Hilden, Germany). Oligos designed to target *Brca1* (IDT; Coralville, IA) (**Table A.1**) were annealed to each other and ligated into the digested lentiviral CRISPR plasmid.

Table A.1: Oligos targeting *Brca1.* Oligos designed to target *Brca1*, the exons that these oligos target, and their on-target and off-target scores.

Exon #	Oligo 1 (5'-3')	Oligo 2 (5'-3')	On-Target Score	Off-Target Score
2	CACCGTTGTACTTCTTGAATTTGGA	AAACTCCAAATTCAAGAAGTACAAC	69.1	34.1
4	CACCGGTTATCTCATTCTTACACAA	AAACTTGTGTAAGAATGAGATAACG	46.8	37.6
5	CACCGGCTGCTTTTGAGCTTGACAC	AAACGTGTCAAGCTCAAAAGCAGCC	69.8	39.7
6	CACCGGCGTCGATCATCCAGAGCGT	AAACACGCTCTGGATGATCGACGCC	58.1	48.2
6	CACCGGCTACCGGAACCGTGTCAGA	AAACTCTGACACGGTTCCGGTAGCC	45.3	46.9
6	CACCGGCATTTCCAGGTTCGACCTG	AAACCAGGTCGAACCTGGAAATGCC	35.2	46.3
7	CACCGTCACTGATCTCACGATTCCA	AAACTGGAATCGTGAGATCAGTGAC	59.4	43.2

A.2.2: Transformation of *E. coli* and purification of plasmid

One Shot™ Stbl3™ chemically competent *E. coli* were transformed with the lentiCRISPR V2 plasmids containing ligated oligos targeting *Brca1* following manufacturer's instructions. A lentiCRISPR V2 plasmid without any ligated oligos was used as a negative control. The *E. coli* solution was spread on ampicillin resistant plates and incubated overnight at 37°C. A single colony from each plasmid was then selected and grown in a 15 mL shaker tubes with 3 mL of LB with ampicillin on a shaker at 300 RPM at 37°C overnight. The next day, 100 µL of the starter colony was transferred to a flask containing 100 mL of LB and ampicillin and incubated on a shaker at 200 RPM at 37°C overnight. Plasmids were purified from *E. coli* using a QIAprep Spin Miniprep Kit (Qiagen) following manufacturer's instructions. Proper ligation was confirmed via Sanger sequencing using the primers suggested on Addgene.

A.2.3: Lentiviral Packaging

The lentiCRISPR V2 plasmids were transfected into HEK 293T cells (ATCC) in a 6-well plate using a lenti-vpak packaging kit (Origene Technologies; Rockville, MD) following manufacturer's instructions. After 12 hours of incubation, the media was changed, and the volume of media was reduced to 1 mL per well. The next day, the first batch of viral supernatant was collected and the media was replaced. On the following

day, a second batch of viral supernatant was collected. Viral supernatant was spun at 3000 rpm/min for 5 min and filtered through at 0.45 µm filter.

A.2.4: Transduction

Transduction was performed by first adding 450 µL of FTE cells at a concentration of 20,000 cell/mL to 300 µL of virus. Polybrene (Santa Cruz Biotechnology; Dallas, TX) was added to a final concentration of 8 µg/mL and the solution was mixed well. This solution was added to a 24-well plate (750 µL per well), and the entire plate was centrifuged at 1000 RPM for two hours to concentrate cells and virus to the bottom of each well. Using this technique and a GFP plasmid, transduction efficiency was 68% for WT FTE cells and 79% for $TP53^{R175H}$ FTE cells.

A.2.5: Puromycin Treatment

The sensitivity of mouse FTE cells to puromycin (DOT Scientific; Burton, MI) was determined using a kill curve. Cells were seeded in a 48-well plate for 24 hours and puromycin was spiked into the media at final concentrations between 0.5 and 100 µg/mL. The percent of dead cells was estimated visually after 48 hours and the minimum concentration of puromycin that was able to kill cells (**Fig. A.1**) was determined to be 2.5 µg/mL for $TP53^{R175H}$ cells and 50 µg/mL for WT cells. After transduction, cells were allowed to recover for 72 hours before puromycin treatment was initiated. Cells were treated with the concentrations of puromycin that killed all cells without puromycin resistance for 7 days with the media being changed every day.

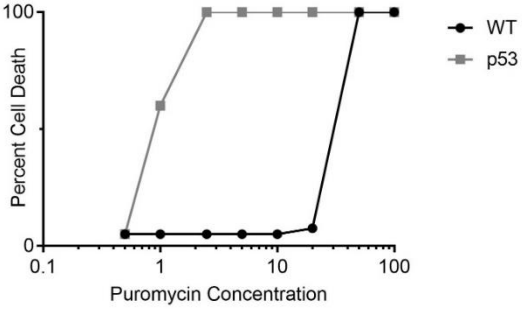

Figure A.1: Puromycin kill curves. FTE cells were treated with varying concentrations of puromycin and the percent cell death was measured after 48 hours.

A.2.6 Analysis of clonal knockouts

In order to analyze our CRISPR knockout efficacy, genomic DNA was isolated from cells. Briefly, cells were trypsinized, spun down, and resuspended in 100 µL of 50 mM NaOH. The cell solution was placed at 95°C for 20 minutes to lyse all cells and then neutralized with 50 µL TE buffer. The concentration of DNA from samples was determined using a NanoDrop. PCR was performed on genomic DNA using the primers listed in Table 2 and using Accuprime Taq Polymerase High Fidelity following the manufacturer's instructions. The genomic DNA sequences were determined using Sanger sequencing. The CRISPR efficiency was then measured by comparing the resulting sequences to a non-mutated genome using a previously described method called tracking of indels by decomposition (TIDE) [167].

Table A.2: Primers. The primer sets used to sequence genomic DNA, and the exon region containing indels targeted by each set of primers.

Exon #	Forward Primer (5'-3')	Reverse Primer (5'-3')
2	CTTCAGCGTGAGAACTCCTCCA	GATGGCAGAGTGAAGACCACCT
4	ACACACACACACGCATGTTTGT	CACCCCTAGTCCCCAAACACAT
5	TTTCAGGAGCCTACAGGGAAGC	GGCAGGCAGGAAGTACATCAGA
6	CTGTGTAGGTCTGGCTGTCCTC	ATAGTCACATGCACAACCCCCA
6	CTGTGTAGGTCTGGCTGTCCTC	ATAGTCACATGCACAACCCCCA
6	CTGTGTAGGTCTGGCTGTCCTC	ATAGTCACATGCACAACCCCCA
7	CTCTGTGCCTCCTTTGTAGCCT	ATGGTGATGGTGGTAGTGGTGG

A.3: Results

When CRISPR-Cas9 knockout of *Brca1* was performed on FTE cell, cells were selected with puromycin, and mutation efficiency was measured using TIDE, we found that the highest mutation percentage we obtained was 7.5% in WT FTE cells and 40.9% in $Tp53^{R273H}$ FTE cells (**Fig A.2**). The highest efficiency occurred with virus targeting Exon 4 of the *Brca1* locus (**Table A.1**) for both cell types.

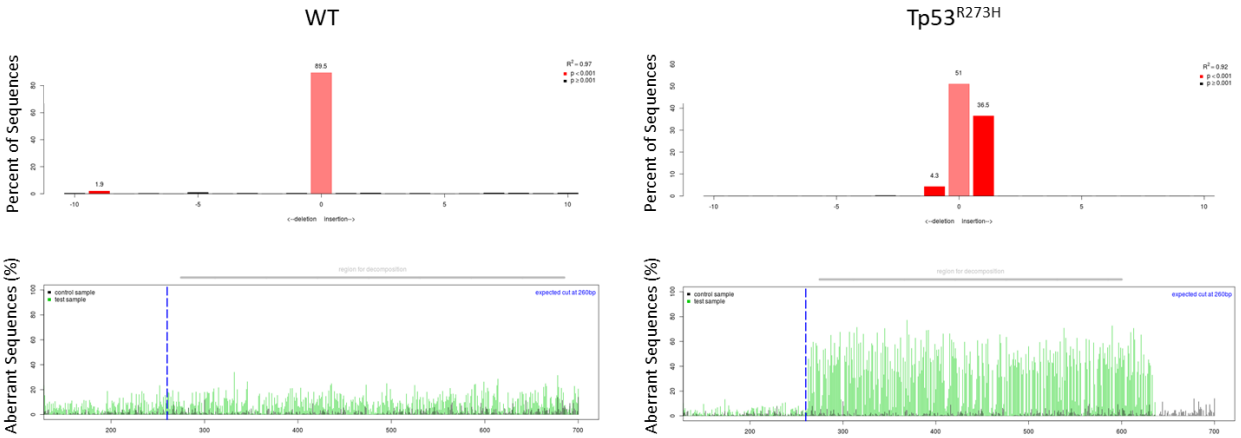

Figure A.2: TIDE analysis of CRISPR mutations. The percent of sequences mutated and the percent of aberrant sequences are shown for WT and Tp53^{R274H} FTE cells. This data shows that the mutation efficiency was 7.5% and 40.9% for WT cells and Tp53^{R274H} cells respectively.

To determine the impact of these mutations on production of a functional Brca1 protein, a Western blot was performed using an antibody that targets the C-terminus of *Brca1* (MAB22101, R&D Systems) at 1:500, detected with Anti-Rabbit IgG, HRP-linked Antibody (7074S, Cell Signaling) at 1:1000 and Clarity Western ECL (Biorad), and imaged on an Odyssey Infrared Imaging System (Li-Cor). clarity (**Fig. A.3**). Protein analysis showed that there is Brca1 protein with an entact C-terminus being produced by mutated FTE cells. In an attempt to further select cells that has received the lentiCRISPR V2 plasmid, an additional round of puromycin treatment lasting seven days was performed. After this selection, genomic DNA was again collected from cells and the mutation efficiency in these cells was analyzed using TIDE. Interestingly, it was found that the mutation efficiency dropped to 1.2% and 26.1% for WT FTE cells and TP53^{R273H} FTE cells respectively (**Fig. A4)**.

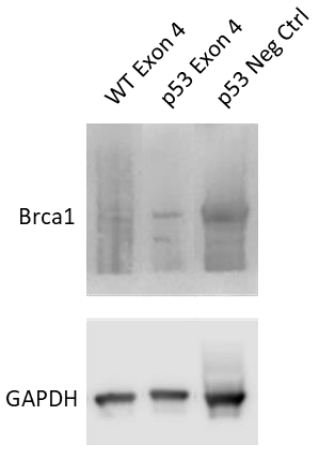

Figure A.3: Western blot of Brca1. Western blot shows that Brca1 protein is still expressed in WT and Tp53^{R274H} FTE cells.

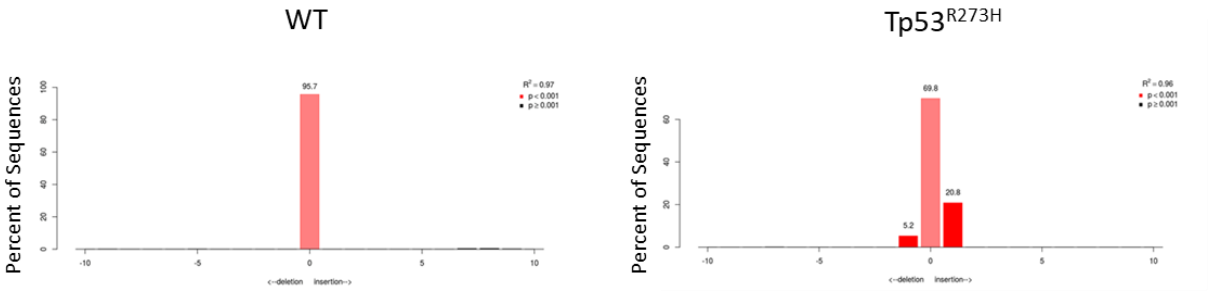

Figure A.4: TIDE analysis of CRISPR mutations after additional puromycin selection. The percent of sequences mutated and the percent of aberrant sequences are shown for WT and Tp53^{R274H} FTE cells. This data shows that

A.4: Conclusions

While we were able to use a CRISPR-Cas9 system to mutate *Brca1* in FTE cells, we were unable to establish a clonal knockout line from the pool of edited cells. When further puromycin selection was performed, the mutation efficiency unexpectedly decreased. The most reasonable explanation for this decrease in the percent of mutated cells is that *Brca1* has an important role in DNA repair and checkpoint regulation. Without a functional Brca1 protein, it is likely that FTE cells will be more susceptible to abnormal amounts of DNA damage. Therefore, it is possible that the stress of puromycin treatment could increase the number of genetic mutations that FTE without *Brca1* harbor. Since *Brca1* is not the only checkpoint inhibitor that forces cells into apoptosis when DNA damage becomes too extensive, it is possible that increased DNA damage from puromycin treatment will cause FTE cells with *Brca1* mutations to undergo apoptosis.

Unfortunately, the inability to generate *Brca1* knockout cell lines with a high purity of mutated cells prevented the further study of the *Brca1* mutation on WT and TP53^{R273H} FTE cell phenotypes. Since this is still a viable question for the cancerous progression of FTE cells, alternative approaches could be used to investigate the impact of *Brca1* mutations. One approach would be to still use the CRISPR-Cas9 system,

but generate the cell line from a single cell knockout. The major pitfall of this approach is the extensive number of passages needed to generate enough cells for experiments from a single cell. Another approach would be to use siRNA to knock down *Brca1* in FTE cells. However, this approach is also imperfect as high siRNA knockdown efficiency is difficult to obtain and the effects are transient and not suitable for studies lasting multiple days.

B.1: Phenotypic analysis of WT FTE cells and FTE cells expressing a mutation p53 protein

The expression of a dominant negative, non-functional p53 protein may have an impact on the phenotypical behavior of mouse FTE cells. To investigate the impact of a mutated p53 protein on FTE cells, we performed comet assays to assess DNA damage and cell counts to measure cell proliferation.

B.2: Methods

B.2.1: Comet Assay

FTE cells were treated with a 1% H_2O_2 for 20 minutes followed by media for 30 minutes, 1 hour, or 2 hours. Cells were then spun down at 0.1*g* for 5 minutes, embedded in 1% agarose, and sandwiched between a glass slide and a coverslip. Agarose was cooled in the fridge for 5 minutes. Cells embedded in agarose were then lysed using Triton X100 and electrophoresis was performed on slides for 25 minutes at 1 V/cm. Slides were then stained with propidium iodide and imaged using fluorescent microscopy. The OpenComet plugin for FIJI [168] was then used to analyze images for the percent of DNA in the head of cells, the length of the tail, and tail moment.

B.2.2: Proliferation Assay

FTE cells were seeded in 10 cm plates. The next day, one plate of WT FTE cells and one plate of FTE cells with p53 mutated protein were counted using a hemocytometer, and the rest of the plates were either treated with 6% follicular fluid or SFM. The number of cells in each plate were then counted at 24, 48, 72, and 96 hours using a hemocytometer and normalized to the original cell counts.

B.3: Results

B.3.1: Expression of a mutated dominant negative, non-functional p53 protein reduces the ability of FTE cells to repair DNA damage

The ability of FTE cells to repair damaged DNA was measured with a comet assay (**Fig. B.1a**). This experiment showed that there was initially no difference in DNA repair between WT FTE cells and FTE cells expressing a mutated p53 protein; however, after one hour, WT FTE cells had significantly more DNA in the head of comets (**Fig. B.1b**), shorter tail length (**Fig. B.1c**), and reduced tail moment (**Fig. B.1d**) than FTE cells expressing a mutated p53 protein. Taken together, these data indicate the expression of a dominant negative, non-functional p53 protein in FTE cells reduced their ability to repair DNA damage over time.

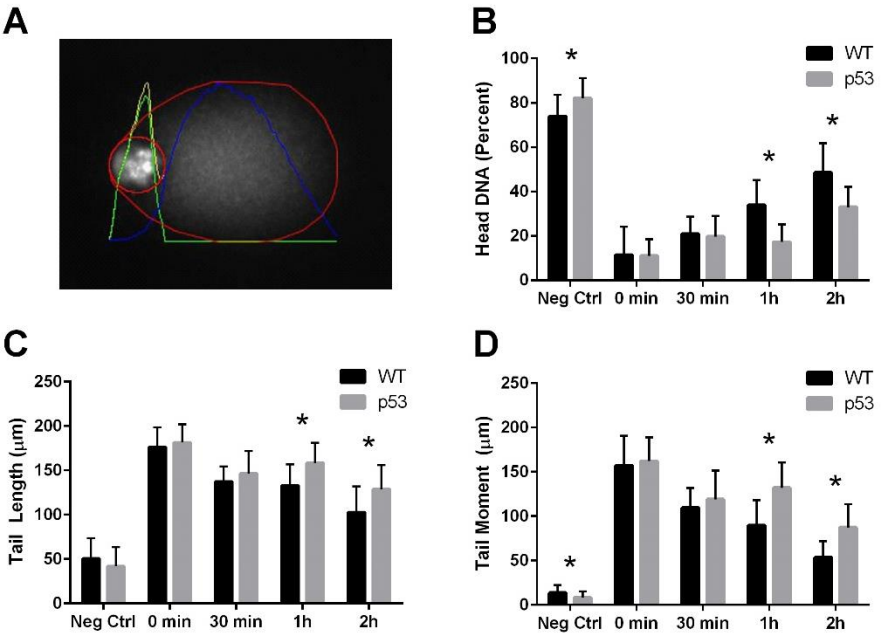

Figure B.1: DNA damage repair in FTE cells. A) Example of comet assay analysis. B) The percent of DNA in the head of comets of FTE cells. n = 24-47, * indicates $p < 0.05$ using students t-test. C) The length of comet tails of FTE cells. n = 24-47, * indicates $p < 0.05$ using students t-test. D) The tail moment of FTE cells. n = 24-47, * indicates $p < 0.05$ using students t-test.

B.3.2: Proliferation of FTE cells with follicular fluid

We initially attempted to measure proliferation in mouse FTE cells using Click-iT EdU; however, we found that these cells were not able to update EdU and a different approach to measure proliferation was needed. Proliferation was measured by counting the number of FTE cells at 24, 48, 72, and 96 hours and comparing those data points to time 0. Our data indicates that proliferation appeared to plateau around

72 hours in all conditions. WT FTE cells had increased proliferation compared to FTE cells expressing a mutated p53 protein. However, follicular fluid did not increase proliferation (**Fig. B.2**).

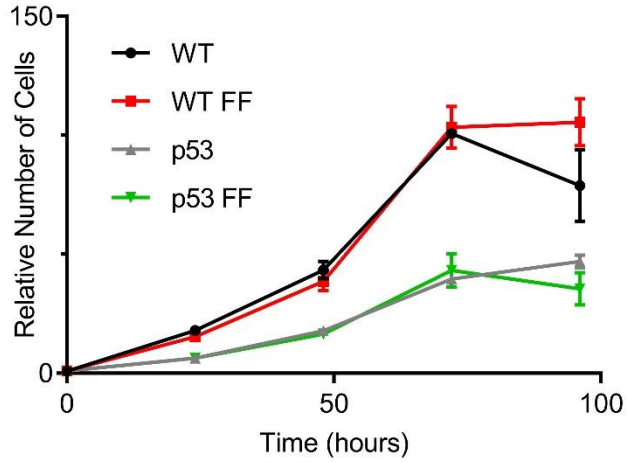

Figure B.2: Proliferation of FTE cells. WT FTE cells proliferated more quickly than FTE cells expressing a mutated p53 protein. Follicular fluid did not impact proliferation in either cell type.

B.4: Conclusions

When the ability of FTE cells to repair DNA damage and proliferation were measured, our results showed that the expression of a mutated p53 protein significantly reduced the ability of cells to repair damage and reduced proliferation rate. When follicular fluid was added to our proliferation assay, it had no impact on proliferation. Taken together, these data indicate that the expression of non-functional p53 protein can impact FTE cell phenotypes indicative of cancer.

References

1. Jemal A, Siegel R, Ward E, Hao Y, Xu J, Thun MJ. Cancer statistics, 2009. *CA Cancer J Clin* 2009; **59:** 225-49.
2. Rauh-Hain JA, Krivak TC, Del Carmen MG, Olawaiye AB. Ovarian cancer screening and early detection in the general population. *Rev Obstet Gynecol* 2011; **4:** 15-21.
3. Perets R, Wyant GA, Muto KW, et al. Transformation of the fallopian tube secretory epithelium leads to high-grade serous ovarian cancer in Brca;Tp53;Pten models. *Cancer Cell* 2013; **24:** 751-65.
4. Purdie DM, Bain CJ, Siskind V, Webb PM, Green AC. Ovulation and risk of epithelial ovarian cancer. *Int J Cancer* 2003; **104:** 228-32.
5. Yang-Hartwich Y, Gurrea-Soteras M, Sumi N, et al. Ovulation and extra-ovarian origin of ovarian cancer. *Sci Rep* 2014; **4:** 6116.
6. Cramer DW, Welch WR. Determinants of ovarian cancer risk. II. Inferences regarding pathogenesis. *J Natl Cancer Inst* 1983; **71:** 717-21.
7. Fathalla MF. Incessant ovulation--a factor in ovarian neoplasia? *Lancet* 1971; **2:** 163.
8. Auersperg N, Wong AS, Choi KC, Kang SK, Leung PC. Ovarian surface epithelium: biology, endocrinology, and pathology. *Endocr Rev* 2001; **22:** 255-88.
9. Emori MM, Drapkin R. The hormonal composition of follicular fluid and its implications for ovarian cancer pathogenesis. *Reprod Biol Endocrinol* 2014; **12:** 60.
10. Irving-Rodgers HF, Hummitzsch K, Murdiyarso LS, et al. Dynamics of extracellular matrix in ovarian follicles and corpora lutea of mice. *Cell Tissue Res* 2010; **339:** 613-24.
11. Fadare O. *Precancerous lesions of the gynecologic tract : diagnostic and molecular genetic pathology*. Cham ; New York: Springer International Publishing,, 2015.
12. Berchuck A, Kohler MF, Boente MP, Rodriguez GC, Whitaker RS, Bast RC. Growth regulation and transformation of ovarian epithelium. *Cancer* 1993; **71:** 545-51.
13. Dean M, Jin V, Russo A, Lantvit DD, Burdette JE. Exposure of the extracellular matrix and colonization of the ovary in metastasis of fallopian-tube-derived cancer. *Carcinogenesis* 2019; **40:** 41-51.
14. Banet N, Kurman RJ. Two types of ovarian cortical inclusion cysts: proposed origin and possible role in ovarian serous carcinogenesis. *Int J Gynecol Pathol* 2015; **34:** 3-8.
15. He X, Jiang Y. Substrate curvature regulates cell migration. *Phys Biol* 2017; **14:** 035006.
16. Baptista D, Teixeira L, van Blitterswijk C, Giselbrecht S, Truckenmüller R. Overlooked? Underestimated? Effects of Substrate Curvature on Cell Behavior. *Trends Biotechnol* 2019.
17. Leung PCK, Adashi EY. The Ovary. London: Academic Press,, 2019: 1 online resource.
18. Jansen RP. Endocrine response in the fallopian tube. *Endocr Rev* 1984; **5:** 525-51.
19. Schwartz PE. The role of prophylactic oophorectomy in the avoidance of ovarian cancer. *Int J Gynaecol Obstet* 1992; **39:** 175-84.
20. Casey MJ, Synder C, Bewtra C, Narod SA, Watson P, Lynch HT. Intra-abdominal carcinomatosis after prophylactic oophorectomy in women of hereditary breast ovarian cancer syndrome kindreds associated with BRCA1 and BRCA2 mutations. *Gynecol Oncol* 2005; **97:** 457-67.
21. Bell DA. Origins and molecular pathology of ovarian cancer. *Mod Pathol* 2005; **18 Suppl 2:** S19-32.
22. Feeley KM, Wells M. Precursor lesions of ovarian epithelial malignancy. *Histopathology* 2001; **38:** 87-95.
23. Lengyel E. Ovarian cancer development and metastasis. *Am J Pathol* 2010; **177:** 1053-64.

24. Flesken-Nikitin A, Choi KC, Eng JP, Shmidt EN, Nikitin AY. Induction of carcinogenesis by concurrent inactivation of p53 and Rb1 in the mouse ovarian surface epithelium. *Cancer Res* 2003; **63:** 3459-63.
25. Orsulic S, Li Y, Soslow RA, Vitale-Cross LA, Gutkind JS, Varmus HE. Induction of ovarian cancer by defined multiple genetic changes in a mouse model system. *Cancer Cell* 2002; **1:** 53-62.
26. Liu J, Yang G, Thompson-Lanza JA, et al. A genetically defined model for human ovarian cancer. *Cancer Res* 2004; **64:** 1655-63.
27. Sasaki R, Narisawa-Saito M, Yugawa T, et al. Oncogenic transformation of human ovarian surface epithelial cells with defined cellular oncogenes. *Carcinogenesis* 2009; **30:** 423-31.
28. Wu J, Liu Z, Shao C, et al. HMGA2 overexpression-induced ovarian surface epithelial transformation is mediated through regulation of EMT genes. *Cancer Res* 2011; **71:** 349-59.
29. van Niekerk CC, Boerman OC, Ramaekers FC, Poels LG. Marker profile of different phases in the transition of normal human ovarian epithelium to ovarian carcinomas. *Am J Pathol* 1991; **138:** 455-63.
30. Kruk PA, Uitto VJ, Firth JD, Dedhar S, Auersperg N. Reciprocal interactions between human ovarian surface epithelial cells and adjacent extracellular matrix. *Exp Cell Res* 1994; **215:** 97-108.
31. Berchuck A, Rodriguez G, Olt G, et al. Regulation of growth of normal ovarian epithelial cells and ovarian cancer cell lines by transforming growth factor-beta. *Am J Obstet Gynecol* 1992; **166:** 676-84.
32. Murdoch WJ, Martinchick JF. Oxidative damage to DNA of ovarian surface epithelial cells affected by ovulation: carcinogenic implication and chemoprevention. *Exp Biol Med (Maywood)* 2004; **229:** 546-52.
33. Godwin AK, Testa JR, Hamilton TC. The biology of ovarian cancer development. *Cancer* 1993; **71:** 530-6.
34. Okamura H, Katabuchi H. Detailed morphology of human ovarian surface epithelium focusing on its metaplastic and neoplastic capability. *Ital J Anat Embryol* 2001; **106:** 263-76.
35. Selvaggi SM. Tumors of the ovary, maldeveloped gonads, fallopian tube, and broad ligament. *Arch Pathol Lab Med* 2000; **124:** 477.
36. Okamoto S, Okamoto A, Nikaido T, et al. Mesenchymal to epithelial transition in the human ovarian surface epithelium focusing on inclusion cysts. *Oncol Rep* 2009; **21:** 1209-14.
37. Tanwar PS, Mohapatra G, Chiang S, et al. Loss of LKB1 and PTEN tumor suppressor genes in the ovarian surface epithelium induces papillary serous ovarian cancer. *Carcinogenesis* 2014; **35:** 546-53.
38. Piek JM, van Diest PJ, Zweemer RP, et al. Dysplastic changes in prophylactically removed Fallopian tubes of women predisposed to developing ovarian cancer. *J Pathol* 2001; **195:** 451-6.
39. Karst AM, Drapkin R. Ovarian cancer pathogenesis: a model in evolution. *J Oncol* 2010; **2010:** 932371.
40. Karst AM, Levanon K, Drapkin R. Modeling high-grade serous ovarian carcinogenesis from the fallopian tube. *Proc Natl Acad Sci U S A* 2011; **108:** 7547-52.
41. Folkins AK, Jarboe EA, Saleemuddin A, et al. A candidate precursor to pelvic serous cancer (p53 signature) and its prevalence in ovaries and fallopian tubes from women with BRCA mutations. *Gynecol Oncol* 2008; **109:** 168-73.
42. Lee Y, Miron A, Drapkin R, et al. A candidate precursor to serous carcinoma that originates in the distal fallopian tube. *J Pathol* 2007; **211:** 26-35.
43. Donnez J, Casanas-Roux F, Caprasse J, Ferin J, Thomas K. Cyclic changes in ciliation, cell height, and mitotic activity in human tubal epithelium during reproductive life. *Fertil Steril* 1985; **43:** 554-9.

44. Chen EY, Mehra K, Mehrad M, et al. Secretory cell outgrowth, PAX2 and serous carcinogenesis in the Fallopian tube. *J Pathol* 2010; **222:** 110-6.
45. Knudson AG. Two genetic hits (more or less) to cancer. *Nat Rev Cancer* 2001; **1:** 157-62.
46. Okamoto A, Sameshima Y, Yokoyama S, et al. Frequent allelic losses and mutations of the p53 gene in human ovarian cancer. *Cancer Res* 1991; **51:** 5171-6.
47. Wahl GM, Linke SP, Paulson TG, Huang LC. Maintaining genetic stability through TP53 mediated checkpoint control. *Cancer Surv* 1997; **29:** 183-219.
48. Ahmed AA, Etemadmoghadam D, Temple J, et al. Driver mutations in TP53 are ubiquitous in high grade serous carcinoma of the ovary. *J Pathol* 2010; **221:** 49-56.
49. Pal T, Permuth-Wey J, Betts JA, et al. BRCA1 and BRCA2 mutations account for a large proportion of ovarian carcinoma cases. *Cancer* 2005; **104:** 2807-16.
50. Jarboe E, Folkins A, Nucci MR, et al. Serous carcinogenesis in the fallopian tube: a descriptive classification. *Int J Gynecol Pathol* 2008; **27:** 1-9.
51. Visvanathan K, Vang R, Shaw P, et al. Diagnosis of serous tubal intraepithelial carcinoma based on morphologic and immunohistochemical features: a reproducibility study. *Am J Surg Pathol* 2011; **35:** 1766-75.
52. Meserve EEK, Brouwer J, Crum CP. Serous tubal intraepithelial neoplasia: the concept and its application. *Mod Pathol* 2017; **30:** 710-21.
53. Iwanicki MP, Chen HY, Iavarone C, et al. Mutant p53 regulates ovarian cancer transformed phenotypes through autocrine matrix deposition. *JCI Insight* 2016; **1**.
54. Jabłońska-Trypuć A, Matejczyk M, Rosochacki S. Matrix metalloproteinases (MMPs), the main extracellular matrix (ECM) enzymes in collagen degradation, as a target for anticancer drugs. *J Enzyme Inhib Med Chem* 2016; **31:** 177-83.
55. Cho A, Howell VM, Colvin EK. The Extracellular Matrix in Epithelial Ovarian Cancer - A Piece of a Puzzle. *Front Oncol* 2015; **5:** 245.
56. Zigrino P, Löffek S, Mauch C. Tumor-stroma interactions: their role in the control of tumor cell invasion. *Biochimie* 2005; **87:** 321-8.
57. Frantz C, Stewart KM, Weaver VM. The extracellular matrix at a glance. *J Cell Sci* 2010; **123:** 4195-200.
58. Hulmes DJ. Building collagen molecules, fibrils, and suprafibrillar structures. *J Struct Biol* 2002; **137:** 2-10.
59. Franchi M, Raspanti M, Dell'Orbo C, et al. Different crimp patterns in collagen fibrils relate to the subfibrillar arrangement. *Connect Tissue Res* 2008; **49:** 85-91.
60. Chen X, Nadiarynkh O, Plotnikov S, Campagnola PJ. Second harmonic generation microscopy for quantitative analysis of collagen fibrillar structure. *Nat Protoc* 2012; **7:** 654-69.
61. Provenzano PP, Eliceiri KW, Campbell JM, Inman DR, White JG, Keely PJ. Collagen reorganization at the tumor-stromal interface facilitates local invasion. *BMC Med* 2006; **4:** 38.
62. Conklin MW, Eickhoff JC, Riching KM, et al. Aligned collagen is a prognostic signature for survival in human breast carcinoma. *Am J Pathol* 2011; **178:** 1221-32.
63. Lind AK, Weijdegård B, Dahm-Kähler P, Mölne J, Sundfeldt K, Brännström M. Collagens in the human ovary and their changes in the perifollicular stroma during ovulation. *Acta Obstet Gynecol Scand* 2006; **85:** 1476-84.
64. Hynes RO, Naba A. Overview of the matrisome--an inventory of extracellular matrix constituents and functions. *Cold Spring Harb Perspect Biol* 2012; **4:** a004903.
65. Irving-Rodgers HF, Rodgers RJ. Extracellular matrix of the developing ovarian follicle. *Semin Reprod Med* 2006; **24:** 195-203.
66. Zamah AM, Hassis ME, Albertolle ME, Williams KE. Proteomic analysis of human follicular fluid from fertile women. *Clin Proteomics* 2015; **12:** 5.

67. Alsina-Sanchis E, Figueras A, Lahiguera Á, et al. The TGFβ pathway stimulates ovarian cancer cell proliferation by increasing IGF1R levels. *Int J Cancer* 2016; **139:** 1894-903.
68. Cheng JC, Auersperg N, Leung PC. EGF-induced EMT and invasiveness in serous borderline ovarian tumor cells: a possible step in the transition to low-grade serous carcinoma cells? *PLoS One* 2012; **7:** e34071.
69. Huang HS, Chu SC, Hsu CF, et al. Mutagenic, surviving and tumorigenic effects of follicular fluid in the context of p53 loss: initiation of fimbria carcinogenesis. *Carcinogenesis* 2015; **36:** 1419-28.
70. Bahar-Shany K, Brand H, Sapoznik S, et al. Exposure of fallopian tube epithelium to follicular fluid mimics carcinogenic changes in precursor lesions of serous papillary carcinoma. *Gynecol Oncol* 2014; **132:** 322-7.
71. Cooper JP, Youle RJ. Balancing cell growth and death. *Curr Opin Cell Biol* 2012; **24:** 802-3.
72. Nelson CM, Bissell MJ. Of extracellular matrix, scaffolds, and signaling: tissue architecture regulates development, homeostasis, and cancer. *Annu Rev Cell Dev Biol* 2006; **22:** 287-309.
73. Frisch SM, Francis H. Disruption of epithelial cell-matrix interactions induces apoptosis. *J Cell Biol* 1994; **124:** 619-26.
74. Frisch SM, Ruoslahti E. Integrins and anoikis. *Curr Opin Cell Biol* 1997; **9:** 701-6.
75. Wheelock MJ, Johnson KR. Cadherins as modulators of cellular phenotype. *Annu Rev Cell Dev Biol* 2003; **19:** 207-35.
76. Sánchez-Tilló E, Liu Y, de Barrios O, et al. EMT-activating transcription factors in cancer: beyond EMT and tumor invasiveness. *Cell Mol Life Sci* 2012; **69:** 3429-56.
77. Paoli P, Giannoni E, Chiarugi P. Anoikis molecular pathways and its role in cancer progression. *Biochim Biophys Acta* 2013; **1833:** 3481-98.
78. Simpson CD, Anyiwe K, Schimmer AD. Anoikis resistance and tumor metastasis. *Cancer Lett* 2008; **272:** 177-85.
79. Nieman MT, Prudoff RS, Johnson KR, Wheelock MJ. N-cadherin promotes motility in human breast cancer cells regardless of their E-cadherin expression. *J Cell Biol* 1999; **147:** 631-44.
80. Guo W, Giancotti FG. Integrin signalling during tumour progression. *Nat Rev Mol Cell Biol* 2004; **5:** 816-26.
81. Wang LH. Molecular signaling regulating anchorage-independent growth of cancer cells. *Mt Sinai J Med* 2004; **71:** 361-7.
82. Karst AM, Jones PM, Vena N, et al. Cyclin E1 deregulation occurs early in secretory cell transformation to promote formation of fallopian tube-derived high-grade serous ovarian cancers. *Cancer Res* 2014; **74:** 1141-52.
83. Schindelin J, Arganda-Carreras I, Frise E, et al. Fiji: an open-source platform for biological-image analysis. *Nat Methods* 2012; **9:** 676-82.
84. Russo MA, Paolillo M, Sanchez-Hernandez Y, et al. A small-molecule RGD-integrin antagonist inhibits cell adhesion, cell migration and induces anoikis in glioblastoma cells. *Int J Oncol* 2013; **42:** 83-92.
85. Zhang Y, Lu H, Dazin P, Kapila Y. Squamous cell carcinoma cell aggregates escape suspension-induced, p53-mediated anoikis: fibronectin and integrin alphav mediate survival signals through focal adhesion kinase. *J Biol Chem* 2004; **279:** 48342-9.
86. Maître JL, Heisenberg CP. Three functions of cadherins in cell adhesion. *Curr Biol* 2013; **23:** R626-33.
87. Valenta T, Hausmann G, Basler K. The many faces and functions of β-catenin. *EMBO J* 2012; **31:** 2714-36.
88. Lee CM, Shvartsman H, Deavers MT, et al. beta-catenin nuclear localization is associated with grade in ovarian serous carcinoma. *Gynecol Oncol* 2003; **88:** 363-8.

89. Khramtsov AI, Khramtsova GF, Tretiakova M, Huo D, Olopade OI, Goss KH. Wnt/beta-catenin pathway activation is enriched in basal-like breast cancers and predicts poor outcome. *Am J Pathol* 2010; **176:** 2911-20.
90. Damsky WE, Curley DP, Santhanakrishnan M, et al. β-catenin signaling controls metastasis in Braf-activated Pten-deficient melanomas. *Cancer Cell* 2011; **20:** 741-54.
91. Li K, Zhou ZY, Ji PP, Luo HS. Knockdown of β-catenin by siRNA influences proliferation, apoptosis and invasion of the colon cancer cell line SW480. *Oncol Lett* 2016; **11:** 3896-900.
92. Attaran M, Pasqualotto E, Falcone T, et al. The effect of follicular fluid reactive oxygen species on the outcome of in vitro fertilization. *Int J Fertil Womens Med* 2000; **45:** 314-20.
93. Muñoz NM, Baek JY, Grady WM. TGF-beta has paradoxical and context dependent effects on proliferation and anoikis in human colorectal cancer cell lines. *Growth Factors* 2008; **26:** 254-62.
94. Kim J, Coffey DM, Creighton CJ, Yu Z, Hawkins SM, Matzuk MM. High-grade serous ovarian cancer arises from fallopian tube in a mouse model. *Proc Natl Acad Sci U S A* 2012; **109:** 3921-6.
95. Medeiros F, Muto MG, Lee Y, et al. The tubal fimbria is a preferred site for early adenocarcinoma in women with familial ovarian cancer syndrome. *Am J Surg Pathol* 2006; **30:** 230-6.
96. Aoki Y, Kawada N, Tanaka K. Early form of ovarian cancer originating in inclusion cysts. A case report. *J Reprod Med* 2000; **45:** 159-61.
97. Provenzano PP, Inman DR, Eliceiri KW, et al. Collagen density promotes mammary tumor initiation and progression. *BMC Med* 2008; **6:** 11.
98. Kraning-Rush CM, Carey SP, Lampi MC, Reinhart-King CA. Microfabricated collagen tracks facilitate single cell metastatic invasion in 3D. *Integr Biol (Camb)* 2013; **5:** 606-16.
99. Riching KM, Cox BL, Salick MR, et al. 3D collagen alignment limits protrusions to enhance breast cancer cell persistence. *Biophys J* 2014; **107:** 2546-58.
100. Oksjoki S, Rahkonen O, Haarala M, Vuorio E, Anttila L. Differences in connective tissue gene expression between normally functioning, polycystic and post-menopausal ovaries. *Mol Hum Reprod* 2004; **10:** 7-14.
101. Endsley MP, Moyle-Heyrman G, Karthikeyan S, et al. Spontaneous Transformation of Murine Oviductal Epithelial Cells: A Model System to Investigate the Onset of Fallopian-Derived Tumors. *Front Oncol* 2015; **5:** 154.
102. Quartuccio SM, Karthikeyan S, Eddie SL, et al. Mutant p53 expression in fallopian tube epithelium drives cell migration. *Int J Cancer* 2015; **137:** 1528-38.
103. Hutson HN, Marohl T, Anderson M, Eliceiri K, Campagnola P, Masters KS. Calcific Aortic Valve Disease Is Associated with Layer-Specific Alterations in Collagen Architecture. *PLoS One* 2016; **11:** e0163858.
104. Bredfeldt JS, Liu Y, Pehlke CA, et al. Computational segmentation of collagen fibers from second-harmonic generation images of breast cancer. *J Biomed Opt* 2014; **19:** 16007.
105. Liu Y, Keikhosravi A, Mehta GS, Drifka CR, Eliceiri KW. Methods for Quantifying Fibrillar Collagen Alignment. *Methods Mol Biol* 2017; **1627:** 429-51.
106. Jiménez-Torres JA, Peery SL, Sung KE, Beebe DJ. LumeNEXT: A Practical Method to Pattern Luminal Structures in ECM Gels. *Adv Healthc Mater* 2016; **5:** 198-204.
107. Krahn KN, Bouten CV, van Tuijl S, van Zandvoort MA, Merkx M. Fluorescently labeled collagen binding proteins allow specific visualization of collagen in tissues and live cell culture. *Anal Biochem* 2006; **350:** 177-85.
108. Kirk JM, Da Costa PE, Turner-Warwick M, Littleton RJ, Laurent GJ. Biochemical evidence for an increased and progressive deposition of collagen in lungs of patients with pulmonary fibrosis. *Clin Sci (Lond)* 1986; **70:** 39-45.
109. Lämmermann T, Sixt M. Mechanical modes of 'amoeboid' cell migration. *Curr Opin Cell Biol* 2009; **21:** 636-44.

110. Shen X, Liu X, Zhu P, et al. Proteomic analysis of human follicular fluid associated with successful in vitro fertilization. *Reprod Biol Endocrinol* 2017; **15:** 58.
111. Kurman RJ, Shih IM. The origin and pathogenesis of epithelial ovarian cancer: a proposed unifying theory. *Am J Surg Pathol* 2010; **34:** 433-43.
112. Dean M, Jin V, Russo A, Burdette JE. PTEN and colonization of the ovary in metastasis of fallopian tube-derived ovarian cancer *American Association for Cancer Research - Addressing Critical Questions in Cancer Research and Treatment.* Pittsburgh, PA, 2017.
113. Berkholtz CB, Lai BE, Woodruff TK, Shea LD. Distribution of extracellular matrix proteins type I collagen, type IV collagen, fibronectin, and laminin in mouse folliculogenesis. *Histochem Cell Biol* 2006; **126:** 583-92.
114. Curry TE, Smith MF. Impact of extracellular matrix remodeling on ovulation and the folliculo-luteal transition. *Semin Reprod Med* 2006; **24:** 228-41.
115. Tan OL, Hurst PR, Fleming JS. Location of inclusion cysts in mouse ovaries in relation to age, pregnancy, and total ovulation number: implications for ovarian cancer? *J Pathol* 2005; **205:** 483-90.
116. Wen BL, Brewer MA, Nadiarnykh O, et al. Texture analysis applied to second harmonic generation image data for ovarian cancer classification. *J Biomed Opt* 2014; **19:** 096007.
117. Berger AJ, Linsmeier KM, Kreeger PK, Masters KS. Decoupling the effects of stiffness and fiber density on cellular behaviors via an interpenetrating network of gelatin-methacrylate and collagen. *Biomaterials* 2017; **141:** 125-35.
118. Ray A, Slama ZM, Morford RK, Madden SA, Provenzano PP. Enhanced Directional Migration of Cancer Stem Cells in 3D Aligned Collagen Matrices. *Biophys J* 2017; **112:** 1023-36.
119. Cavalcanti-Adam EA, Volberg T, Micoulet A, Kessler H, Geiger B, Spatz JP. Cell spreading and focal adhesion dynamics are regulated by spacing of integrin ligands. *Biophys J* 2007; **92:** 2964-74.
120. Balaban NQ, Schwarz US, Riveline D, et al. Force and focal adhesion assembly: a close relationship studied using elastic micropatterned substrates. *Nat Cell Biol* 2001; **3:** 466-72.
121. Baker BM, Trappmann B, Wang WY, et al. Cell-mediated fibre recruitment drives extracellular matrix mechanosensing in engineered fibrillar microenvironments. *Nat Mater* 2015; **14:** 1262-8.
122. Wozniak MA, Modzelewska K, Kwong L, Keely PJ. Focal adhesion regulation of cell behavior. *Biochim Biophys Acta* 2004; **1692:** 103-19.
123. Sabeh F, Shimizu-Hirota R, Weiss SJ. Protease-dependent versus -independent cancer cell invasion programs: three-dimensional amoeboid movement revisited. *J Cell Biol* 2009; **185:** 11-9.
124. Tilbury K, Lien CH, Chen SJ, Campagnola PJ. Differentiation of Col I and Col III isoforms in stromal models of ovarian cancer by analysis of second harmonic generation polarization and emission directionality. *Biophys J* 2014; **106:** 354-65.
125. Kanzawa S, Endo H, Shioya N. Improved in vitro angiogenesis model by collagen density reduction and the use of type III collagen. *Ann Plast Surg* 1993; **30:** 244-51.
126. Carey SP, Martin KE, Reinhart-King CA. Three-dimensional collagen matrix induces a mechanosensitive invasive epithelial phenotype. *Sci Rep* 2017; **7:** 42088.
127. Rusby JE, Brachtel EF, Michaelson JS, Koerner FC, Smith BL. Breast duct anatomy in the human nipple: three-dimensional patterns and clinical implications. *Breast Cancer Res Treat* 2007; **106:** 171-9.
128. KLEITSCH WP. Anatomy of the pancreas; a study with special reference to the duct system. *AMA Arch Surg* 1955; **71:** 795-802.
129. Nicholson JK. The microanatomy of the distal tubules, collecting tubules and collecting ducts of the starling kidney. *J Anat* 1982; **134:** 11-23.
130. Koff SA. Guidelines to determine the size and shape of intestinal segments used for reconstruction. *J Urol* 1988; **140:** 1150-1.

131. Discher DE, Janmey P, Wang YL. Tissue cells feel and respond to the stiffness of their substrate. *Science* 2005; **310:** 1139-43.
132. Brown XQ, Ookawa K, Wong JY. Evaluation of polydimethylsiloxane scaffolds with physiologically-relevant elastic moduli: interplay of substrate mechanics and surface chemistry effects on vascular smooth muscle cell response. *Biomaterials* 2005; **26:** 3123-9.
133. Guo WH, Frey MT, Burnham NA, Wang YL. Substrate rigidity regulates the formation and maintenance of tissues. *Biophys J* 2006; **90:** 2213-20.
134. Farrelly N, Lee YJ, Oliver J, Dive C, Streuli CH. Extracellular matrix regulates apoptosis in mammary epithelium through a control on insulin signaling. *J Cell Biol* 1999; **144:** 1337-48.
135. Levina EM, Domnina LV, Rovensky YA, Vasiliev JM. Cylindrical substratum induces different patterns of actin microfilament bundles in nontransformed and in ras-transformed epitheliocytes. *Exp Cell Res* 1996; **229:** 159-65.
136. Svitkina TM, Rovensky YA, Bershadsky AD, Vasiliev JM. Transverse pattern of microfilament bundles induced in epitheliocytes by cylindrical substrata. *J Cell Sci* 1995; **108 (Pt 2):** 735-45.
137. Pinheiro D, Bellaïche Y. Mechanical Force-Driven Adherens Junction Remodeling and Epithelial Dynamics. *Dev Cell* 2018; **47:** 391.
138. Kolega J. The cellular basis of epithelial morphogenesis. *Dev Biol (N Y 1985)* 1986; **2:** 103-43.
139. Yip AK, Huang P, Chiam KH. Cell-Cell Adhesion and Cortical Actin Bending Govern Cell Elongation on Negatively Curved Substrates. *Biophys J* 2018; **114:** 1707-17.
140. Broaders KE, Cerchiari AE, Gartner ZJ. Coupling between apical tension and basal adhesion allow epithelia to collectively sense and respond to substrate topography over long distances. *Integr Biol (Camb)* 2015; **7:** 1611-21.
141. Sharma A, Gentry-Maharaj A, Burnell M, et al. Assessing the malignant potential of ovarian inclusion cysts in postmenopausal women within the UK Collaborative Trial of Ovarian Cancer Screening (UKCTOCS): a prospective cohort study. *BJOG* 2012; **119:** 207-19.
142. Fleszar AJ, Walker A, Porubsky V, et al. The Extracellular Matrix of Ovarian Cortical Inclusion Cysts Modulates Invasion of Fallopian Tube Epithelial Cells. *APL Bioeng* 2018; **2**.
143. Jimenez-Torres JA, Peery SL, Sung KE, Beebe DJ. LumeNEXT: A Practical Method to Pattern Luminal Structures in ECM Gels. *Adv Healthc Mater* 2016; **5:** 198-204.
144. Notbohm J, Kim JH, Asthagiri AR, Ravichandran G. Three-dimensional analysis of the effect of epidermal growth factor on cell-cell adhesion in epithelial cell clusters. *Biophys J* 2012; **102:** 1323-30.
145. Mertz AF, Che Y, Banerjee S, et al. Cadherin-based intercellular adhesions organize epithelial cell-matrix traction forces. *Proc Natl Acad Sci U S A* 2013; **110:** 842-7.
146. Scully RE, Young RH, Clement PB. *Tumors of the Ovary, Maldeveloped Gonads, Fallopian Tube, and Broad Ligament: Atlas of Tumor Pathology*: Amer Registry of Pathology, 1999.
147. Murdoch WJ. Ovarian surface epithelium during ovulatory and anovulatory ovine estrous cycles. *Anat Rec* 1994; **240:** 322-6.
148. Paguirigan AL, Beebe DJ. From the cellular perspective: exploring differences in the cellular baseline in macroscale and microfluidic cultures. *Integr Biol (Camb)* 2009; **1:** 182-95.
149. Ziltener HJ, Maines-Bandiera S, Schrader JW, Auersperg N. Secretion of bioactive interleukin-1, interleukin-6, and colony-stimulating factors by human ovarian surface epithelium. *Biol Reprod* 1993; **49:** 635-41.
150. Chene G, Penault-Llorca F, Le Bouëdec G, et al. Ovarian epithelial dysplasia after ovulation induction: time and dose effects. *Hum Reprod* 2009; **24:** 132-8.
151. *Cancer Facts and Figures 2016*: American Cancer Society, 2016.
152. Lu P, Takai K, Weaver VM, Werb Z. Extracellular matrix degradation and remodeling in development and disease. *Cold Spring Harb Perspect Biol* 2011; **3**.

153. Yoshimura A, Sawada K, Nakamura K, et al. Exosomal miR-99a-5p is elevated in sera of ovarian cancer patients and promotes cancer cell invasion by increasing fibronectin and vitronectin expression in neighboring peritoneal mesothelial cells. *BMC Cancer* 2018; **18:** 1065.
154. Kovács M, Tóth J, Hetényi C, Málnási-Csizmadia A, Sellers JR. Mechanism of blebbistatin inhibition of myosin II. *J Biol Chem* 2004; **279:** 35557-63.
155. Vicente-Manzanares M, Ma X, Adelstein RS, Horwitz AR. Non-muscle myosin II takes centre stage in cell adhesion and migration. *Nat Rev Mol Cell Biol* 2009; **10:** 778-90.
156. Golubovskaya VM, Nyberg C, Zheng M, et al. A small molecule inhibitor, 1,2,4,5-benzenetetraamine tetrahydrochloride, targeting the y397 site of focal adhesion kinase decreases tumor growth. *J Med Chem* 2008; **51:** 7405-16.
157. Kim SA, Tai CY, Mok LP, Mosser EA, Schuman EM. Calcium-dependent dynamics of cadherin interactions at cell-cell junctions. *Proc Natl Acad Sci U S A* 2011; **108:** 9857-62.
158. Baranyai T, Herczeg K, Onódi Z, et al. Isolation of Exosomes from Blood Plasma: Qualitative and Quantitative Comparison of Ultracentrifugation and Size Exclusion Chromatography Methods. *PLoS One* 2015; **10:** e0145686.
159. Pearce OMT, Delaine-Smith RM, Maniati E, et al. Deconstruction of a Metastatic Tumor Microenvironment Reveals a Common Matrix Response in Human Cancers. *Cancer Discov* 2018; **8:** 304-19.
160. Guo C, Kaufman LJ. Flow and magnetic field induced collagen alignment. *Biomaterials* 2007; **28:** 1105-14.
161. Roma-Rodrigues C, Mendes R, Baptista PV, Fernandes AR. Targeting Tumor Microenvironment for Cancer Therapy. *Int J Mol Sci* 2019; **20**.
162. Achilli M, Mantovani D. Tailoring Mechanical Properties of Collagen-Based Scaffolds for Vascular Tissue Engineering: The Effects of pH, Temperature and Ionic Strength on Gelation. *Polymers* 2010; **2:** 664-80.
163. Liu Y, West SC. Distinct functions of BRCA1 and BRCA2 in double-strand break repair. *Breast Cancer Res* 2002; **4:** 9-13.
164. Burma S, Chen BP, Chen DJ. Role of non-homologous end joining (NHEJ) in maintaining genomic integrity. *DNA Repair (Amst)* 2006; **5:** 1042-8.
165. Sanjana NE, Shalem O, Zhang F. Improved vectors and genome-wide libraries for CRISPR screening. *Nat Methods* 2014; **11:** 783-4.
166. Shalem O, Sanjana NE, Hartenian E, et al. Genome-scale CRISPR-Cas9 knockout screening in human cells. *Science* 2014; **343:** 84-7.
167. Brinkman EK, Chen T, Amendola M, van Steensel B. Easy quantitative assessment of genome editing by sequence trace decomposition. *Nucleic Acids Res* 2014; **42:** e168.
168. Gyori BM, Venkatachalam G, Thiagarajan PS, Hsu D, Clement MV. OpenComet: an automated tool for comet assay image analysis. *Redox Biol* 2014; **2:** 457-65.